AD-A254 264

# REPORT DOCUMENTATION PAGE

Form Approved
OMB No. 0704-0188



| 1. AGENCY USE ONLY (Leave blank) | 2. REPORT DATE | 3. REPORT TYPE AND DATES COVERED |
|---|---|---|
| | August 1992 | THESIS |

**4. TITLE AND SUBTITLE**
System Design and Relaxation Oscillations of a Titanium-Sapphire Laser

**5. FUNDING NUMBERS**

**6. AUTHOR(S)**
William L. Erikson, Captain

**7. PERFORMING ORGANIZATION NAME(S) AND ADDRESS(ES)**
AFIT Student Attending: University of Arkansas

**8. PERFORMING ORGANIZATION REPORT NUMBER**
AFIT/CI/CIA-92-072

**9. SPONSORING / MONITORING AGENCY NAME(S) AND ADDRESS(ES)**
AFIT/CI
Wright-Patterson AFB OH 45433-6583

**10. SPONSORING / MONITORING AGENCY REPORT NUMBER**

**11. SUPPLEMENTARY NOTES**

**12a. DISTRIBUTION / AVAILABILITY STATEMENT**
Approved for Public Release IAW 190-1
Distributed Unlimited
ERNEST A. HAYGOOD, Captain, USAF
Executive Officer

**12b. DISTRIBUTION CODE**

**13. ABSTRACT** *(Maximum 200 words)*



92-23498

92 8 24 007

| 14. SUBJECT TERMS | 15. NUMBER OF PAGES 102 |
|---|---|
| | 16. PRICE CODE |

| 17. SECURITY CLASSIFICATION OF REPORT | 18. SECURITY CLASSIFICATION OF THIS PAGE | 19. SECURITY CLASSIFICATION OF ABSTRACT | 20. LIMITATION OF ABSTRACT |
|---|---|---|---|
| | | | |

# SYSTEM DESIGN AND RELAXATION OSCILLATIONS OF A TITANIUM-SAPPHIRE LASER

Abstract of thesis submitted in partial fulfillment
of the requirements for the degree of
Master of Science

by

WILLIAM L. ERIKSON, B.S.
United States Air Force Academy, 1982

August, 1992
University of Arkansas

This abstract is approved by:

Thesis Director:

Surendra Pal Singh

Dr. Surendra P. Singh

## Abstract

A general method for designing a laser system is presented. Using the Ti:sapphire laser as an example, the requirements of stability, astigmatic compensation, and matching of the pump and cavity modes are addressed. Investigations into the relaxation oscillations of a Ti:sapphire laser are reported. Using four level laser rate equation theory, a technique is developed for analyzing relaxation oscillations exhibited by a laser. This technique presents a new and simple method for measuring the upper state lifetime and intrinsic cavity losses of a laser system. Beam-like vector solutions to Maxwell's equations are also presented. These solutions present a more detailed description of the polarization properties of laser beams. Experimental evidence of these properties is shown using an Argon laser.

# SYSTEM DESIGN AND RELAXATION OSCILLATIONS OF A TITANIUM-SAPPHIRE LASER

# SYSTEM DESIGN AND RELAXATION OSCILLATIONS OF A TITANIUM-SAPPHIRE LASER

A thesis submitted in partial fulfillment
of the requirements for the degree of
Master of Science

by

WILLIAM L. ERIKSON, B.S.
United States Air Force Academy, 1982

August, 1992
University of Arkansas

This thesis is approved
for recommendation to the
Graduate Council.

Thesis Director:

Surendra Pal Singh

Dr. Surendra P. Singh

Thesis Committee:

Rajendra Gupta

Dr. Rajendra Gupta

Gregory J. Salamo

Dr. Gregory J. Salamo

Bill Durham

Dr. Bill Durham, Chemistry

THESIS DUPLICATION RELEASE

I hereby authorize the University of Arkansas Libraries to duplicate this thesis when needed for research and/or scholarship.

Agreed _____

Refused _____

## Acknowledgements

I thank my wife Melissa for her loving support and faithful encouragement during my graduate school experience. I also owe many thanks to my parents, who have confidently supported me in every challenge I have undertaken.

I am indebted to Dr. Singh for his leadership in my research project. His example of pursuing a deeper understanding of the world of lasers has inspired me to do the same. I would also like to thank my colleague Yujaing Qu for his friendship and eager assistance in data collecting and solving the endless little problems that develop in experimental work.

This thesis was typeset by the author using LaTeX.

# Contents

# Chapter 1

# Introduction

The Ti:sapphire laser has been the subject of continuing research since it was first introduced by Moulton [1] as a broadly tunable solid state laser. Because of its broad tunability ($\approx$ 650–1200 nm), high output power, and demonstrated stability, the Ti:sapphire laser is gaining prominence in many areas of research. These areas include high resolution spectroscopy and high energy laser applications.

Many areas of high resolution spectroscopy research require frequency stabilized, single-mode, continuous wave (cw) lasers. Although dye lasers have been dominant in this field, the Ti:sapphire laser offers the advantages of wide tunability, ease of use, and increased stability. The dominant absorption band for Ti:sapphire is centered around 500 nm, allowing direct pumping with an argon ion laser for cw operation and doubled Nd:YAG lasers, dye lasers, and flash lamps for pulsed operation. Active frequency stabilization involves a reference cavity (Fabry Perot), some type of feedback to the laser cavity, and an intracavity compensating element. By actively stabilizing a Ti:sapphire laser, a frequency stability of 1 kHz rms relative to the reference cavity has been observed [2]. Stabilized Ti:sapphire lasers have been used for examining the hyperfine structure of the D lines and the absorption spectroscopy of the 5S$\rightarrow$5D transition in rubidium [3]. A similar Ti:sapphire laser was used to investigate the two-photon excitation of the 2S$\rightarrow$4S transition in atomic hydrogen [4]. Other areas of spectroscopic research require broadly tunable short laser pulses of relatively high energy. This is another area where the capabilities of the Ti:sapphire laser are being exploited. Various methods for active and passive mode locking of a Ti:sapphire laser have been employed to generate high power pulses in the femtosecond regime [5, 6, 7].

High energy laser applications, such as future remote space sensing systems, have generated the need for studying the energy output capabilities of Ti:sapphire lasers [8].

Output powers of 0.5 terawatt for 125-fs pulses have been observed using the technique of chirped-pulse amplification [9]. For cw operation, 350 watts of output power has been proposed using a liquid nitrogen-cooled Ti:sapphire laser [10].

Other areas of research where Ti:sapphire lasers may be useful are nonlinear optics, laser cooling, and trapping of atoms. Because of the many possible and diverse applications for a Ti:sapphire laser, there is a need for a general method for designing simple and flexible Ti:sapphire laser cavities from which a specific laser system can be constructed.

Although most of the current research involving the Ti:sapphire laser is centered around areas of specific application, little attention has been paid to the study of the dynamical behavior of this laser system. One particular dynamical behavior of interest is the relaxation oscillations exhibited by the Ti:sapphire laser. These oscillations characterize the behavior of certain laser systems when they are perturbed from steady state. Relaxation oscillations have been observed and studied in a number of other laser systems including ruby [11], dye [12] and copper-vapor [13]. By studying these relaxation oscillations, one can gain a greater insight into the parameters that drive the dynamics of the laser. Recent studies in the ultra-high speed relaxation oscillations (up to 39 GHz) of vertical cavity surface emitting diode lasers indicate potential application in the area of optical interconnect [14].

In this thesis, we present a general method for designing a Ti:sapphire laser that can be customized for specific research applications. We also report on investigations of the relaxation oscillations of a Ti:sapphire laser that we constructed. To our knowledge, these are the first such investigations to have been carried out on a Ti:sapphire laser system. By analyzing the relaxation oscillations, we measured the upper state lifetime and the intrinsic cavity losses of our laser. Our method for analyzing these oscillations presents a simple and new technique for measuring these important laser parameters.

In Chapter 2, we review the propagation characteristics of laser beams including their transformation characteristics through optical elements. With this foundation, we describe a technique using ray transformation matrices in Chapter 3 to address the problems of stability, astigmatism, and mode matching in the design of a laser system.

We also describe the design of a specific Ti:sapphire laser. In Chapter 4 we discuss the theory of relaxation oscillations based on two simplified laser rate equations. We then develop a method for analyzing the relaxation oscillations exhibited by certain lasers which allows us to measure the upper state lifetime and the intrinsic cavity losses of a laser system. Chapter 5 describes two sets of experiments conducted with our Ti:sapphire laser. The first set involved the study of the relaxation oscillations generated by cavity loss modulation. The second set of experiments was conducted to determine the intrinsic cavity losses of our laser by an independent method. Finally, in Chapter 6 we describe vector beam-like solutions of Maxwell's equations. We use these solutions to discuss the polarization properties of Gaussian laser beams. We also present experimental evidence representing these solutions.

# Chapter 2

# Propagation of Laser Beams

Any study of lasers must involve a basic understanding of the propagation characteristics of laser beams. To this end, we begin this chapter with a review of the wave nature of light and its propagation characteristics in free space (vacuum). We then derive the paraxial wave equation, which describes propagation of electromagnetic waves (beams) whose energy is concentrated near the axis of propagation, and look at a particular beam-like solution to this equation. Finally, we will see how laser beam parameters are transformed as they pass through various optical elements.

## 2.1 Propagation of Electromagnetic Waves

The behavior of an electromagnetic field is governed by Maxwell's equations, which for free space can be written in the form

$$\nabla \cdot \mathbf{E}(\mathbf{r},t) = 0\,, \tag{2.1}$$

$$\nabla \times \mathbf{E}(\mathbf{r},t) = -\frac{\partial \mathbf{B}(\mathbf{r},t)}{\partial t}\,, \tag{2.2}$$

$$\nabla \cdot \mathbf{B}(\mathbf{r},t) = 0\,, \tag{2.3}$$

$$\nabla \times \mathbf{B}(\mathbf{r},t) = \frac{1}{c^2}\frac{\partial \mathbf{E}(\mathbf{r},t)}{\partial t}\,, \tag{2.4}$$

where $c$ is the speed of light in free space, $\mathbf{E}(\mathbf{r},t)$ is the electric field and $\mathbf{B}(\mathbf{r},t)$ is the magnetic field. If we eliminate $\mathbf{B}(\mathbf{r},t)$ from these equations by taking the curl of Eq. (2.2) and the time derivative of Eq. (2.4), we obtain a closed equation for the electric field. Using the fact that time and space derivatives commute and the vector identity

$$\nabla \times (\nabla \times \mathbf{E}) = \nabla(\nabla \cdot \mathbf{E}) - \nabla^2 \mathbf{E}\,, \tag{2.5}$$

together with Eq. (2.1), we find that the electric field satisfies the *wave equation*

$$\left(\nabla^2 - \frac{1}{c^2}\frac{\partial^2}{\partial t^2}\right)\mathbf{E}(\mathbf{r},t) = 0\,. \tag{2.6}$$

Similarly, by taking the curl of Eq. (2.4) and the time derivative of Eq. (2.2) we can show that the magnetic field also satisfies the wave equation. This means that Maxwell's equations admit wave-like solutions and each component of the **E** field and **B** field satisfies the *scalar wave equation*

$$\left(\nabla^2 - \frac{1}{c^2}\frac{\partial^2}{\partial t^2}\right)\Psi(\mathbf{r},t) = 0\,. \tag{2.7}$$

The solutions of this equation are of the form:

$$\Psi(\mathbf{r},t) = \begin{cases} f\,(t \mp z/c) & \text{plane wave} \\ \frac{1}{r} f\,(t \mp r/c) & \text{spherical wave} \\ \frac{1}{\sqrt{\rho}} f\,(t \mp \rho/c) & \text{cylindrical wave} \end{cases} \tag{2.8}$$

where $\Psi(\mathbf{r},t)$ represents any component of $\mathbf{E}(\mathbf{r},t)$ or $\mathbf{B}(\mathbf{r},t)$. The particular form of the solution chosen depends on the symmetry of the problem. In describing laser propagation, we are interested in quasi-monochromatic fields (coherent light), so we desire solutions of the form

$$\Psi(\mathbf{r},t) = \Psi_o(\mathbf{r})e^{-i\omega t}. \tag{2.9}$$

If we substitute this solution into the scalar wave equation (2.7), we find the space dependent part, $\Psi_o(r)$, satisfies the *Helmholtz equation*

$$\left(\nabla^2 + \frac{\omega^2}{c^2}\right)\Psi_o(\mathbf{r}) = 0\,. \tag{2.10}$$

Perhaps the most familiar solution of this equation is the plane wave solution. We can represent a plane wave propagating in the $z$-direction by

$$\Psi_o(\mathbf{r}) = \psi_o e^{ikz}\,, \tag{2.11}$$

where $\psi_o$ is a constant and the propagation constant $k$ is related to the wavelength and angular frequency of the wave by

$$k = \frac{\omega}{c} = \frac{2\pi}{\lambda}\,. \tag{2.12}$$

The **E** field of a plane electromagnetic wave is then written as

$$\mathbf{E}(\mathbf{r},t) = \mathbf{E_o} e^{i(kz-\omega t)} . \tag{2.13}$$

and the **B** field as

$$\mathbf{B}(\mathbf{r},t) = \hat{k} \times \frac{\mathbf{E_o}}{c} e^{i(kz-\omega t)} . \tag{2.14}$$

For plane waves, $\mathbf{E_o}$ is a constant vector. These two equations satisfy Eqs. (2.2) and (2.4). Maxwell's equations (2.1) and (2.3) require

$$\hat{k} \cdot \mathbf{E}(\mathbf{r},t) = \hat{k} \cdot \mathbf{B}(\mathbf{r},t) = 0 . \tag{2.15}$$

Then the energy flow as defined by the Poynting vector

$$\mathbf{S} = \frac{1}{2\mu_o} \Re\epsilon \, (\mathbf{E}^* \times \mathbf{B}) = \frac{1}{2} \epsilon_o c E_o^2 \hat{k} \tag{2.16}$$

is in the $z$-direction as expected. Although the unidirectional propagation of plane waves is characteristic of laser beams, the fact that the wave has the same amplitude, $\Psi_o(\mathbf{r}) = \psi_o e^{ikz}$, for the entire plane $z$ = constant is not characteristic of a laser beam. In addition to a predominant direction of propagation, laser beams also have a finite extent in the transverse direction. We therefore look at other potential solutions of Eq. (2.10) that mimic these properties of laser beams.

The second important solution of Eq. (2.10) is the spherical wave, which can be written for $r \neq 0$ in the form

$$\Psi_o(\mathbf{r}) = \frac{A}{r} e^{ikr} , \tag{2.17}$$

where $A$ is a constant. This represents a wave of constant amplitude over a sphere of radius $r$. Since we are interested in the predominantly unidirectional propagation of a wave, we restrict ourselves to a small cross-section of the wave near the $z$-axis (paraxial) at a distance $z = R$ away from the origin, or the point source. For these points close to the $z$-axis, we can write $r$ as

$$r = R\left(1 + \frac{x^2 + y^2}{R^2}\right)^{1/2} \tag{2.18}$$

and since $x^2 + y^2 \ll R^2$ for the paraxial points, we can approximate $r$, using the binomial expansion, by

$$r \approx R + \frac{x^2 + y^2}{2R} . \tag{2.19}$$

The spherical wave solution on the $z$-axis at $z = R$ can then be written as

$$\Psi_o(\mathbf{r}) = \frac{A}{R} e^{ikR} e^{ik(x^2+y^2)/2R} \tag{2.20}$$

for distances far from the source. Because of its small relative magnitude compared to $R$, the second term in Eq. (2.19) can be neglected in the denominator of Eq. (2.20). It must be kept in the exponential term however, because there it is compared to a wavelength. In Eq. (2.20), $R$ is the radius of curvature of the phase fronts. We now have a solution to the Helmholtz equation which has a non-uniform amplitude in a plane perpendicular to the $z$-axis. We will see that this solution suggests very important "beam-like" solutions to the paraxial wave equation, which we derive next.

## 2.2 The Paraxial Wave Equation

We are interested in solutions that give a finite transverse extent and yet travel predominantly in the $z$-direction. To this end we propose a solution of the form

$$\Psi_o(\mathbf{r}) = \psi(\mathbf{r}) e^{ikz} \tag{2.21}$$

where $\psi(\mathbf{r})$ describes the transverse profile of the beam. Substituting this into the Helmholtz equation (2.10) and using the fact that $k = \omega/c$, we obtain

$$\left[ \left( \frac{\partial^2}{\partial x^2} + \frac{\partial^2}{\partial y^2} \right) \psi(\mathbf{r}) + 2ik \frac{\partial \psi(\mathbf{r})}{\partial z} + \frac{\partial^2 \psi(\mathbf{r})}{\partial z^2} \right] e^{ikz} = 0 \, . \tag{2.22}$$

We now assume that the $z$ dependence of $\psi(\mathbf{r})$ is slow. This means that the transverse profile of the beam does not vary significantly over distances comparable to the optical wavelength $\lambda = 2\pi/k$. In other words, the beam spreads slowly as it propagates in the $z$ direction. This assumption is known as the *paraxial approximation* and is represented mathematically by the conditions

$$\left| \frac{\partial \psi(\mathbf{r})}{\partial z} \right| \ll k \left| \psi(\mathbf{r}) \right| \, . \tag{2.23}$$

$$\left| \frac{\partial^2 \psi(\mathbf{r})}{\partial z^2} \right| \ll 2k \left| \frac{\partial \psi(\mathbf{r})}{\partial z} \right| \text{ and } \left| \nabla_{\mathbf{T}}^2 \psi(\mathbf{r}) \right| \, . \tag{2.24}$$

where the *transverse Laplacian* is given by

$$\nabla_{\mathbf{T}}^{\mathbf{2}} = \frac{\partial^2}{\partial x^2} + \frac{\partial^2}{\partial y^2} \,. \tag{2.25}$$

Under the paraxial approximation, the Helmholtz equation (2.10) leads to the *paraxial wave equation*:

$$\nabla_{\mathbf{T}}^{\mathbf{2}} \upsilon(\mathbf{r}) + 2ik\frac{\partial \upsilon(\mathbf{r})}{\partial z} = 0 \,. \tag{2.26}$$

Before we look at specific solutions to this equation, let us investigate the validity of the paraxial wave approximation. Suppose we have a wave traveling in the $x$-$z$ plane whose $k$-vector makes an angle $\theta$ with the $z$-axis. Since we can always describe a wave as a superposition of plane waves, we can represent the wave component in the $x$-$z$ plane as

$$\Psi_o(x,z) = Ae^{iksin\theta x + ikcos\theta z} = \upsilon(x,z)e^{ikz} \,. \tag{2.27}$$

where

$$\upsilon(x,z) = Ae^{iksin\theta x + ik(cos\theta - 1)z} \,. \tag{2.28}$$

We then find for each term in Eq. (2.24):

$$\frac{\partial^2 \upsilon(x,z)}{\partial z^2} = -k^2(cos\theta - 1)^2 \upsilon(x,z) \tag{2.29}$$

$$2ik\frac{\partial \upsilon(x,z)}{\partial z} = -2k^2(cos\theta - 1)\upsilon(x,z) \tag{2.30}$$

$$\frac{\partial^2 \upsilon(x,z)}{\partial x^2} = -k^2 sin^2\theta \upsilon(x,z) \tag{2.31}$$

Using the approximations $sin\theta \approx \theta$ and $cos\theta - 1 \approx \theta^2/2$, we find that Eq. (2.21) leads to the inequality

$$k^2\frac{\theta^4}{4} \ll k^2\theta^2 \qquad \Longrightarrow \qquad \frac{\theta^2}{4} \ll 1 \,. \tag{2.32}$$

Thus the paraxial approximation is good as long as this inequality is satisfied. If we say that two orders of magnitude is sufficient to call the approximation valid, then the inequality holds for $\theta < 0.2$ radian or $12^o$. This means the paraxial wave approximation is valid as long as the beam does not converge or diverge outside of a cone of $\approx 24^o$, or as long as most of the plane waves comprising the beam have their $k$-vector inside a cone of $\approx 24^o$.

## 2.3 Gaussian Beam Solutions

We now recall the spherical wave solution, Eq. (2.20) derived in Section 2.1. Since it is a solution to the Helmholtz equation (2.10) in the paraxial approximation, it must also satisfy the paraxial wave equation. We generalize the form of the spherical wave solution such that it has a Gaussian transverse profile.

$$\psi(\mathbf{r}) = Ae^{ik(x^2+y^2)/2q(z)+ip(z)} , \tag{2.33}$$

where A is a constant and we introduce the *complex beam parameter* $q(z)$ and a *complex phase shift* $p(z)$. Requiring Eq. (2.33) to be a solution of Eq. (2.26) allows us to determine the parameters $q(z)$ and $p(z)$. With $\psi(\mathbf{r})$ given by Eq. (2.33), each term in Eq. (2.26) can be written as

$$\frac{\partial^2}{\partial x^2}\psi(\mathbf{r}) = \left(\frac{ik}{q(z)} - \frac{k^2x^2}{q^2(z)}\right)\psi(\mathbf{r}) \tag{2.34}$$

$$\frac{\partial^2}{\partial y^2}\psi(\mathbf{r}) = \left(\frac{ik}{q(z)} - \frac{k^2y^2}{q^2(z)}\right)\psi(\mathbf{r}) \tag{2.35}$$

$$\frac{\partial}{\partial z}\psi(\mathbf{r}) = \left(-ik\frac{(x^2+y^2)}{2q^2(z)}\frac{dq(z)}{dz} + i\frac{dp(z)}{dz}\right)\psi(\mathbf{r}) . \tag{2.36}$$

With the help of these, we find that Eq. (2.26) becomes

$$A\left[\frac{k^2}{q^2(z)}\left(x^2+y^2\right)\left(\frac{dq(z)}{dz}-1\right) - 2k\left(\frac{dp(z)}{dz} - \frac{i}{q(z)}\right)\right]e^{ik(x^2+y^2)/2q(z)+ip(z)} = 0. \tag{2.37}$$

To satisfy this equation, we must simultaneously have

$$\frac{dq(z)}{dz} = 1 \qquad \text{and} \qquad \frac{dp(z)}{dz} = \frac{i}{q(z)} . \tag{2.38}$$

Integrating Eq. (2.38), we find

$$q(z) = q_o + z \qquad \text{where} \quad q(0) = q_o \tag{2.39}$$

$$p(z) = i\ln\frac{q_o+z}{q_o} \qquad \text{where} \quad p(0) = 0 . \tag{2.40}$$

In order to understand the physical significance of the complex beam parameter $q(z)$, we write it in terms of its real and imaginary parts by introducing two real beam

parameters $R(z)$ and $w(z)$ as

$$\frac{1}{q(z)} = \frac{1}{R(z)} + i\frac{\lambda}{\pi w^2(z)} . \tag{2.41}$$

In the plane $z = 0$ this equation leads to

$$\frac{1}{q(0)} = \frac{1}{q_o} = \frac{1}{R_o} + i\frac{\lambda}{\pi w_o^2} . \tag{2.42}$$

If we choose $z = 0$ to be the point where $R_o = \infty$, then $q_o$ is pure imaginary and we can write

$$\frac{1}{q_o} = i\frac{\lambda}{\pi w_o^2} = \frac{i}{z_o} , \tag{2.43}$$

where

$$z_o = \frac{\pi w_o^2}{\lambda} = \frac{k w_o^2}{2} . \tag{2.44}$$

Using Eqs. (2.43) and (2.44) we can rewrite Eq. (2.39) as

$$q(z) = -iz_o + z \tag{2.45}$$

and Eq. (2.41) as

$$\frac{1}{q(z)} = \frac{1}{q_o + z} = \frac{1/q_o}{1 + z/q_o} . \tag{2.46}$$

Separating the real and imaginary parts of Eq. (2.46) we find

$$\frac{1}{q(z)} = \frac{z/z_o^2}{1 + z^2/z_o^2} + i\frac{1/z_o}{1 + z^2/z_o^2} . \tag{2.47}$$

Comparing Eq. (2.47) with Eq. (2.41) we find that

$$R(z) = z + \frac{z_o^2}{z} , \tag{2.48}$$

and

$$w(z) = w_o\sqrt{\left(1 + \frac{z^2}{z_o^2}\right)} . \tag{2.49}$$

Making use of Eq. (2.43) in Eq. (2.40) we can write the expression for $p(z)$ as

$$p(z) = i\ln\left(1 + i\frac{z}{z_o}\right) \equiv i\ln\sqrt{1 + \frac{z^2}{z_o^2}} - \tan^{-1}\left(\frac{z}{z_o}\right) . \tag{2.50}$$

Finally, using Eqs. (2.41) and (2.50) in Eq. (2.33) and letting $\rho^2 = x^2 + y^2$, we can write the Gaussian beam solution as

$$\psi(\mathbf{r}) = \frac{A e^{-i \tan^{-1}(z/z_o)}}{\sqrt{1 + z^2/z_o^2}} e^{ik\rho^2/2R(z) - \rho^2/w^2(z)} . \tag{2.51}$$

In terms of the expression for $w(z)$ from Eq. (2.49) we write the full solution to the paraxial wave equation in the form

$$\Psi_o(\mathbf{r}) = \frac{A w_o}{w(z)} e^{ik\rho^2/2R(z) - \rho^2/w^2(z)} e^{i[kz - \tan^{-1}(z/z_o)]} . \tag{2.52}$$

We are now in a position to understand the physical significance of $w(z)$, $z_o$, and $R(z)$ and how they characterize Gaussian beams. If we look at the intensity of a wave of total power $P$,

$$I(\mathbf{r}) = \frac{1}{2} c\epsilon_o |E(\mathbf{r})|^2 = \frac{c\epsilon_o A^2 w_o^2}{w^2(z)} e^{-2\rho^2/w^2(z)} = \frac{2P}{\pi w^2(z)} e^{-2\rho^2/w^2(z)} , \tag{2.53}$$

we see a Gaussian distribution in the transverse direction with $w(z)$ representing the characteristic width of the beam or the beam's *spot size* at the plane intersecting the beam axis at $z$. The meaning of "spot size" is not uniform in the literature. For our purposes, we define the spot size to be $w(z)$ and therefore $2w(z)$ represents the diameter of the beam. The plane intersecting the beam axis at $z = 0$ is known as the *beam waist*. From Eq. (2.49) we see that the spot size is minimum at the beam waist

$$w(0) = w_o . \tag{2.54}$$

A diagram of the beam waist region of a Gaussian beam is shown in Fig. 2.1. The length scale over which the beam's spot size grows in the direction of propagation is determined by the quantity $z_o$, known as the *Rayleigh range*, defined by Eq. (2.44). From Eq. (2.49) we can see that

$$w(z_o) = \sqrt{2} w_o \tag{2.55}$$

so the cross section of the beam doubles over the length equal to the Rayleigh range. The distance of $2z_o$ from $-z_o$ to $z_o$ is referred to as the *confocal parameter* of the beam, the distance over which the beam remains approximately collimated.

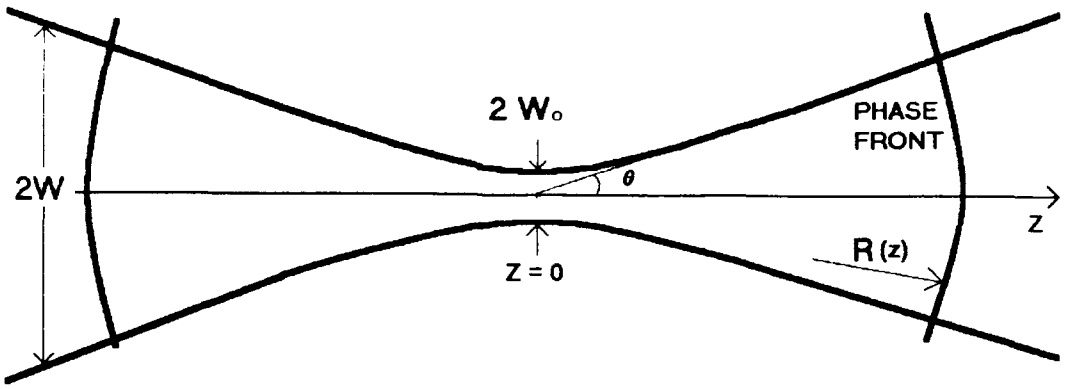


Figure 2.1: A diagram of the beam waist region of a Gaussian beam. The beam waist is the plane $z = 0$. The minimum spot size is found at the beam waist and has a diameter of $2w_o$. The angle of divergence of the beam is represented by $\theta$ and the radius of curvature of the phase fronts is given by $R(z)$.

To understand the physical significance of $R(z)$, we compare the full Gaussian beam solution, Eq. (2.52), with the spherical wave solution, Eq. (2.20) and see that $R(z)$ represents the radius of curvature of the phase front. This radius of curvature is infinite at the beam waist, where the beam is collimated. In the far field, the radius of curvature is approximately equal to $z$. By convention, for a beam traveling in the positive $z$ direction, $R(z) > 0$ for a diverging beam and $R(z) < 0$ for a converging beam. It is interesting to note that if the quantity $z_o$ and the beam waist location is known, all other information concerning the Gaussian beam at any other point in space can be determined from Eqs. (2.44) – (2.49). This means $z_o$ uniquely determines a Gaussian beam.

We saw in Section 2.2 that the paraxial approximation would be valid if the solution did not diverge at an angle greater than approximately $12^o$ (or $\approx 1/4$ radian). We solve for the beam divergence angle of the Gaussian spherical wave solution by evaluating Eq. (2.49) at $z \gg z_o$. With the help of the binomial expansion we find

$$w(z \gg z_o) \approx \frac{w_o z}{z_o} = \frac{z\lambda}{\pi w_o} . \tag{2.56}$$

The angle of divergence is expressed as

$$\theta \approx \tan\theta = \frac{w(z)}{z} = \frac{\lambda}{\pi w_o} . \tag{2.57}$$

Thus as long as the minimum spot size is larger than a few wavelengths, a condition which is fulfilled for most laser beams, the paraxial approximation is expected to hold.

The solution we have assumed in this section is the so called fundamental solution. In general, there are other solutions of the paraxial wave equation (2.26). For rectangular symmetry, there are the Hermite-Gaussian solutions, which have the form

$$\begin{aligned} \psi_{mn}(\mathbf{r}) &= A_{mn}\frac{w_o}{w(z)}H_m\left(\frac{\sqrt{2}x}{w(z)}\right)H_n\left(\frac{\sqrt{2}y}{w(z)}\right)\exp[-i(m+n+1)tan^{-1}(z/z_o)]\times \\ &\quad \exp[ik(x^2+y^2)/2R(z)-(x^2+y^2)/w^2(z)]\,. \end{aligned} \tag{2.58}$$

Here $H_n(x)$ represents a Hermite polynomial of order $n$ and argument $x$. For cylindrical symmetry, the solutions are known as Laguerre-Gaussian solutions and are of the form

$$\begin{aligned} \psi_{lm}(\mathbf{r}) &= A\sqrt{\frac{2l!}{(1+\delta_{0m})\pi(l+m)!}}\epsilon^{i(2l+m+1)}\left(\frac{\sqrt{2}\rho}{w(z)}\right)^m L_l^m\left(\frac{2\rho^2}{w^2(z)}\right) \\ &\quad \times\exp[ik\rho^2/2R(z)-\rho^2/w^2(z)+im\phi]\,, \end{aligned} \tag{2.59}$$

where $L_l^m(x)$ refers to an associated Laguerre polynomial of degree $l$. For most applications, the fundamental solution is the desired solution, and is therefore most often encountered in the literature. We now look at the effect of various optical elements on a Gaussian beam.

## 2.4 Transformation Characteristics of Gaussian Beams

We have seen that for free space propagation laser beams may be represented by a Gaussian spherical beam solution to the paraxial wave equation. We now investigate how these beams are transformed as they pass through various optical elements. Specifically, we are interested in how $q(z)$ transforms as the beam propagates.

We start with the example of free space propagation. According to Eq. (2.39), an initial beam parameter, $q_i$, will transform into the final beam parameter $q_f$ after propagating through a distance $d$ by

$$q_f = q_i + d\,. \tag{2.60}$$

If we represent this transformation by the equation

$$q_f = \frac{Aq_i + B}{Cq_i + D}. \tag{2.61}$$

we can write the coefficients in the beam transformation matrix

$$\begin{bmatrix} A & B \\ C & D \end{bmatrix} = \begin{bmatrix} 1 & d \\ 0 & 1 \end{bmatrix}. \tag{2.62}$$

We now take the example of a thin lens with a focal length $f$, which transforms a spherical wave of radius $R_i$ incident from the left into a spherical wave of radius $R_f$ exiting the lens to the right according to the equation

$$\frac{1}{R_f} = \frac{1}{R_i} - \frac{1}{f}. \tag{2.63}$$

For a Gaussian beam incident on a thin lens, we expect the radius of curvature to be transformed as in Eq. (2.63), but the spot size just to the left of the lens should be exactly the same as the spot size just to the right of the lens. We can therefore relate the transformed beam parameter, $q_f$, just after the lens to the incident beam parameter, $q_i$, just before the lens by

$$\frac{1}{q_f} = \frac{1}{q_i} - \frac{1}{f}. \tag{2.64}$$

Solving explicitly for $q_f$,

$$q_f = \frac{q_i f}{f - q_i} = \frac{q_i}{-q_i/f + 1}. \tag{2.65}$$

we can write the beam transformation matrix for a thin lens

$$\begin{bmatrix} A & B \\ C & D \end{bmatrix} = \begin{bmatrix} 1 & 0 \\ -1/f & 1 \end{bmatrix}. \tag{2.66}$$

These two specific transformations are examples of the general $ABCD$ law for Gaussian beams [15]. The transformed $q$ parameter of a Gaussian beam can be obtained from Eq. (2.61) where the coefficients are determined from the ray transfer matrices of geometric optics.

In this chapter we have reviewed the propagation of electromagnetic waves and saw how they can be used to represent laser beams. From a scalar treatment of

Maxwell's equations, we derived the paraxial wave equation. Beam-like solutions to the paraxial wave equation characterize most of the propagation characteristics of laser beams. For Gaussian beam solutions, these characteristics are determined from the complex beam parameter $q(z)$. The manner in which a Gaussian beam transforms through optical elements is determined from the ray transfer matrices of geometric optics. These matrices will play an important role as we design a laser system in the next chapter.

# Chapter 3

# Laser Design

Solid state lasers have proved to be widely tunable and simpler to use than dye lasers. They are finding increasing use in spectroscopic and nonlinear optical experiments. Because of broad tunability, in order to minimize losses, one must use crystals with Brewster windows. This presents the problem of how to compensate for the astigmatism induced by Brewster surfaces and other nonparaxial elements. For most applications, cylindrically symmetric ($TEM_{00}$) beams are needed. In this chapter we present a general method that allows us to compensate astigmatism using curved mirrors. Our objective is to design a tunable single-frequency, single-mode Ti:sapphire laser. We begin our discussion of laser system design with a comparison between standing and ring cavity designs. We then describe the stability requirements for a laser cavity and address astigmatic compensation. The problem of matching the pump mode into the cavity mode is considered next. We use our cavity design as an example. Finally, we describe various intracavity elements that can be used to make the laser unidirectional and tunable to single wavelength.

## 3.1 Ring versus Standing Wave Cavity

The first consideration in designing a laser is to choose between a standing wave or a ring cavity to optimize the particular laser system. A standing wave cavity is generally simpler in design and offers the advantage of the electromagnetic wave passing through the gain medium twice during a round trip in the cavity. One disadvantage of a standing wave cavity however is spatial hole burning. The electromagnetic field inside a standing wave cavity may be considered to be the superposition of two oppositely propagating traveling waves. The interference between these two waves sets up nodes

inside the cavity (and hence inside the gain medium) where the intensity of the electromagnetic wave goes to zero. Between two nodes is an antinode corresponding to intense fields. The result is periodic gain depletion or "holes burned" at the spacing of $\lambda/2$ inside the gain medium. Therefore, standing wave cavities do not utilize the gain completely and various grating effects can occur. The problem of spatial hole burning is overcome in a ring laser, where no standing waves exist. Another advantage of ring lasers is found in the pumping scheme. Many solid state lasers require optical pumping of the gain medium, which is often accomplished with another laser. In a standing wave cavity, part of the pump beam can be reflected back onto itself, causing interference and stability problems, especially in situations involving longitudinal pumping schemes. In a ring laser, such reflections or feedback are not present. A disadvantage of a ring laser is the directional mode competition which may result in large intensity fluctuations. This directional competition can be suppressed by introducing a Faraday rotator and waveplate assembly as described in Section 3.5.2. Finally, the design of a ring laser generally affords for easier introduction of intracavity elements with the second beam waist and extra space available in the long arm. One beam waist is in the middle of the crystal (gain medium) and the other is at the center of the long arm and is available for elements such as atomic vapor cells and nonlinear crystals. For our specific needs, we opted for a ring cavity for our Ti:sapphire laser.

## 3.2 Stable Cavity: The Ray Matrix Approach

Once the choice between a standing wave and a ring cavity has been made, the stability of the laser cavity must be addressed. While certain high power applications may require the use of an unstable resonator, most spectroscopic applications involve stable laser cavities. We address only this type of cavities in this section. Although we look at the specifics of a ring cavity, the general procedure outlined applies to standing wave cavities as well. To determine the stability of a cavity, we must first review some basics from geometrical optics.

Light propagation can be described in terms of rays, which are geometric curves representing the direction of propagation of energy. In most cases we are interested

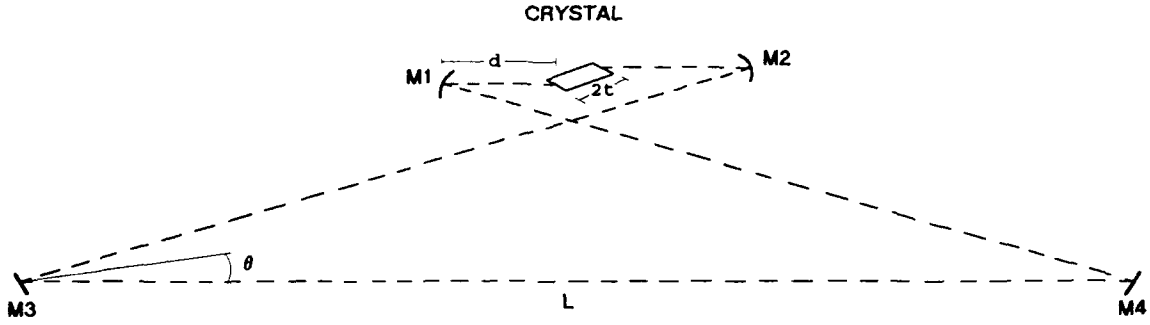


Figure 3.1: A basic ring laser design consisting of a crystal of length $2t$, two curved mirrors with radius of curvature $R$, and two flat mirrors to steer the beam in the long arm. The distance between the curved mirrors and the faces of the crystal is $d$ and the length of the long arm from M1 to M2 is $L$. The crystal has Brewster surfaces at both ends, and the long and short arms are taken to be parallel. Angle $\theta$ is one half the fold angle of the laser and represents the angle of incidence for all cavity mirrors.

in light propagating predominantly in a single direction. We chose this direction to be the $z$-axis and refer to it as the *optic* or *cavity* axis. At any given point in space, we can then describe a light ray with two parameters. The lateral displacement off the $z$-axis at a specific $z$ location is given by $r(z)$ and the slope of the ray at $z$ is $dr/dz = r'(z)$. If we form a column vector from these two parameters, we can obtain the ray at a distance $z$ from the original ray (at $z_o$) by the transformation

$$\begin{bmatrix} r(z) \\ r'(z) \end{bmatrix} = \begin{bmatrix} A & B \\ C & D \end{bmatrix} \begin{bmatrix} r(z_o) \\ r'(z_o) \end{bmatrix} \tag{3.1}$$

where the $ABCD$ transformation matrix (or the ray matrix) depends on the optical element through which the ray passes. The specific parameters for various optical elements can be derived from the laws of geometric optics and are available in many optics and laser textbooks [16, 17, 18]. The matrices most often used in designing laser cavities are reproduced in Table 3.1 for reference.

The round trip matrix represents the transformation of a ray after one round trip through the cavity. This matrix is found by multiplying in sequence the matrices of each optical element that is encountered by a ray in one round trip. An analysis of this matrix gives us the stability region, beam spot size, and beam waist locations inside the cavity. For a basic ring laser as depicted in Fig. 3.1, we have two beam waists, one at the center of the crystal and one in the center of the long arm. A knowledge

| | |
|---|---|
| Free space propagation of distance $d$ inside a medium of refractive index $n$. | $\begin{bmatrix} 1 & d/n \\ 0 & 1 \end{bmatrix}$ |
| Thin lens with focal length $f$. | $\begin{bmatrix} 1 & 0 \\ -1/f & 1 \end{bmatrix}$ |
| Curved mirror with radius of curvature $R$ at an angle of incidence $\theta$, *tangential plane*. | $\begin{bmatrix} 1 & 0 \\ -2/Rcos\theta & 1 \end{bmatrix}$ |
| Curved mirror with radius of curvature $R$ at an angle of incidence $\theta$, *sagittal plane*. | $\begin{bmatrix} 1 & 0 \\ -2cos\theta/R & 1 \end{bmatrix}$ |
| Flat interface between air and medium with refractive index $n$ at Brewster's angle, *tangential plane*. | $\begin{bmatrix} n & 0 \\ 0 & 1/n \end{bmatrix}$ |
| Flat interface between air and medium with refractive index $n$ at Brewster's angle, *sagittal plane*. | $\begin{bmatrix} 1 & 0 \\ 0 & 1 \end{bmatrix}$ |

Table 3.1: Transformation Ray Matrices for Optical Elements

of the beam waist location and spot size is necessary for mode matching and efficient pumping of the cavity mode volume by the pump laser. Using the ray transformation matrices from Table 3.1, we find the round trip matrix in the tangential plane for starting at the center of the crystal to be

$$\begin{bmatrix} A_t^c & B_t^c \\ C_t^c & D_t^c \end{bmatrix} = \begin{bmatrix} 1 & t/n \\ 0 & 1 \end{bmatrix} \begin{bmatrix} n & 0 \\ 0 & 1/n \end{bmatrix} \begin{bmatrix} 1 & d \\ 0 & 1 \end{bmatrix} \begin{bmatrix} 1 & 0 \\ -2/R\cos\theta & 1 \end{bmatrix} \times \begin{bmatrix} 1 & L \\ 0 & 1 \end{bmatrix} \begin{bmatrix} 1 & 0 \\ -2/R\cos\theta & 1 \end{bmatrix} \begin{bmatrix} 1 & d \\ 0 & 1 \end{bmatrix} \begin{bmatrix} 1/n & 0 \\ 0 & n \end{bmatrix} \begin{bmatrix} 1 & t/n \\ 0 & 1 \end{bmatrix} . \quad (3.2)$$

Here $2t$ is the length of the crystal along the optic axis, $d$ is the distance between either curved mirror and the face of the crystal, and $L$ is the total length of the long arm (free space propagation). For notational purposes, the subscript $t$ refers to the *tangential* or the horizontal plane containing the optic axis and the subscript $s$ refers to the *sagittal* or vertical plane containing the optic axis. We will use the superscript $c$ to refer to the beam waist at the center of the *crystal* and the superscript $l$ to refer to the beam waist at the center of the *long arm*. If we define the optical path length between the two curved mirrors in the tangential plane as

$$2l_t = \frac{2t}{n^3} + 2d , \quad (3.3)$$

then the round trip matrix is simplified and its elements can be written in the form

$$A_t^c = 2\left(1 - \frac{L}{R\cos\theta}\right)\left(1 - \frac{2l_t}{R\cos\theta}\right) - 1 , \quad (3.4)$$

$$B_t^c = n^2\left(1 - \frac{2l_t}{R\cos\theta}\right)\left[2l_t + L\left(1 - \frac{2l_t}{R\cos\theta}\right)\right] , \quad (3.5)$$

$$C_t^c = -\frac{4}{n^2 R\cos\theta}\left(1 - \frac{L}{R\cos\theta}\right) , \quad (3.6)$$

$$D_t^c = A_t^c . \quad (3.7)$$

For the sagittal plane, each $R\cos\theta$ term is replaced by $R/\cos\theta$ and the Brewster's interface matrices become unit matrices. Defining the optical path length between the two curved mirrors in the sagittal plane as

$$2l_s = \frac{2t}{n} + 2d . \quad (3.8)$$

the elements of the round trip matrix for the sagittal plane can be written

$$A_s^c = 2\left(1 - \frac{L\cos\theta}{R}\right)\left(1 - \frac{2l_s\cos\theta}{R}\right) - 1 . \tag{3.9}$$

$$B_s^c = \left(1 - \frac{2l_s\cos\theta}{R}\right)\left[2l_s + L\left(1 - \frac{2l_s\cos\theta}{R}\right)\right] . \tag{3.10}$$

$$C_s^c = -\frac{4\cos\theta}{R}\left(1 - \frac{L\cos\theta}{R}\right) . \tag{3.11}$$

$$D_s^c = A_s^c . \tag{3.12}$$

Once each element of the round trip matrix is known for a given plane, the stability conditions can be derived. Since the ray is transformed by the $ABCD$ matrix in each round trip through the cavity, we are interested in the range of the parameters that allow $r_f(z_o)$ and $r'_f(z_o)$ to remain finite as N goes to $\infty$ in the matrix equation

$$\begin{bmatrix} r_f(z_o) \\ r'_f(z_o) \end{bmatrix} = \begin{bmatrix} A & B \\ C & D \end{bmatrix}^N \begin{bmatrix} r_i(z_o) \\ r'_o(z_o) \end{bmatrix} . \tag{3.13}$$

For this to be the case, the eigenvalues of the round trip matrix must be less than or equal to unity. This leads to the range of parameters or *region of stability* defined by the inequality

$$-1 \leq m \leq 1 , \tag{3.14}$$

where the parameter $m$ is given by:

$$m = \frac{A + D}{2} . \tag{3.15}$$

A complete derivation of the region of stability using eigenrays and eigenvalues of the round trip matrix can be found in [17, pages 599–602]. For our round trip matrix, $A = D$, so $m = A$ and the stability condition becomes

$$-1 \leq A \leq 1 . \tag{3.16}$$

This condition must be satisfied simultaneously for both the tangential and sagittal planes. We are interested in near confocal spacing between the curved mirrors. In order to investigate the sensitivity of cavity stability in the vicinity of confocal spacing,

we introduce a sensitivity variable $\delta$ by writing the actual distance between the curved mirrors as

$$2l \equiv 2d + 2t = R + \delta \,. \tag{3.17}$$

where $R$ is the radius of curvature of the curved mirrors. In terms of the optical path lengths $2l_t$ and $2l_s$ introduced earlier, we can write

$$2l_t = R + \delta_t - 2t\left(1 - \frac{1}{n^3}\right) = R + \delta_t - 2t_t \,. \tag{3.18}$$

and

$$2l_s = R + \delta_s - 2t\left(1 - \frac{1}{n}\right) = R + \delta_s - 2t_s \,. \tag{3.19}$$

where $\delta_t$ represents the $\delta$ variable in the tangential plane, $\delta_s$ represents the $\delta$ variable in the sagittal plane. We also introduce the quantities $t_t$ and $t_s$ by

$$t_t = t\left(1 - \frac{1}{n^3}\right) \,, \tag{3.20}$$

and

$$t_s = t\left(1 - \frac{1}{n}\right) \,. \tag{3.21}$$

Using Eqs. (3.18) and (3.19) in Eqs. (3.4) and (3.9), we obtain the region of stability defined by Eq. (3.16) in terms of $\delta$ for each of the planes

$$2t_t - R(1 - cos\theta) \leq \quad \delta_t \quad \leq 2t_t + \frac{R^2 cos\theta - LR(1 - cos\theta)}{L - Rcos\theta} \,. \tag{3.22}$$

$$2t_s - R\left(\frac{1 - cos\theta}{cos\theta}\right) \leq \quad \delta_s \quad \leq 2t_s + \frac{R^2 + LR(1 - cos\theta)}{Lcos\theta - R} \,. \tag{3.23}$$

Figure 3.2 shows the region of stability for both the tangential and sagittal planes as a function of the variables $\delta$ and $L$, the free space propagation length. The angle of incidence is $\theta = 15°$ and the radius of curvature of the cavity mirrors is $R = 10$ cm. Figure 3.3 shows the region of stability as a function of the angle of incidence $\theta$ and the sensitivity variable $\delta$ for a free space propagation length $L = 100$ cm and $R = 10$ cm. For both figures, the upper boundary of stability in the tangential plane is represented by the dashed line given by the equation

$$\delta_{t_{max}} = 2t_t + \frac{R^2 cos\theta - LR(1 - cos\theta)}{L - Rcos\theta} \,. \tag{3.24}$$

The lower boundary of stability in the tangential plane is shown by the dotted line given by the equation

$$\delta_{t_{min}} = 2t_t - R(1 - cos\theta) \ . \tag{3.25}$$

The region between these two curves is the region of cavity stability for the tangential plane. For the sagittal plane, the upper boundary of stability is represented by the solid line given by the equation

$$\delta_{s_{max}} = 2t_s + \frac{R^2 + LR(1 - cos\theta)}{Lcos\theta - R} \ . \tag{3.26}$$

The lower boundary of the sagittal plane is given by

$$\delta_{s_{min}} = 2t_s - R\left(\frac{1 - cos\theta}{cos\theta}\right) \ , \tag{3.27}$$

and is shown by the dot-dashed line. The region between these two curves is the region of stability for the sagittal plane.

A cavity is stable in both planes where the tangential and sagittal regions of stability overlap. By choosing a value for $\delta$ from this region, a stable cavity can be designed for a given angle of incidence $\theta$ and free space propagation length $L$ by setting the distance between the two curved mirrors equal to $2l$ as defined by Eq. (3.17).

In order to determine the spot size at the beam waist in the long arm, we must determine the round trip matrix from the center of the long arm. Using a procedure similar to that used to obtain Eqs. (3.4)-(3.7) and Eqs. (3.9)-(3.12), we find the elements of the round trip matrix starting at the center of the long arm for the tangential plane to be

$$A_t' = \left(1 - \frac{L}{Rcos\theta}\right)\left(1 - \frac{4l_t}{Rcos\theta}\right) - \frac{L}{Rcos\theta} \ . \tag{3.28}$$

$$B_t' = \left(1 - \frac{L}{Rcos\theta}\right)\left[L + 2l_t\left(1 - \frac{L}{Rcos\theta}\right)\right] \ . \tag{3.29}$$

$$C_t' = -\frac{4}{Rcos\theta}\left(1 - \frac{2l_t}{Rcos\theta}\right) \ . \tag{3.30}$$

$$D_t' = A_t' \ . \tag{3.31}$$

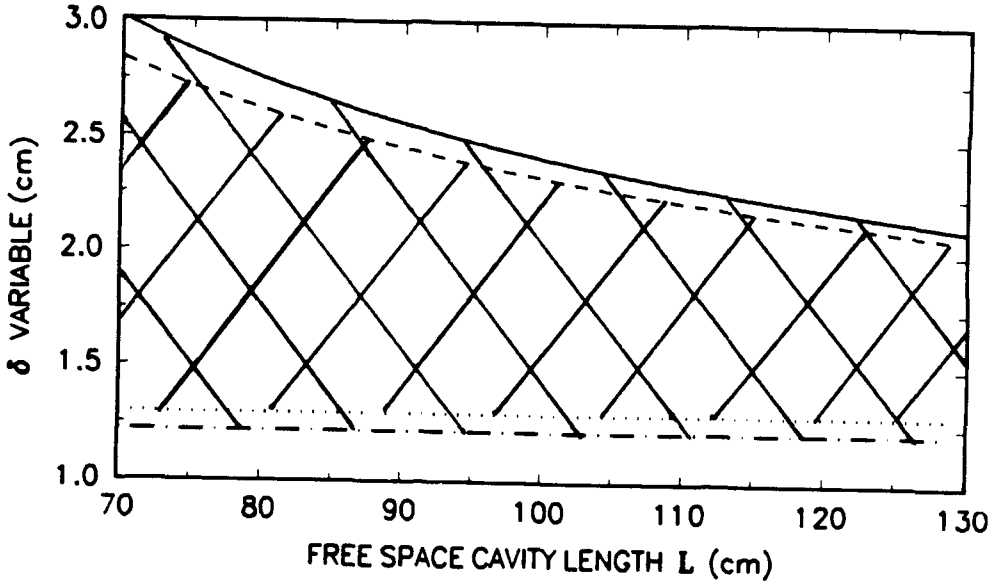


Figure 3.2: The stability region for a ring laser as a function of the sensitivity variable $\delta$ and the free space propagation length $L$. The stability region in the sagittal plane is the area between the solid and dot-dashed curves. These curves represent Eqs. (3.26) and (3.27) respectively. For the tangential plane, the region of stability is the area between the dashed and dotted curves, representing Eqs. (3.24) and Eq. (3.25). A cavity is stable in the region where the stability regions of both planes overlap. For these curves, the angle of incidence is $\theta = 15°$ and $R = 10$ cm.

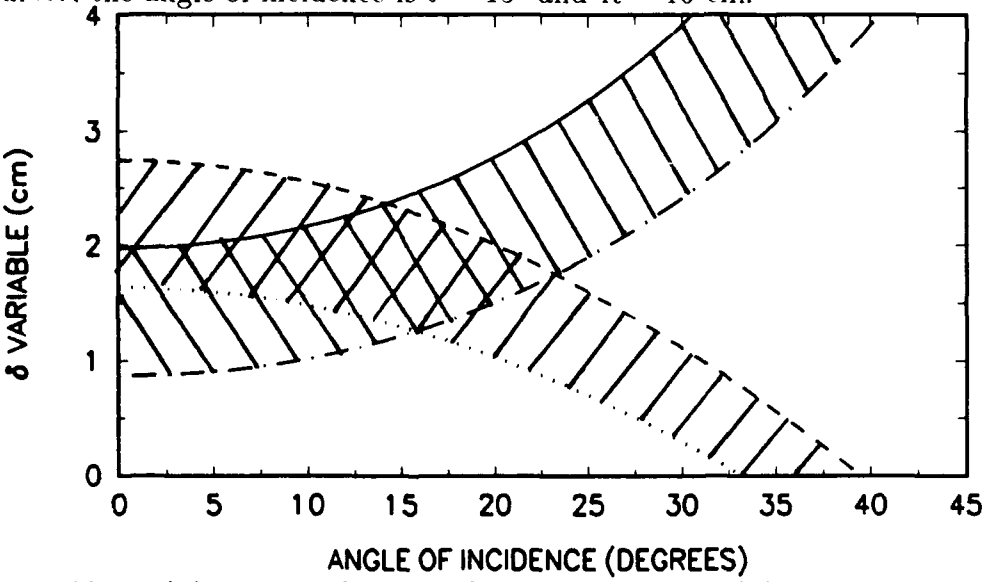


Figure 3.3: The stability region for a ring laser as a function of the sensitivity variable $\delta$ and the angle of incidence $\theta$. The stability region in the sagittal plane is the area between the solid and dot-dashed curves. These curves represent Eqs. (3.26) and (3.27) respectively. For the tangential plane, the region of stability is the area between the dashed and dotted curves, representing Eqs. (3.24) and Eq. (3.25). A cavity is stable in the region where the stabilities of both planes overlap. For these curves, the length of the long arm $L$ is 100 cm.

Similarly, the matrix elements in the sagittal plane are

$$A_s^l = \left(1 - \frac{L\cos\theta}{R}\right)\left(1 - \frac{4l_s\cos\theta}{R}\right) - \frac{L\cos\theta}{R} , \tag{3.32}$$

$$B_s^l = \left(1 - \frac{L\cos\theta}{R}\right)\left[L + 2l_s\left(1 - \frac{L\cos\theta}{R}\right)\right] , \tag{3.33}$$

$$C_s^l = -\frac{4\cos\theta}{R}\left(1 - \frac{2l_s\cos\theta}{R}\right) , \tag{3.34}$$

$$D_s^l = A_s^l . \tag{3.35}$$

The expressions for the round trip ray transformation matrices derived in this section will allow us to determine the size of the Gaussian beam waists inside the cavity. This information will be used to analyze and compensate for astigmatism in the beam profile, as we now show.

## 3.3 Intracavity Beam Waists: Astigmatic Compensation

As seen from Table 3.1, the transformation of a Gaussian beam at a curved mirror and at an interface between media of different indices of refraction is different for the tangential and sagittal planes. The tangential plane is the plane of incidence. The sagittal plane is perpendicular to the plane of incidence. This difference in transformation between planes is one source of astigmatism in laser systems. Nonnormal incidence at curved mirrors is another source of astigmatism. The result is an asymmetric transverse beam profile, which is usually undesirable.

In this section we describe a method for determining the spot size and the location of the cavity beam waists. We then describe a technique for compensating the astigmatism generated in the intracavity beam by the Brewster windows and curved mirrors for the cavity shown in Fig. 3.1. A method for compensating astigmatism in a standing wave cavity composed of three curved mirrors can be found in [19].

In Section 2.4 we saw that the coefficients of a ray matrix can be used to determine the transformation of the complex Gaussian beam parameter $q(z)$. For a stable cavity, after one round trip, we require $q_f = q_i = q_o$ in Eq. (2.61). This leads to

$$q_o = \frac{Aq_o + B}{Cq_o + D} . \tag{3.36}$$

or

$$C q_o^2 + (D - A) q_o - B = 0. \tag{3.37}$$

Solving for $1/q_o$ we find

$$\frac{1}{q_o} = \frac{D - A}{2B} \pm \frac{\sqrt{D^2 - 2AD + A^2 + 4CB}}{2B}. \tag{3.38}$$

Since the determinant of each individual ray transfer matrix is equal to one, so also must be the determinant of the round trip matrix

$$AD - CB = 1 . \tag{3.39}$$

Using Eq. (3.39) in Eq. (3.38) we find that the complex beam parameter $q_o$ is given by

$$\frac{1}{q_o} = \frac{D - A}{2B} \pm i\frac{\sqrt{4 - (A + D)^2}}{2B} . \tag{3.40}$$

Recalling that $1/q_o$ is pure imaginary at a beam waist, we see that $A = D$ for the round trip matrix starting at the location of one of the beam waists. For asymmetric cavities, one can solve for the location of the beam waists by allowing the starting point for the round trip matrix to be represented by a variable and then requiring that $A = D$. In the case of symmetric cavities, the waist location can be found by symmetry. For the cavity shown in Fig. 3.1, the beam waists are located at the center of the crystal and the long arm as confirmed by Eqs. (3.7), (3.12), (3.31), and (3.35).

Another method for defining stable resonators is suggested by Eq. (3.40). By requiring that the beam waist remain real, we obtain the condition

$$(A + D)^2 \leq 4 , \tag{3.41}$$

for stability. This condition is equivalent to

$$-1 \leq \frac{A + D}{2} \leq 1 \quad \Longrightarrow \quad -1 \leq m \leq 1 , \tag{3.42}$$

in agreement with the stability requirement Eq. (3.14) found in Section 3.2 using eigenray analysis.

To determine the spot size at the beam waist, we recall Eq. (2.42) from Section 2.3. We then find

$$\frac{i\lambda}{\pi w_o^2} = i\frac{\sqrt{1-(A+D)^2}}{2B} . \tag{3.43}$$

Using the fact that $A = D$, the spot size of the beam at its waist in terms of the ray matrix elements can be written as

$$w_o = \left[\frac{\lambda B}{\pi\sqrt{1-A^2}}\right]^{1/2} . \tag{3.44}$$

Using the expressions for $A$ and $B$ given in Eqs. (3.4), (3.5), (3.9) and (3.10), the spot size at the beam waist at the center of the crystal in the tangential plane is

$$w_{ot}^c = \left[\frac{\lambda n^2}{2\pi}\sqrt{\frac{\left(\frac{2l_t}{Rcos\theta}-1\right)\left[2l_t + L\left(1-\frac{2l_t}{Rcos\theta}\right)\right]Rcos\theta}{\left(\frac{L}{Rcos\theta}-1\right)}}\right]^{1/2} . \tag{3.45}$$

and for the sagittal plane it is

$$w_{os}^c = \left[\frac{\lambda}{2\pi}\sqrt{\frac{\left(\frac{2l_s cos\theta}{R}-1\right)\left[2l_s + L\left(1-\frac{2l_s cos\theta}{R}\right)\right]R}{\left(\frac{Lcos\theta}{R}-1\right)cos\theta}}\right]^{1/2} . \tag{3.46}$$

Similar calculations at the beam waist in the long arm using the expressions for $A$ and $B$ given in Eqs. (3.28), (3.29), (3.32) and (3.33) yield

$$w_{ot}^l = \left[\frac{\lambda}{2\pi}\sqrt{\frac{\left(\frac{L}{Rcos\theta}-1\right)\left[L + 2l_t\left(1-\frac{L}{Rcos\theta}\right)\right]Rcos\theta}{\left(\frac{2l_t}{Rcos\theta}-1\right)}}\right]^{1/2} . \tag{3.47}$$

for the spot size in the tangential plane and

$$w_{os}^l = \left[\frac{\lambda}{2\pi}\sqrt{\frac{\left(\frac{Lcos\theta}{R}-1\right)\left[L + 2l_s\left(1-\frac{Lcos\theta}{R}\right)\right]R}{\left(\frac{2l_s cos\theta}{R}-1\right)cos\theta}}\right]^{1/2} . \tag{3.48}$$

for the spot size in the sagittal plane.

In general, one finds that the beam waist spot sizes in the two planes are not equal $w_{ot} \neq w_{os}$. However, we note that the spot size at the beam waists depend on the adjustable variables $\theta$, $L$, and $\delta$. Therefore, by adjusting the curved mirror

spacing $2l$, the angle $\theta$, and the cavity free space length $L$, we can find a regime where astigmatism is minimized, or possibly removed, at least at one of the beam waists. In the ideal situation, we want a symmetric beam both inside the crystal and in the long arm. But since this may not be possible, or even desirable for all applications, one must find the parameters that best fit a particular design. In most cases, the output beam is required to have a cylindrically symmetric transverse profile. If the output comes from one of the flat mirrors steering the long arm, then we try to achieve $w_{ot}' = w_{os}'$ in the long arm by choosing the proper values for $\delta$, angle $\theta$, and free space length $L$, for the given values of crystal length $2t$, index of refraction $n$, and radius of curvature $R$ of the curved mirrors.

A plot of the spot size (beam radius) at the center of the crystal and at the center of the long arm is shown in Fig. 3.4. The variation of the spot size is shown as a function of the free space length $L$ for an angle of incidence $\theta = 15.5°$. Figure 3.5 shows the spot size variation as a function of angle of incidence $\theta$ for a free space length $L = 100$ cm. For both figures, the radius of curvature $R = 10$ cm, $\delta = 1.5$ cm, and $\lambda = 780$ nm, representing the average wavelength of laser radiation inside the cavity. The solid curve shows the spot size in the sagittal plane at the center of the long arm as given by Eq. (3.48). The dotted curve shows the spot size in the tangential plane in the long arm as given by Eq. (3.47). For the beam waist at the center of the crystal, the spot size in the tangential plane is depicted by the dashed curve and in the sagittal plane by the dot-dashed curve. These curves represent Eqs. (3.45) and (3.46) respectively. From Figs. 3.4 and 3.5, we see that for a free space length of $L = 100$ cm, angle of incidence $\theta = 15.5°$ and $\delta = 1.5$ cm, the spot size in each plane at the beam waist in the long arm are equal. Therefore, under these conditions, the astigmatism in the long arm is fully compensated and the beam in the long arm is circularly symmetric.

Since we chose to compensate for the astigmatism in the long arm, the transverse profile of the beam inside the crystal remains asymmetric. This astigmatism must be kept in mind when addressing the problem of matching the pump beam mode into the cavity mode. This is the subject of the next section.

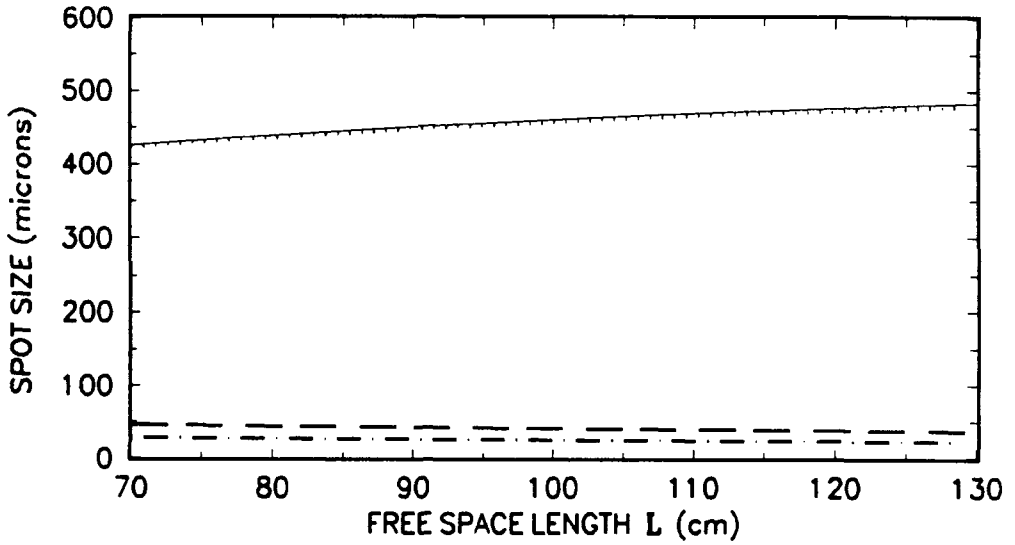


Figure 3.4: Variation of the spot size $w_o$ at the two intracavity beam waists as a function of $L$, the length of the long arm. For the beam waist in the long arm, the dotted curve represents $w_o$ in the tangential plane as given by Eq. (3.47) and the solid curve shows $w_o$ in the sagittal plane given by Eq. (3.48). For the beam waist at the center of the crystal, the dashed curve represents $w_o$ in the tangential plane as given in Eq. (3.45) and the dot-dashed curve shows $w_o$ in the sagittal plane according to Eq. (3.46). For this plot, the angle of incidence is 15°, $R = 10$ cm, $\delta = 1.5$ cm, and $\lambda = 780$ nm.

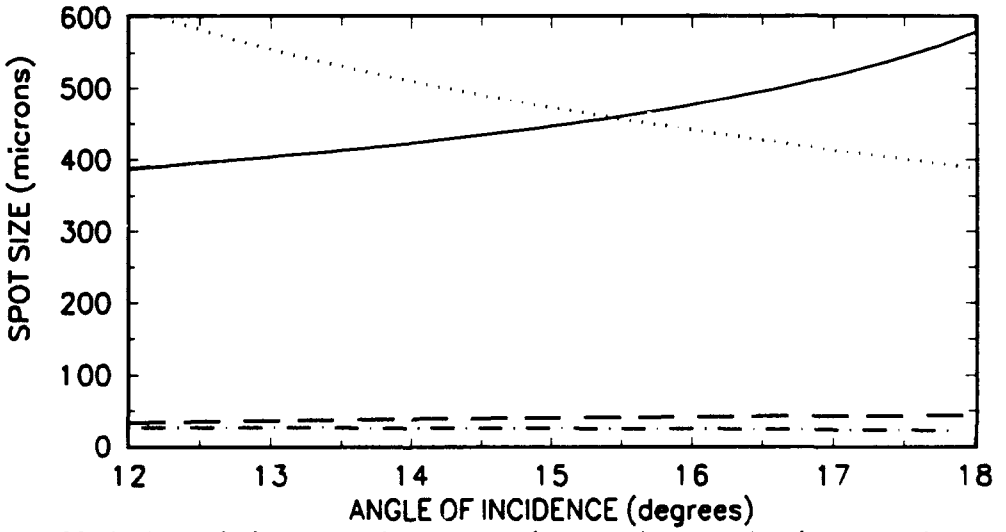


Figure 3.5: Variation of the spot size $w_o$ at the two intracavity beam waists as a function of the angle of incidence $\theta$ for a free space propagation length $L = 100$ cm. For the beam waist in the long arm, the dotted curve represents $w_o$ in the tangential plane as given by Eq. (3.47) and the solid curve shows $w_o$ in the sagittal plane given by Eq. (3.48). For the beam waist at the center of the crystal, the dashed curve represents $w_o$ in the tangential plane as given in Eq. (3.45) and the dot-dashed curve shows $w_o$ in the sagittal plane according to Eq. (3.46). For this plot, $R = 10$ cm, $\delta = 1.5$ cm, and $\lambda = 780$ nm.

## 3.4 Mode Matching

Having determined the beam waists and spot sizes, we now address the problem of coupling the pump energy as efficiently as possible into the fundamental mode inside the cavity. For this to occur, we require the pump beam spot size and waist to coincide with the cavity mode beam waist and spot size as much as possible. Our initial treatment of the problem assumes a symmetric spot size at the beam waist. In Section 3.3 we saw that this is not the case for our cavity. We therefore conclude this section with a technique to introduce astigmatism in the pump beam to better match the spot size inside the crystal. Our objective is to optimize the spatial mode matching of the pump and intracavity beams. A detailed investigation of the influence of this spatial mode matching on the efficiency of longitudinally pumped solid state lasers can be found in [20].

The theory of mode matching two Gaussian beams is developed in [15]. The basic problem consists of placing a focusing lens in the path of a Gaussian beam to generate a second beam waist at a predetermined point and with a predetermined spot size. We call the distance from the first beam waist to the lens $d_1$ and the distance to the second beam waist $d_2$. Using the transformation matrices from Table 3.1, we determine the transformation matrix for a Gaussian beam traveling a distance of $d_1$, then passing through a lens of focal length $f$, and finally through a distance of $d_2$. The resulting matrix is

$$\begin{bmatrix} A & B \\ C & D \end{bmatrix} = \begin{bmatrix} 1 - d_2/f & d_1 + d_2 - d_1 d_2/f \\ -1/f & 1 - d_1/f \end{bmatrix} . \tag{3.49}$$

Recalling Eq. (2.61), we relate the initial beam parameter $q_1$ to the final beam parameter $q_2$ by

$$q_2 = \frac{(1 - d_2/f)\, q_1 + d_1 + d_2 - d_1 d_2/f}{-q_1/f + 1 - d_1/f} . \tag{3.50}$$

Requiring the initial and final points of the transformation to be beam waists, we use Eq. (2.43), which describes the complex beam parameter $q_o$ at the beam waist, to write

$$q_1 = \frac{i\pi w_1^2}{\lambda} \qquad \text{and} \qquad q_2 = \frac{i\pi w_2^2}{\lambda} . \tag{3.51}$$

Here $w_1$ is the spot size at the original beam waist of the pump beam (inside the pump laser) and $w_2$ is the "transformed" spot size of the pump beam at the second beam waist (inside the cavity). Substituting the expressions from Eq. (3.51) into Eq. (3.50), we obtain

$$\left(\frac{\pi w_1 w_2}{\lambda}\right)^2 \frac{1}{f} + \frac{i\pi w_2^2}{\lambda}\left(1 - \frac{d_1}{f}\right) = d_1 + d_2 - \frac{d_1 d_2}{f} + \frac{i\pi w_1^2}{\lambda}\left(1 - \frac{d_2}{f}\right) . \qquad (3.52)$$

Equating the imaginary parts of Eq. (3.52), we find

$$\frac{f - d_1}{f - d_2} = \frac{w_1^2}{w_2^2} . \qquad (3.53)$$

and equating the real parts of Eq. (3.52) gives

$$(f - d_1)(f - d_2) = f^2 - f_o^2 . \qquad (3.54)$$

Here we have defined the *characteristic focal length*

$$f_o = \frac{\pi w_1 w_2}{\lambda} . \qquad (3.55)$$

To satisfy both Eqs. (3.53) and (3.54) simultaneously, we require

$$f > f_o . \qquad (3.56)$$

This means that if a pump beam having a spot size of $w_1$ at its original beam waist is to be matched onto a second beam waist of spot size $w_2$, it must be focused through a lens (or focusing system) with a focal length greater than the characteristic focal length defined by Eq. (3.55). We now look at the mode matching requirements of our laser system.

The problem for our laser system is to find the optimum position and focal length of a lens to focus the pump beam into the beam waist at the center of the crystal. Collinear pumping of the crystal is desired to optimize energy transfer from the pump source and simplicity of design. This requires the pump to be focused through one of the cavity curved mirrors. A schematic of the various elements and distances involved in our mode matching problem are shown in Fig. 3.6. The focusing lens has a focal length $f_1$ and the mirror has a focal length of $f_2$. They are separated by a distance $a$.

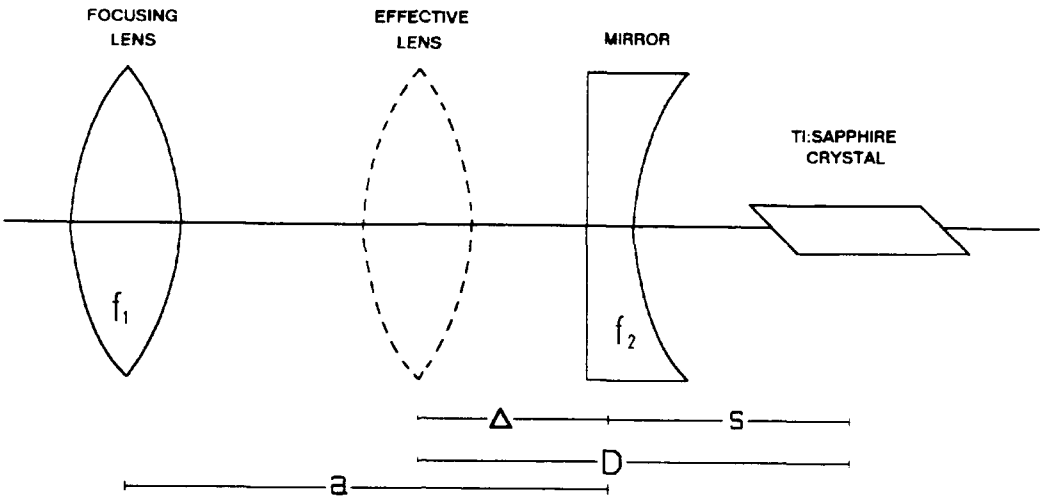


Figure 3.6: A schematic of the optical elements used in matching the spot size of the pump beam to the cavity spot size at the beam waist at the center of the crystal. The lens has a focal length $f_1$ and the mirror has a focal length of $f_2$. These elements are separated by the distance $a$. The *effective lens* is depicted with dash lines and has a focal length represented by $D$. The distance between the cavity mirror and the center of the crystal is $s$ and $\Delta$ is the distance between the effective focusing lens and the cavity mirror.

From basic optics [21], we know the effective focal length of two optical elements with focal lengths $f_1$ and $f_2$ separated by a distance $a$ is given by

$$\frac{1}{f_{eff}} = \frac{1}{f_1} + \frac{1}{f_2} - \frac{a}{f_1 f_2} . \tag{3.57}$$

The location of the "effective lens" is a distance

$$\Delta = \frac{a f_2}{f_1 + f_2 - a} \tag{3.58}$$

from the second element (cavity mirror). For our particular application, we can only vary the position of the lens, so we solve Eq. (3.57) for $f_1$

$$f_1 = \frac{f_2 - a}{f_2/f_{eff} - 1} , \tag{3.59}$$

to estimate the focal length requirement of the matching lens. To match a beam waist with spot size $w_1$ to a beam waist with spot size $w_2$ using a lens as depicted in Fig. 3.6, the effective focal length obtained from the "focusing system" must be greater than

the characteristic length $f_o$ defined by Eq. (3.55). Because of space limitations, one should select a lens with as small a focal length as possible while still meeting all other design requirements. The stability requirements outlined in Section 3.2 often place stringent requirements on this focusing lens, since the cavity mirror must be a minimum distance from the center of the crystal. Also, very small changes in the $\delta$ variable defined in Eq. (3.17) can result in large changes in the spot size at the center of the crystal. These changes in turn result in large changes in the mode matching requirements.

Taking our cavity design as an example, we obtain a value for the characteristic focal length $f_o$ as follows. Pumping with all lines from an argon ion laser, we take the average wavelength to be $\lambda = 500$ nm. Matching a beam waist spot size of 1.8 mm from the pump laser to an average spot size at the beam waist inside the crystal of 25 microns, we find

$$f_o \approx 28 \text{ cm} . \tag{3.60}$$

Solving Eq. (3.59) assuming $f_{eff} = f_o$ and $f_2 = -5$ cm, from a 10 cm concave cavity end mirror, we obtain the minimum focal length for the lens to be

$$f_{1_{min}} \approx 4 + \frac{4}{5}a . \tag{3.61}$$

We see that the minimum focal length depends on the minimum acceptable spacing between the lens and the cavity mirror. Assuming we want a minimum of 5 cm from the mirror to the lens for mounting and adjusting, we have a minimum focal length of

$$f_{1_{min}} \approx 8 \text{ cm} \tag{3.62}$$

for the focusing lens in our mode matching problem. For our laser system, a 10 cm achromatic lens was selected to meet the minimum $f_1$ requirements, and allow for variations in the pump laser, the value of $\delta$, spot sizes and cavity configurations.

The position of the "effective lens" from the beam waist inside the crystal is determined from the formula

$$D = \Delta + s = f_{eff} \pm \frac{w_2}{w_1}\sqrt{f_{eff}^2 - f_o^2} . \tag{3.63}$$

where $w_1$ is being matched to $w_2$. The distance $s$ between the cavity mirror and the center of the crystal is determined by the value of $\delta$ according to Eq. (3.17). Since this value is determined from the stability requirements of Eqs. (3.22) and (3.23), we consider it to be a constant for the mode matching problem. The value of $s$ is given by

$$s = \frac{1}{2}(R + \delta) \ , \tag{3.64}$$

where $R$ is the radius of curvature of the cavity mirror in the focusing system and $\delta$ is chosen from the stability diagrams (see Figs. 3.2 and 3.3).

To find the position of the focusing lens, we first solve Eq. (3.57) for $f_{eff}$ explicitly

$$f_{eff} = \frac{f_1 f_2}{f_1 + f_2 - a} \tag{3.65}$$

Using Eqs. (3.65) and (3.58) we rewrite Eq. (3.63) as

$$\frac{a f_2}{f_1 + f_2 - a} + s = \frac{f_1 f_2}{f_1 + f_2 - a} \pm \frac{w_2}{w_1}\sqrt{\left(\frac{f_1 f_2}{f_1 + f_2 - a}\right)^2 - f_o^2} \ . \tag{3.66}$$

In most applications, $w_2 \ll w_1$ and $f_{eff} \approx f_o$, so we neglect the second term and solve for $a$

$$a \approx \frac{f_1 f_2 - s(f_1 + f_2)}{f_2 - s} = \frac{f_1 f_2 - \frac{1}{2}(R + \delta)(f_1 + f_2)}{f_2 - \frac{1}{2}(R + \delta)} \ . \tag{3.67}$$

For a 10 cm lens ($f_1$), a curved mirror of $R = 10$ cm ($f_2 = -5$ cm) and $\delta = 1.5$ cm we obtain

$$a \approx 7.3 \text{ cm} \ . \tag{3.68}$$

Thus by placing the 10 cm lens a distance of 7.3 cm behind the cavity end mirror, we can focus the pump beam to its minimum spot size at the center of the crystal. In practice, this calculated distance is a "starting point" for the laser design and should be adjusted by trial and error to compensate for the term neglected in Eq. (3.66) and optimize the performance of the laser.

We saw from Section 3.3 that the spot size at the center of the crystal may be asymmetric. To effectively mode match the pump volume and the intracavity volume inside the crystal, we need to *introduce* astigmatism into the pump beam. This can be done by rotating the focusing lens about the vertical axis by a few degrees. In fact,

some astigmatism is already present due to the nonnormal approach of the pump beam on the curved cavity mirror. Calculations by Schulz [22] for a 14° angle of incidence at the curved cavity mirror show a required rotation of approximately 8°. Our experience showed that a similar rotation in the focusing lens resulted in increased output power.

In this section we have described the problem of matching the mode of the pump beam to that of the cavity. We saw that this can be accomplished by proper selection and placement of a focusing lens outside the cavity. We also briefly discussed how astigmatism may be introduced in the pump beam to better match the cavity mode volume. We now investigate various intracavity elements that can be used in the laser system.

## 3.5 Intracavity Elements

The specific application for a laser system dictates the type of intracavity elements required. In this section, we describe some intracavity elements that can be used inside a laser cavity to meet design requirements. These include unidirectional lasing and single wavelength operation. Our objective in this section is only to give a brief overview of certain intracavity elements. A more rigorous treatment of the theory of these elements can be found for example in [23].

Since some of these elements rely on the birefringent characteristics of certain materials, we begin this section with a basic review of birefringence.

### 3.5.1 Birefringence

Birefringence, or double refraction, is a property of anisotropic crystals where the index of refraction seen by incident light is a function of its polarization. Refractive indices are determined from the dielectric permeability of the medium. Here we only consider *uniaxial* crystals. In these crystals, two axes defined by the crystalline structure have the same dielectric permeability while the third axis has a different value. The axis with the unique dielectric permeability is referred to as the *optic axis* and represents a unique direction of propagation inside the crystal. The electromagnetic

waves representing the light incident on a birefringent medium are broken down into components based on the orientation of the **E** field vector relative to the optic axis. The components of the electromagnetic waves with the **E** field vector oriented along the optic axis experience one index of refraction $n_e$ and travel at the speed $c/n_e$. The trajectory of these waves represents the *extraordinary beam*. The components of the electromagnetic waves with the **E** field vector orthogonal to the optic axis experience a different index of refraction $n_o$ and travel at the speed $c/n_o$. The trajectory of these waves represent the *ordinary beam*.

The different speeds of the ordinary and extraordinary beams result in a phase difference between the two types of electromagnetic waves. This phase difference is represented by

$$\vartheta = \frac{2\pi}{\lambda} d\,(n_o - n_e)\ . \tag{3.69}$$

where $d$ represents the thickness of the birefringent medium. By varying this thickness one can control the phase difference induced by the birefringence. If the overall phase difference is $\vartheta = \pm\pi/2$, then the birefringent crystal changes linearly polarized light into circularly polarized light, provided the crystal is oriented so that the optic axis is at 45° to the plane of polarization of the incident beam. This optical element is known as a *quarter wave plate*. If the overall phase difference is $\vartheta = \pm\pi$, then the birefringent crystal rotates the plane of polarization by an angle of $2o$, where $o$ represents the angle between the plane of polarization and the optic axis of the crystal. Such optical elements are known as polarization rotators or *half wave plates*. The direction of rotation is determined by the direction of propagation through the birefringent crystal.

### 3.5.2 Unidirectional Lasing

A basic ring cavity, as shown in Fig. 3.1, allows for an electromagnetic wave to propagate in both directions. This means that as the gain medium is pumped and energy inside the gain medium builds up, the modes of each direction compete against each other. This competition can result in bistability or chaotic behavior. Many applications for ring lasers require the laser to be stable and therefore the direction

of lasing to be controlled. This is usually accomplished by giving the cavity a favored direction by suppressing or enhancing one of the directional modes.

One technique for introducing a favored direction inside the cavity is to reflect the output from one direction of the cavity back onto itself with an external mirror. This method has the effect of transferring a percentage of the energy from the undesired directional mode to the desired directional mode. One drawback of this technique is that pure unidirectional lasing cannot be obtained since energy buildup in the unfavored direction inside the cavity is not fully suppressed. Furthermore, this type of feedback may lead to phase and frequency instability.

To obtain unidirectional lasing, one must suppress the undesired directional cavity mode sufficiently to ensure that the threshold condition for that mode is not met. This suppression is often accomplished with an optical diode consisting of a Faraday rotator and some type of optical compensator. The manner by which these elements produce unidirectional lasing is as follows.

Laser systems usually contain surfaces oriented at Brewster's angle with respect to the cavity axis in order to minimize the insertion loss of intracavity elements. These Brewster windows give rise to a dominant polarization of the electromagnetic wave traveling inside the cavity. This dominant polarization is in the tangential plane, or the plane of incidence defined by the cavity axis and the normal to the surface of the Brewster window. This polarization component experiences no loss at the Brewster interface.

Certain materials rotate the plane of polarization of the electromagnetic wave as it passes through the medium. Birefringent crystals, alluded to in Section 3.5.1, are such materials. Other materials rotate the polarization of an electromagnetic wave when they are placed in a magnetic field. This effect is known as the *Faraday effect* and elements using this principle are referred to as Faraday rotators. The extent of rotation of polarization per unit length, or the "rotary power," of a Faraday rotator is proportional to the intensity of the magnetic field and an intrinsic property of the material represented by the Verdet constant. Unfortunately, materials with large Verdet constants usually also have high absorption coefficients. This means that large rotation angles can only be obtained at the expense of high transmission losses. The

direction of polarization rotation is determined solely by the direction of the magnetic field and is therefore independent of the direction of propagation. In other words, if the polarization of a wave changes by an angle $\phi$ after passing once through a Faraday rotator, it will have a total rotation of $2\phi$ if it is reflected back through the same Faraday rotator in the opposite direction.

To induce loss in one direction inside the cavity and not the other, a Faraday rotator is combined with a half wave plate. The half wave plate is oriented to compensate for the rotation induced by the rotator. In one direction, the half wave plate rotates the polarization back to its original orientation. For this direction, the wave suffers no loss as it travels through the Brewster windows inside the cavity. In the other direction however, the waveplate adds to the rotation of polarization and the electromagnetic wave is attenuated by traveling through a Brewster window. Even with small rotation angles, the attenuation of the wave is usually sufficient to fully suppress the undesired directional cavity mode.

### 3.5.3 Tuning to Single Wavelength

Lasers operating with broad gain medium require some type of wavelength selecting device if single wavelength operation is desired. To fully utilize broad tunability, we desire single wavelength operation with minimal loss to the desired wavelength. We also want to have a high transmission bandwidth at the selected wavelength and maximum rejection at the unwanted wavelengths. The optical element best suited for these requirements is the birefringent filter.

Since their introduction as a tuning element for broadband lasers, the theory and design of birefringent filters has been an area of active research [24, 25, 26, 27]. These filters have been used as tuning elements in a number of broadband lasers, including dye, high power Nd:glass, Ti:sapphire, and He–$Se^+$ [28, 29]. The basic theory behind birefringent filters is as follows.

As was shown in Section 3.5.1, birefringent crystals can be used to rotate the polarization of an incident electromagnetic wave. A birefringent plate which can be used as a wavelength selecting devise is shown in Fig. 3.7. The birefringent plate is placed into the laser cavity such that the normal of the plate is at Brewster's angle

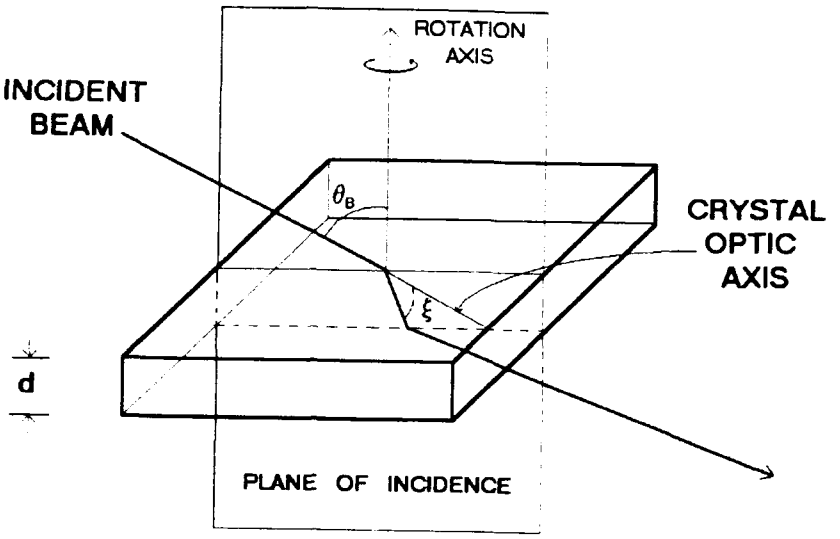


Figure 3.7: A birefringent plate used as an intracavity tuning element. The normal to the plate is at Brewster's angle $\theta_B$ to the cavity axis. The optic axis of the crystal makes the angle $\xi$ with the path of the refracted beam inside the crystal. The thickness of the plate is $d$.

$\theta_B$ to the cavity axis. The refracted beam inside the plate travels in a direction that makes the angle $\xi$ with the optic axis of the crystal. The phase difference induced between the ordinary beam and the extraordinary beam of wavelength $\lambda$ after it has travelled through the plate of thickness $d$ is given by

$$\vartheta = \frac{2\pi(n_e - n_o)dsin^2\xi}{\lambda sin\theta_B} . \tag{3.70}$$

Electromagnetic waves for which this phase difference is a multiple of $2\pi$ will experience no rotation in polarization and hence no attenuation as they pass through the end surface of the plate at Brewster's angle. The wavelength of these waves can be determined by setting $\vartheta = 2m\pi$ in Eq. (3.70) and solving for $\lambda$

$$\lambda = \frac{(n_e - n_o)dsin^2\xi}{msin\theta_B} . \tag{3.71}$$

where $m$ is an integer. Since the plate is introduced into the cavity at Brewster's angle, all other wavelengths will suffer loss as they exit the plate.

In practice, birefringent filters are composed of a series of birefringent plates. This is to provide stronger suppression of the undesired wavelengths and narrowing the transmission bandwidth of the filter. By rotating the filter around the normal

to the surface of the plate and hence keeping the plate at Brewster's angle to the cavity axis, one can change the angle $\xi$ between the optic axis of the crystal and the direction of the refracted beam inside the plate. From Eq. (3.71), we see that such a change in $\xi$ will result in a change in the "privileged" wavelength which is transmitted without loss. In this manner, one can tune the laser to a desired wavelength.

A more rigorous treatment of the theory and design of these filters can be found in the references cited at the beginning of this subsection. For a study of cavity modes containing birefringent filters see [30] and a detailed discussion of the stability of birefringent plates can be found in [31].

In this chapter, we have discussed the basic principles of designing a laser system. We discussed the advantages and disadvantages of standing wave and ring cavities. We presented an approach to the cavity design in terms of $ABCD$ ray transformation matrices and showed how they can be used to analyze the stability of laser cavities. We also developed a technique for compensating for astigmatism in the intracavity beam. We then discussed the mode matching problem and showed how to optimize the pump mode coupling into the cavity mode inside the gain medium. We also presented a brief survey of the intracavity elements that can be used for unidirectional lasing and tuning the laser to a single wavelength. With an understanding of the basics of laser design, we now turn our attention to the theory of laser dynamics.

# Chapter 4

# Laser Dynamics

An understanding of the behavior of any dynamical system requires a theoretical framework within which the system dynamics can be analyzed. Such a framework usually consists of a small number of equations of motion. These equations of motion are derived for an idealized system that mimics the physical system under investigation as much as possible. In this chapter, we present two basic equations of motion for a laser system known as the *laser rate equations*. We then show how these equations can be used to analyze relaxation oscillations exhibited by certain lasers. Many solid state lasers exhibit these oscillations. In particular, the Ti:sapphire laser described in this thesis exhibits pronounced relaxation oscillations when perturbed by external excitations from the steady state. We also describe a numerical method for modeling the dynamical behavior of the laser within the rate equation approximation. Finally, we look at the threshold condition for laser action and see how this condition can be used to determine the intrinsic cavity losses of a laser system.

## 4.1 Laser Rate Equations

The treatment of laser dynamics using rate equation theory involves the exchange of energy between two important dynamical variables, the number of photons inside the laser cavity $q$ and the number of excited atoms $n$ inside the laser gain medium. These two quantities evolve in time according to the *coupled cavity and atomic rate equations*. The derivation of these equations can be found in most textbooks on laser theory [16, 17, 32, 33]. The form of these equations depends somewhat on the model used to describe the gain medium. We opt for the four level laser model for the Ti:sapphire gain medium, as shown in Fig. (4.1). We assume that the upper pump

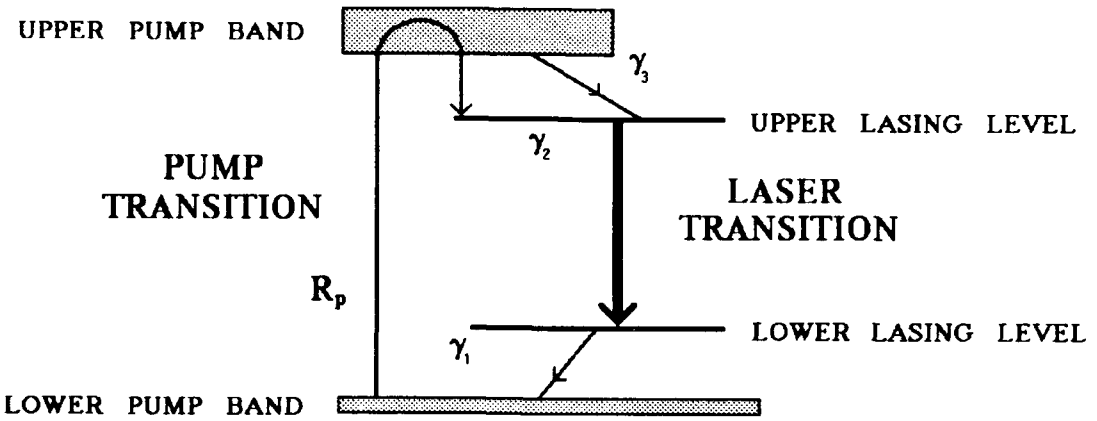


Figure 4.1: A general model of the four level laser pumping scheme. The decay rates from the upper pump band $\gamma_3$ and the lower lasing level $\gamma_1$ are assumed to be much greater than the decay rate of the upper lasing level $\gamma_2$. $R_p$ represents the rate at which atoms are introduced into the upper lasing level.

band and the lower lasing level decays instantaneously compared to the fluorescence lifetime. Assuming single mode laser operation, we arrive at the cavity rate equation, which describes the time evolution of the number of photons $q$ inside the laser cavity

$$\frac{dq(t)}{dt} = K n(t)\,[q(t) + 1] - \gamma_c q(t)\,. \tag{4.1}$$

Here $K$ is the spontaneous emission rate per mode and $\gamma_c$ is the cavity decay rate which is related to the round trip cavity loss $\ell_c$ (in percent per pass) and the cavity round trip time $T$ by

$$\gamma_c = \frac{\ell_c}{100T} = \tau_c^{-1}\,. \tag{4.2}$$

Eq. (4.2) introduces $\tau_c$ as the photon lifetime inside the cavity. The "1" inside the square brackets in Eq. (4.1) is sometimes referred to as the "extra photon" and represents the first photon inside the cavity mode due to the spontaneous emission process. Without this spontaneously emitted photon, the cavity photons would not "build up." Therefore, this "1" is required when Eq. (4.1) is used to describe the initial build up of laser action. At steady state, or other conditions where $q \gg 1$, this term can be ignored.

The atomic rate equation, which describes the number of atoms $n$ in the upper state is given by

$$\frac{dn(t)}{dt} = R_p - \gamma_2 n(t) - K n(t) q(t) , \tag{4.3}$$

where $R_p$ represents the rate at which atoms are introduce into the upper lasing level and $\gamma_2$ is the upper lasing level decay rate. The lifetime of the upper state, $\tau_2$, is related to its decay rate by

$$\gamma_2 = \tau_2^{-1} . \tag{4.4}$$

Since it is assumed that there is no accumulation of atoms in the lower lasing level, Eq. (4.3) also describes the evolution of laser inversion or the population inversion. The steady state solution of Eq. (4.1) and Eq. (4.3) gives us an expression for the number of atoms in the upper state

$$n_{ss} = \frac{\gamma_c}{K} , \tag{4.5}$$

and the number of photons inside the cavity

$$q_{ss} = \frac{R_p}{\gamma_c} - \frac{\gamma_2}{K} \equiv (r-1)\frac{\gamma_2}{K} . \tag{4.6}$$

Here we have introduced the laser *pump parameter* $r$ by

$$r = \frac{R_p K}{\gamma_2 \gamma_c} . \tag{4.7}$$

The laser pump parameter can also be written as the ratio of the pump power to the threshold pump power

$$r = \frac{W_p}{W_{th}} . \tag{4.8}$$

Note that at threshold, $r = 1$ and from Eq. (4.6) we can write

$$n_{th} = \frac{\gamma_c}{K} = \frac{R_p}{\gamma_2} . \tag{4.9}$$

Comparing Eq. (4.9) with (4.5), we see that in the steady state, laser inversion is "clamped" at its threshold value

$$n_{ss} = n_{th} . \tag{4.10}$$

We use these rate equations to look at one specific dynamical behavior known as relaxation oscillations exhibited by certain lasers.

## 4.2 Relaxation Oscillations: Laser Rate Equation Analysis

Many dynamic systems operating in the steady state will return to their steady state after being perturbed if the steady state is stable. The approach back to the steady state may not be monotonic. Instead, the system may approach the steady state in an oscillatory manner. These oscillations are usually damped and are known as *relaxation oscillations*. In this section, we analyze the rate equations of Section 4.1 in the presence of perturbations from steady state and see under what conditions a laser system exhibits relaxation oscillations. We will determine the equations of motion for the relaxation oscillations in terms of characteristic laser parameters.

Since the laser rate equations (4.1) and (4.3) are coupled, a perturbation in either the number of photons inside the cavity or the number of atoms in the upper state will result in a perturbation of the other. Treating the perturbations as small compared to the steady state values, we look for solutions to Eqs. (4.1) and (4.3) of the form:

$$q(t) = q_{ss} + \epsilon(t) \qquad \text{where} \quad \epsilon(t) \ll q_{ss} \,. \tag{4.11}$$

$$n(t) = n_{ss} + \eta(t) \qquad \text{where} \quad \eta(t) \ll n_{ss} \,. \tag{4.12}$$

Substituting Eqs. (4.11) and (4.12) into Eqs. (4.1) and (4.3) and keeping only terms linear in $\epsilon$ and $\eta$, we find the coupled rate equations for the perturbations to be

$$\frac{d\epsilon(t)}{dt} = (r-1)\gamma_2\eta(t) \tag{4.13}$$

$$\frac{d\eta(t)}{dt} = -\gamma_c\epsilon(t) - r\gamma_2\eta(t) \tag{4.14}$$

If we take the time derivative of Eq. (4.13) and use Eq. (4.14) for $\dot{\eta}$, we obtain a closed equation for $\epsilon(t)$.

$$\frac{d^2\epsilon(t)}{dt^2} = -r\gamma_2\frac{d\epsilon(t)}{dt} - (r-1)\gamma_2\gamma_c\epsilon(t) \,. \tag{4.15}$$

A similar equation is obtained for population perturbation. Equation (4.15) describes the perturbation in the cavity photon number. By introducing parameters $\beta$ and $\omega_o$ as

$$2\beta = r\gamma_2 \qquad \text{and} \qquad \omega_o^2 = (r-1)\gamma_2\gamma_c \,. \tag{4.16}$$

we can rewrite the equation of motion for the perturbation of cavity photon number as

$$\frac{d^2\epsilon(t)}{dt^2} + 2\beta\frac{d\epsilon(t)}{dt} + \omega_o^2\epsilon(t) = 0 \,. \tag{4.17}$$

This is the equation of motion for a damped harmonic oscillator with natural frequency $\omega_o$ and energy decay constant $2\beta$. The solution of this equation is of the form

$$\epsilon(t) = \epsilon_o e^{-i\omega t} \,. \tag{4.18}$$

Substituting Eq. (4.18) into Eq. (4.17) we get the auxiliary equation

$$\omega^2 + i2\beta\omega - \omega_o^2 = 0 \,. \tag{4.19}$$

which determines $\omega$. Solving this equation for $\omega$ we find

$$\omega = -i\beta \pm \sqrt{\omega_o^2 - \beta^2} = -i\beta \pm \omega_r \,, \tag{4.20}$$

where we have introduced a shifted frequency $\omega_r$ by

$$\omega_r = \sqrt{\omega_o^2 - \beta^2} \,. \tag{4.21}$$

As is well known, dissipation shifts the frequency of oscillation [34].

The behavior of $\epsilon(t)$ depends on the relative magnitude of $\omega_o$ and $\beta$. We consider three cases separately.

a.) For the case $\omega_o^2 < \beta^2$, $\omega$ is pure imaginary and the solution from Eq. (4.18) takes the form

$$\epsilon(t) = Ae^{-(\beta+\omega_r)t} + Be^{-(\beta-\omega_r)t} \,. \tag{4.22}$$

Thus any perturbation from the steady state exponentially decays to zero. The system is said to be *overdamped.* In this case no oscillations in the laser photon number will be observed. The condition $\omega_o^2 < \beta^2$ can also be expressed in terms of decay rates of the laser system. By recalling the definitions of $\beta$ and $\omega_o$ from Eq. (4.16), we find that the condition for an overdamped response is

$$(r-1)\gamma_c < \frac{r^2\gamma_2}{4} \,. \tag{4.23}$$

This implies that the cavity decay rate must be less than or of the same order of magnitude as the upper state atomic decay rate. This is characteristic of most gas lasers, where relaxation oscillations are not observed.

b.) When $\omega_o^2 = \beta^2$, the two roots to Eq. (4.19) are equal. For this case, the solution from Eq. (4.18) takes the form

$$\epsilon(t) = \epsilon^{-\beta t}(At + B) \ . \tag{4.24}$$

and the system is said to be *critically damped.* Any perturbation in the system decays to zero asymptotically with time. This condition exits in a laser system when

$$(r-1)\gamma_c = \frac{r^2\gamma_2}{4} \ . \tag{4.25}$$

or the cavity decay rate and upper state decay rate are of the same order of magnitude.

c.) For the case $\omega_o^2 > \beta^2$, $\omega_r$ is real. Using Eq. (4.20), the solution from Eq. (4.18) takes the form

$$\epsilon(t) = \epsilon^{-\beta t}\left(A\epsilon^{i\omega_r t} + B\epsilon^{-i\omega_r t}\right) \ . \tag{4.26}$$

This solution can also be rewritten in the form

$$\epsilon(t) = \epsilon_o\epsilon^{-\beta t}cos(\omega_r t + \phi) \ . \tag{4.27}$$

In this case, the system is said to be *underdamped* and displays an exponentially damped sinusoidal response to the perturbation as it returns to steady state. In terms of decay rates, we expect to see these relaxation oscillations in a laser system where

$$\gamma_c > \gamma_2 \ . \tag{4.28}$$

This is the case for many solid state lasers. Expressed in terms of laser parameters from Eq. (4.16) the oscillations around the steady state have a frequency given by

$$\omega_r = \sqrt{(r-1)\gamma_2\gamma_c - r^2\gamma_2^2/4} \ . \tag{4.29}$$

The perturbation has an exponentially decaying envelop characterized by a decay rate given by

$$\beta = \frac{r\gamma_2}{2} \ . \tag{4.30}$$

From Eqs. (4.29) and (4.30) we see that one can determine certain laser parameters by analyzing the relaxation oscillations. Indeed, this was one of the objectives of the experiments discussed in Chapter 5.

Once we understand the characteristic equations of motion for a dynamic system and their controlling parameters, we can now address the question of whether these equations adequately describe the system dynamics in general. This is the subject of the next section.

## 4.3 Relaxation Oscillations: Numerical Modeling

One of the best ways to study a dynamic system is to model it and compare the observed response with that predicted by the model. In this section, we describe a method for modeling the relaxation oscillations exhibited by a laser.

Although the coupled laser rate equations of Section 4.1 are fairly simple in form, exact analytical solutions to them are limited and complex in form [35]. Therefore, in order to effectively model any type of laser dynamic these rate equations must be solved numerically. The number of photons $q$ and the number of excited atoms $n$ are very large for realistic systems. These large numbers are difficult to manage numerically. We therefore introduce scaled variables that are better suited for numerical modeling. The scaling should be chosen in such a way as to minimize the number of parameters in the equations of motion. Also, the scaling should allow the equations to be solved with parameters measured from the experiment. We present two different procedures for scaling. These are suitable for modeling different types of perturbations.

For the system when gain is perturbed we scale the cavity photon number and the number of excited atoms by introducing the variables

$$x = \frac{q}{q_s} = \frac{Kq}{\gamma_2} \tag{4.31}$$

$$y = \frac{n}{n_{th}} = \frac{Kn}{\gamma_c}. \tag{4.32}$$

Here $q_s$ represents the *saturation photon number* for the active atoms. It is defined as the ratio of population decay rate $\gamma_2$ and the spontaneous emission decay rate per

mode $K$ by

$$q_s = \frac{\gamma_2}{K} . \tag{4.33}$$

The scale factor for population $n_{th}$ is the *threshold population inversion* defined by Eq. (4.9). Equations (4.31) and (4.32) imply that $x$ is the cavity photon number in units of saturation photon number and $y$ is the population inversion in units of threshold inversion. Using Eq. (4.7) we can express the population pumping rate in terms of laser pump parameter $r$ and various decay rates as

$$R_p = \frac{r\gamma_2\gamma_c}{K} . \tag{4.34}$$

Substituting the scaled variables from Eqs. (4.31), (4.32) and (4.34) into Eqs. (4.1) and (4.3), the rate equations for the scaled variables are found to be

$$\frac{dx}{dt} = \gamma_c \left[ y\left(x + \frac{1}{q_s}\right) - x \right] . \tag{4.35}$$

$$\frac{dy}{dt} = \gamma_2 \left(r - y - yx\right) . \tag{4.36}$$

Finally, scaling time in terms of the cavity lifetime $\tau_c$ by

$$\tau = \gamma_c t = \frac{t}{\tau_c} , \tag{4.37}$$

we can rewrite Eqs. (4.35) and (4.36) as

$$\frac{dx}{d\tau} = (y-1)x + \frac{y}{q_s} \tag{4.38}$$

$$\frac{dy}{d\tau} = s(r - y - xy) . \tag{4.39}$$

Here $s$ is the ratio of the population decay rate $\gamma_2$ and the cavity decay rate $\gamma_c$

$$s = \frac{\gamma_2}{\gamma_c} . \tag{4.40}$$

These equations are appropriate for modeling a system where the gain of the laser is modulated. Modulation of gain can be described in terms of the pump parameter alone.

For systems where loss is modulated, both $\gamma_c$ and $r$ are changing, so a different scaling is more appropriate. For dynamical studies with this type of system, we replace $y$ defined in Eq. (4.32) with the variable

$$z = \frac{Kn}{\gamma_2} . \tag{4.41}$$

In this model we scale both the number of atoms in the upper state and the number of photons in the cavity by the saturation photon number defined by Eq. (4.33). We scale the time in terms of the upper state lifetime by

$$\tau = \gamma_2 t = \frac{t}{\tau_2} . \tag{4.42}$$

Using Eqs. (4.31), (4.41) and (4.42) into Eqs. (4.1) and (4.3) we obtain the new rate equations

$$\frac{dx}{d\tau} = z\left(x + \frac{1}{q_s}\right) - px \tag{4.43}$$

$$\frac{dz}{d\tau} = R - z(x+1) . \tag{4.44}$$

where we have introduced a new parameter $p$ by

$$p = \frac{\gamma_c}{\gamma_2} . \tag{4.45}$$

The normalized pumping rate

$$R = \frac{R_p K}{\gamma_2^2} = rp \tag{4.46}$$

then depends only on the pumping rate $R_p$ and stays constant as long as $R_p$ is constant. The only parameter that changes when the cavity loss is modulated is $p$, defined in Eq. (4.45). It is helpful to solve Eqs. (4.43) and (4.44) for the steady state. For the scaled cavity photon number at steady state we find

$$x_{ss} = \frac{R}{p} - 1 = r - 1 . \tag{4.47}$$

For the scaled population inversion we find (neglecting the $1/q_s$ term)

$$z_{ss} = p . \tag{4.48}$$

We will find these steady state values useful in Section 5.2.4 when we use Eqs. (4.43) and (4.44) to model our experimental observations.

Using Eqs. (4.38) and (4.39), or Eqs. (4.43) and (4.44), one could model a system numerically depending on whether the gain or the loss is modulated. These equations are scaled in such a manner that only a single parameter is needed to describe the modulation of the system. For Eqs. (4.38) and (4.39), $r$ is varied to represent gain modulation. For Eqs. (4.43) and (4.44), $p$ is varied to represent loss modulation. From their definitions in Eqs. (4.8) and (4.45), these parameters can be measured experimentally.

## 4.4 A Method for Determining Intrinsic Cavity Loss

The threshold for a laser system is defined to be the operating point at which the round trip gain is equal to round trip loss. In other words, the rate at which the signal grows inside the cavity is balanced by its decay rate out of the cavity. In this section we derive an equation that represents the threshold condition and describe an experimental method to determine the intrinsic losses of a laser system.

Let $\alpha$ represent the gain coefficient (fractional gain per watt per second) of the laser and $W_{th}$ be the pumping power at threshold. Then the threshold condition can be written as

$$\gamma_c = \alpha W_{th} \,. \tag{4.49}$$

where the cavity decay rate $\gamma_c$ is defined in Eq. (4.2). If we let the total cavity decay rate $\gamma_c$ be represented by the sum of the decay rate due to intrinsic losses of the laser $\gamma_{int}$ and an induced decay rate $\gamma_{AOM}$ due to a variable loss element such as an acousto-optic modulator (AOM), then we can write

$$\gamma_c = \gamma_{int} + \gamma_{AOM} \,. \tag{4.50}$$

The threshold condition then becomes

$$\gamma_{int} + \gamma_{AOM} = \alpha W_{th} \,. \tag{4.51}$$

If the losses are small, we can express Eq. (4.51) in terms of percent loss. Using Eq. (4.2) we write

$$\ell_c = \ell_{int} + \ell_{AOM} = gW_{th} \,. \tag{4.52}$$

Here $g$ represents the gain of the laser in *percent gain per pass per watt* of pumping power. In terms of the fractional gain coefficient $\alpha$ and the cavity round trip time $T$ we express $g$ as

$$g = 100T\alpha \,. \tag{4.53}$$

Since the intrinsic cavity loss $\ell_{int}$ is a constant of the laser, we rewrite Eq. (4.52) with $\ell_{AOM}$ as a dependent variable

$$\ell_{AOM} = gWth - \ell_{int} \,. \tag{4.54}$$

This is an equation representing a straight line of slope $g$ and intercept $-\ell_{int}$. From Eq. (4.54), one can determine the intrinsic cavity loss by measuring the threshold pump power $W_{th}$ required at different levels of induced loss $\ell_{AOM}$. Indeed this was the objective of the second set of experiments described in Chapter 5.

From this same experimenta method, we can also determine other parameters of our laser system. Recalling the definitions of the laser pump parameter $r$ in Eq. (4.8) and the normalized pumping rate $R$ in Eq. (4.46), we can write

$$R = \frac{gW_p}{100\gamma_2 T} \,. \tag{4.55}$$

where we have also used Eqs. (4.49) and (4.53). Therefore, once we know $g$ from the slope of Eq. (4.54), we can determine the normalized pumping rate $R$, which is another constant of the system, for a given pump power $W_p$. We apply this method to determine $R$ for our laser system in Chapter 5.

Finally, we can approximate the stimulated emission cross section $\sigma_{21}$ of the laser gain medium. Near threshold, the gain coefficient is known as the *small signal* gain coefficient. In terms of percent gain per watt per pass, the small signal gain coefficient $g$ can be written

$$g = \frac{100\eta_0\eta_1\eta_2\eta_3\sigma_{21}\tau_2}{Ah\nu_p} \,. \tag{4.56}$$

The $\eta$ terms represent efficiencies of transferring energy from the pump laser to the laser transition. The quantum efficiency $\eta_0$ represents the fraction of absorbed photons into the pump band that actually participate in the laser transition. The energy efficiency term $\eta_1$ represents the ratio of the energy of a laser photon to that of a pump photon

$$\eta_1 = \frac{h\nu_l}{h\nu_p} = \frac{\lambda_p}{\lambda_l} . \tag{4.57}$$

Here the subscript $p$ refers to the pump and $l$ refers to the laser. The fraction of the actual pump beam that is incident on the laser gain medium is represented by $\eta_2$, which accounts for reflection losses, scattering, etc. The fraction of the incident light actually absorbed by the gain medium is given by $\eta_3$. The upper state lifetime $\tau_2$ is defined in Eq. (4.4) and $A$ is the cross sectional area of the pump beam passing through the gain medium. Finally, $h\nu_p$ represents the energy of a pump photon. Solving Eq. (4.56) for $\sigma_{21}$ we find

$$\sigma_{21} = \frac{gAh\nu_p}{100\eta_0\eta_1\eta_2\eta_3\tau_2} . \tag{4.58}$$

All terms except $\eta_0$ in Eq. (4.58) can be determined experimentally, with a little extra work, from the method for determining cavity losses outlined in this section. We will use Eq. (4.58) in Chapter 5 to approximate the stimulated emission cross section $\sigma_{21}$ for our Ti:sapphire crystal.

In this chapter we saw how Eqs. (4.1) and (4.3) can be used to analyze the relaxation oscillations of lasers. We also developed a method for modeling this dynamical behavior in lasers. We concluded the chapter with a brief look at the threshold condition and saw how the intrinsic cavity loss, the normalized pumping rate, and the stimulated emission cross section can be determined with experimental measurements at threshold. In the next chapter, we describe the experiments conducted with our Ti:sapphire laser.

# Chapter 5

# Experimental Results

In the Ti:sapphire laser, population inversion evolves on a time scale comparable to the cavity lifetime. Such lasers are known as class-B lasers. Most solid state lasers fall into this category. When perturbed, this class of lasers exhibits a wide variety of dynamical behavior. These include simple relaxation oscillations, spiking oscillations, and chaotic behavior. The type of dynamical behavior observed depends on the frequency and depth of perturbations from the steady state.

This chapter begins with a description of the laser system used to conduct the experiments. We then describe the data acquisition procedure, results, and analysis of two sets of experiments. The first set involved the measurement of the relaxation oscillations and spiking behavior exhibited by the Ti:sapphire laser. The second set involves experiments that allow us to determine the intrinsic loss of the cavity by an independent method. From the analysis of these experiments, we were able to derive useful information such as the upper lasing level decay rate, cavity losses and gain per pass for our laser system. Although the results presented here are specific to the Ti:sapphire laser we designed and constructed, similar procedures and conclusions could be applied to other laser systems as well. Information from these experiments would be useful in other experiments on the dynamics of class-B lasers.

## 5.1 Laser Description

The laser system used for the experiments described in this chapter was designed according to the methods developed in Chapter 3. A diagram of the laser is shown in Fig. 5.1. The laser cavity consists of two curved mirrors, each with radius of curvature $R = 10$ cm and two flat mirrors for steering the long arm. All four mirrors

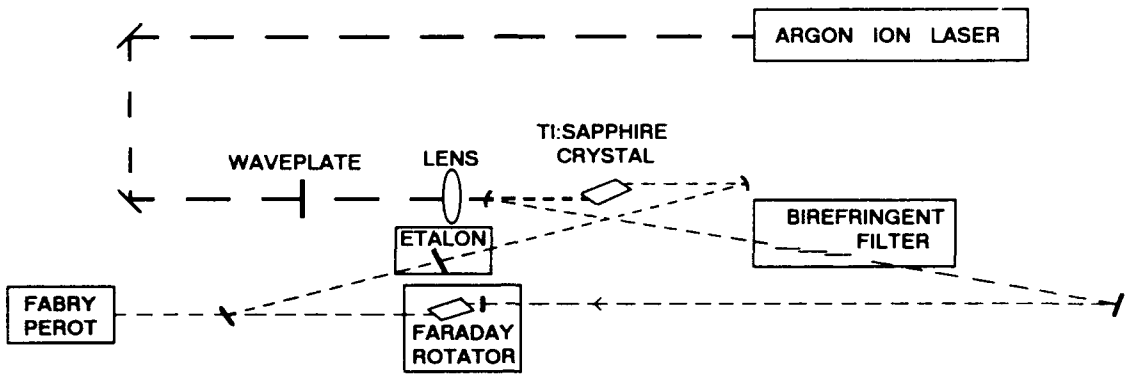


Figure 5.1: Laser cavity design used for the experiments in Chapter 5.

were coated for high reflectivity in the wavelength range 650 to 900 nm and high transmittivity (>85%) for the argon ion pumping lines of 488 and 514.5 nm. The coating was optimized for incident angles of 20° for *p*-polarization. The mirror mounts were constructed of anodized aluminum and had three contact points for adjustment. This mount design afforded precise translational and sensitive tilt adjustments with 80-pitch adjusting screws. The mirror mounts were secured to a 2-inch stainless steel optical breadboard mounted on a four pedestal floating optics table.

The 2 cm long Ti:sapphire rod was cut with Brewster windows at both ends and had a diameter of 4 mm. The rod was housed in a water-cooled copper jacket mounted on a tilt/rotation stage. This stage allowed for rotational adjustment about all axes of the crystal. The crystal was wrapped with thin flexible copper foil to ensure good thermal contact with the cooling jacket.

The dimensions of the cavity were determined by using the stability requirements discussed in Section 3.2. The size of the laser was to be large enough to accommodate various intracavity elements and still fit the confines of the $1' \times 2'$ breadboard. The actual length of the long arm was approximately 107 cm and the value selected from the stability diagrams for $\delta$ was about 1.5 cm (see Figs. 3.2 and 3.3). This gave a total distance of 11.5 cm between the two curved mirrors along the cavity axis and 4.75 cm between the faces of the crystal and the curved mirrors. The physical round trip length of the cavity was 118 cm. The angle of incidence at the curved mirrors was 15.5°, selected to give maximum astigmatic compensation in the long arm of the laser, as detailed in Section 3.3.

The pump beam was mode matched to the fundamental cavity mode with a 10 cm achromatic lens positioned 7.9 cm behind one of the curved cavity mirrors, as described in Section 3.4. The theoretical position of 7.3 cm from Eq. (3.68) was initially used, then the lens was translated to optimize output. The mount for the lens afforded two dimensions of translational freedom as well as tilt around the vertical and lateral axes. The polarization of the pump beam was rotated with a half wave plate (polarization rotator) anti-reflection coated for the pump wavelengths. The vertical polarization was rotated 90° into the tangential plane for minimal loss at the Brewster window of the crystal.

A Brewster's angle Faraday rotator and compensating waveplate were placed in the long arm of the cavity to obtain unidirectional lasing. The combination was placed inside the cavity to permit clockwise propagation of the laser beam in the long arm, as shown in Fig. 5.1. A three-plate birefringent filter, inserted at Brewster's angle was used to obtain single wavelength performance. Single mode operation was obtained by introducing a 3 mm thick etalon into the cavity. The etalon has about 30 % reflectivity centered at 780 nm for normal incidence. The entire laser system was enclosed in a plexiglass dust cover to improve stability. The pump beam was steered through a plexiglass tube to minimize fluctuations due to air currents and dust particles over the 2 meters of propagation to the Ti:sapphire laser. The laser operated stably in a single longitudinal mode. This was checked with the help of a scanning spectrum analyzer. Experiments were conducted with this laser as described in the following sections of this chapter.

## 5.2 Experiment 1: Relaxation Oscillations

There were two objectives in the first set of experiments. The first objective was to determine the fluorescence lifetime, $\tau_2$, of the upper lasing level and the intrinsic cavity losses, $\ell_c$ (percent loss per round trip), of our Ti:sapphire laser. Both of these quantities were determined by analyzing the results of the experiments in terms of the linearized rate equation model introduced in Chapter 4.

The second objective was to see how well the full rate equations predicted the

observed behavior of the laser. The theoretical model assumed a four level laser and ignored all sources of noise, fundamental as well as deterministic. It assumed that polarization dynamics are fast compared to the population and field dynamics and that the lower level decays almost instantaneously to the lower pumping level.

The experimental method involved switching the cavity Q, or modulating the laser cavity loss. The output waveforms from the laser were digitized and recorded as a function of time. A series of measurements were made of the relaxation oscillations at different pump parameters. From this series, one particular waveform was selected at random to extract characteristic laser parameters. Once known, these parameters were used to predict the relaxation oscillation behavior of the laser at other pump parameters.

### 5.2.1 Experimental Procedure

In order to perturb the laser, an acousto-optic modulator (AOM) was placed in the long arm of the laser, as shown in Fig. 5.2. The AOM was manufactured by IntraAction Corporation. It consists of a quartz crystal, anti-reflection coated for minimal static insertion loss in the 700 to 900 nm wavelength range, sandwiched between two piezoelectric transducers. The transducers set up acoustic waves in the crystal causing spatially periodic changes in the index of refraction. These periodic changes give rise to a refractive index grating in the path of the beam. This grating causes a certain fraction of the beam to be diffracted out of the beam path and acts as a source of intracavity loss. The loss suffered by the beam passing through the AOM depends on the angle of incidence of the beam and the amplitude of the acoustic wave. An 80 MHz acoustic wave was set up by the driver (IntraAction Corporation Model ME-80B). The driver produces an 80 MHz signal whose amplitude is proportional to the input voltage in the range 0 to 1 volt. The depth and frequency of modulation (duration of acoustic power on) was controlled by pulses from a Krohn-Hite Model 2000 signal generator to the driver.

After the AOM was put inside the cavity, all elements were adjusted to minimize the threshold of laser action. Laser threshold was found to be at 4.75 watts from the argon ion pump laser when no signal was applied to the AOM. The cavity was then

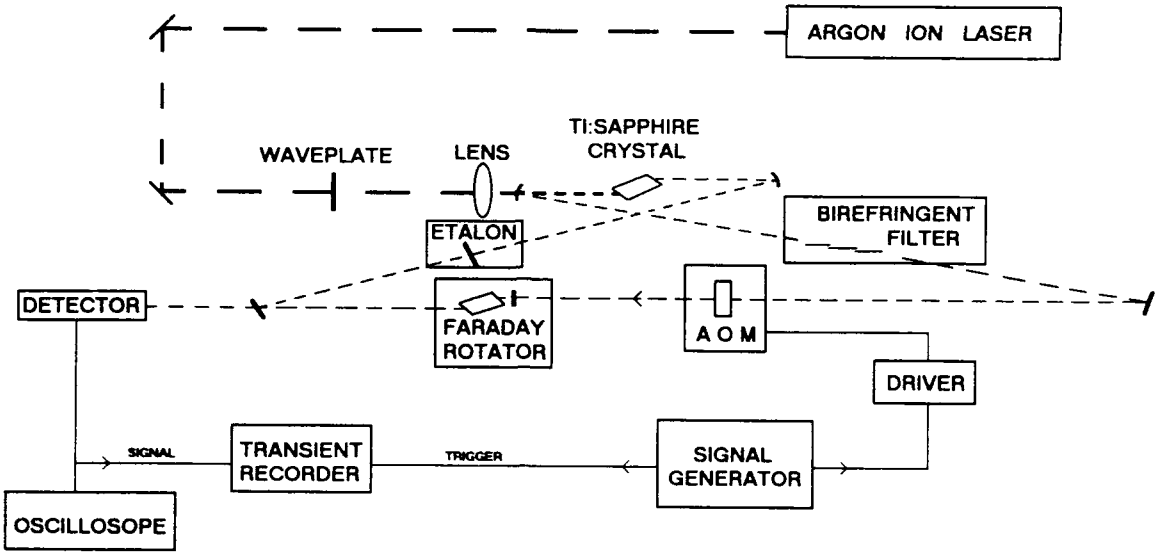


Figure 5.2: Experimental setup to conduct relaxation oscillation experiments described in Section 5.2. The laser beam is represented by the light dashed line and the pump beam by the heavy dashed line. The solid line represents electrical connections.

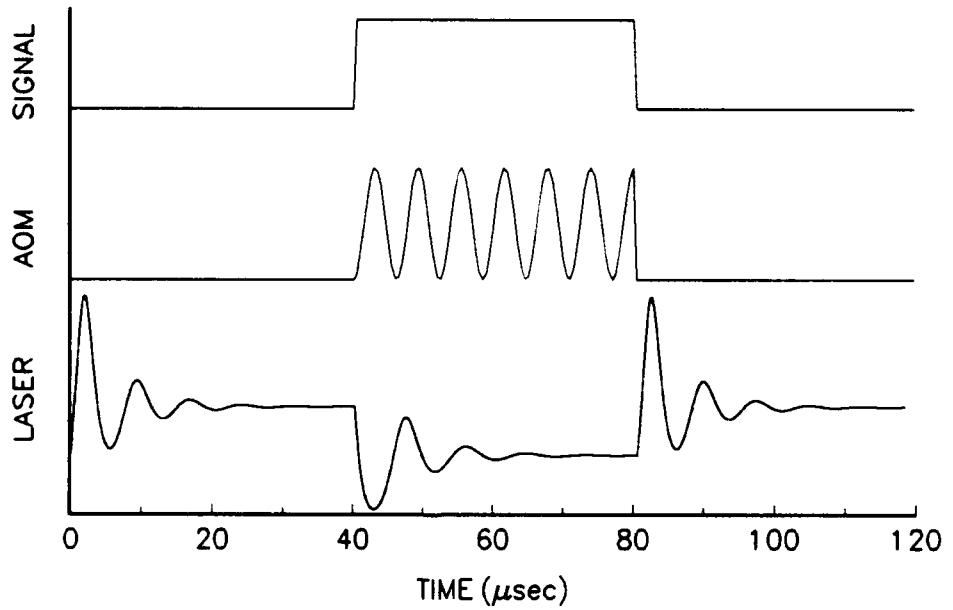


Figure 5.3: A timing diagram comparing the outputs of the signal generator, the AOM driver, and the laser for shallow cavity loss modulation. The cavity experienced greater loss during the time period that the acoustic wave was on.

loss modulated. Both the frequency and depth of loss modulation could be controlled. Cavity losses are related to cavity $Q$ by

$$Q = \frac{2\pi L}{\lambda \ell_c}. \tag{5.1}$$

where $L$ is the round trip length, $\lambda$ is the lasing wavelength, and $\ell_c$ is the percent power loss per round trip. It follows that since the AOM modulates the internal loss, it modulates the cavity $Q$.

Output from the laser was detected by a variable gain, high bandwidth, fast photodetector using the light output from one of the flat cavity mirrors. To keep the threshold pump power as low as possible, no output coupler was used. This setup also allowed us to determine just the intrinsic cavity loss, without having to compensate of output losses. The signal from the photodetector was monitored with a Tektronics 2465A 350 MHz oscilloscope and digitized with a LeCroy TR8837F transient recorder. The transient digitizer was housed in a CAMAC crate controlled by a LeCroy 8901A GPIB crate controller. Both the transient digitizer and the AOM driver were triggered from the same source. At the end of each measurement, the recorded waveforms were transferred to an IBM PC/AT for further analysis. A full schematic of the experiment is shown in Fig. 5.2. A timing diagram comparing the output of the signal generator, the AOM driver, and the laser as a function of time is shown in Fig. 5.3. Data were taken and evaluated for two independent experiments to determine the parameters that govern the rate equations of Section 4.1.

### 5.2.2 Results

For the transient dynamics experiments, the cavity $Q$ was modulated at two different depths. Deep modulation resulted in the laser being completely off during the period of modulation. This means that the cavity loss and AOM induced loss exceeded round trip gain. Shallow modulation resulted in the laser operating continuously, but jumping between different "cavities," one with a high Q and the other with a lower Q. For the sake of distinguishing the response of the laser to the loss modulation in these two cases, we refer to the transient oscillations in the case of deep modulation

as *spiking oscillations* and those in the case of shallow modulation as *relaxation oscillations*. The output waveforms were recorded for different pump parameters. At each operating point, we recorded waveforms from a single sweep and from an average of ten sweeps.

One particular waveform averaged over ten sweeps, chosen at random, was analyzed to determine all the characteristic parameters describing the relaxation oscillation equations of Section 4.2. The procedure for determining $\tau_2$ and the corresponding uncertainty is as follows. From Eq. (4.27), we see that the envelop of transient oscillation is a pure exponential with a decay rate $\beta$. This exponential decay rate is related to the upper state decay rate $\gamma_2$ via Eq. (4.30). Therefore, knowing the pump parameter $r$ and measuring $\beta$ allows us to determine $\gamma_2$. The upper state lifetime is related to the upper state decay rate by the expression

$$\tau_2 = \gamma_2^{-1} . \tag{5.2}$$

To measure $\beta$, we let $\mu(t)$ represent the peak amplitudes of the oscillations from the steady state. These peaks form an exponentially decaying curve according to the expression

$$\mu(t) = \mu_o e^{-\beta t} . \tag{5.3}$$

Here $\mu_o$ represents the amplitude of the initial perturbation and $\beta$ is the decay rate. The positions of the peaks of the oscillation versus elapsed time were fit to an exponential decay curve to determine $\beta$ in Eq. (5.3). This measured value of $\beta$ was then used along with the pump parameter of the waveform being analyzed to determine the upper state decay rate according to Eq. (4.30). We then determine $\tau_2$ using Eq. (5.2).

The uncertainty in $\tau_2$ was estimated from the uncertainty in $\beta$. Since the peaks of the recorded waveform correspond to a specific number of counts, $N$, we assume a Poissonian distribution for the counts and take the statistical uncertainty in the peaks to be

$$\sigma_\mu \approx \frac{N}{\sqrt{N}} = \sqrt{N} . \tag{5.4}$$

The steady state value of the waveform was determined by taking the time average of the last one half of the waveform, where the laser had reached steady state. The

uncertainty in the steady state value was also estimated. The statistical uncertainty in time separation between successive peaks was simply the root mean squared of the deviations of the time period between peaks. If we take the natural logarithm of Eq. (5.3), we can express $\beta$ in terms of the amplitudes of the peaks and the time periods, $T$,

$$\beta = \frac{\ln \mu_o - \ln \mu}{T} . \tag{5.5}$$

Using the laws of error propagation [36], we can approximate the uncertainty, $\Delta\beta$, in $\beta$ to be

$$\Delta\beta \approx \sqrt{\left(\frac{\Delta\mu}{\mu T}\right)^2 + \left(\frac{\Delta\mu_o}{\mu_o T}\right)^2 + \left(\frac{\Delta T}{T}\right)^2} . \tag{5.6}$$

Here $\Delta\mu$ represents the averaged uncertainty of the peaks of the waveform, $\Delta\mu_o$ represents the uncertainty in the steady state value of the waveform, and $\Delta T$ represents the uncertainty in the time separation between peaks.

Using $r = 1.39$ for the pump parameter of the waveform being analyzed and the measured value of $\beta$ in

$$\gamma_2 = \frac{2\beta}{r} , \tag{5.7}$$

we find the value for the upper state decay rate to be

$$\gamma_2 = 288 \pm 10 \text{ KHz} . \tag{5.8}$$

The upper state lifetime $\tau_2$ is then given by

$$\boxed{\tau_2 = 3.47 \pm .13 \mu\text{sec}} . \tag{5.9}$$

To find $\ell_c$, the intrinsic cavity loss, we first determine the relaxation oscillation frequency $\omega_r$, from the measured waveform using the average time period between successive peaks $T_{ave}$

$$\omega_r = \frac{2\pi}{T_{ave}} . \tag{5.10}$$

From the measured value of $\omega_r$, we are able to determine the cavity loss rate, $\gamma_c$, by using Eq. (4.16) into (4.29) to obtain

$$\gamma_c = \frac{\omega_o^2}{\gamma_2(r-1)} = \frac{\omega_r^2 + \beta^2}{\gamma_2(r-1)} . \tag{5.11}$$

The uncertainty in the oscillation frequency was determined from the uncertainty in the time periods according to

$$\frac{\Delta\omega_r}{\omega_r} \approx \frac{\Delta T}{T_{ave}} . \tag{5.12}$$

The uncertainty in $\gamma_c$ is determined from the relation

$$\frac{\Delta\gamma_c}{\gamma_c} \approx \sqrt{4\left(\frac{\Delta\omega_o}{\omega_o}\right)^2 + \left(\frac{\Delta\gamma_2}{\gamma_2}\right)^2} . \tag{5.13}$$

where

$$\frac{\Delta\gamma_2}{\gamma_2} \approx \frac{\Delta\beta}{\beta} . \tag{5.14}$$

Using the measured values for $\beta$, $\omega_r$, $\gamma_2$ and $r$ in Eq. (5.11), $\gamma_c$ is found to be

$$\gamma_c = 9.18 \pm .05 \text{ MHz} . \tag{5.15}$$

Using Eq. (5.15) into Eq. (4.2) we obtain a cavity loss of

$$\boxed{\ell_c = (3.6 \pm .2)\ \% \text{ per pass}} \tag{5.16}$$

for our 118 cm cavity. This figure includes the static insertion loss of the AOM which, according to the specifications, carries a loss of about 0.25 %.

Once the values for the upper state decay rate $\gamma_2$ and the cavity decay rate $\gamma_c$ are determined, a relaxation oscillation frequency can be predicted for all pump parameters and compared with the relaxation oscillation frequency measured experimentally from the recorded waveforms. Figure 5.4 shows the results of such a comparison for deep modulation. All experimental data for $\omega_r$ were extracted from single sweep records. Figure 5.6 shows the same comparison except that the experimental data were extracted from waveforms averaged over ten sweeps. Error bars for the single sweep results represent the root mean squared deviations in the period of oscillation. The error bars for the ten sweep results represent the largest variation between the single sweep measurement and the ten sweep measurement for a given pump parameter. For completeness, a plot of the output power of the laser, measured by the same detector used for detecting the waveform signal, as a function of pump parameter is shown in Fig. 5.5. Figures 5.7-5.9 show the same comparison as Figs. 5.4-5.6 for shallow modulation of the cavity.

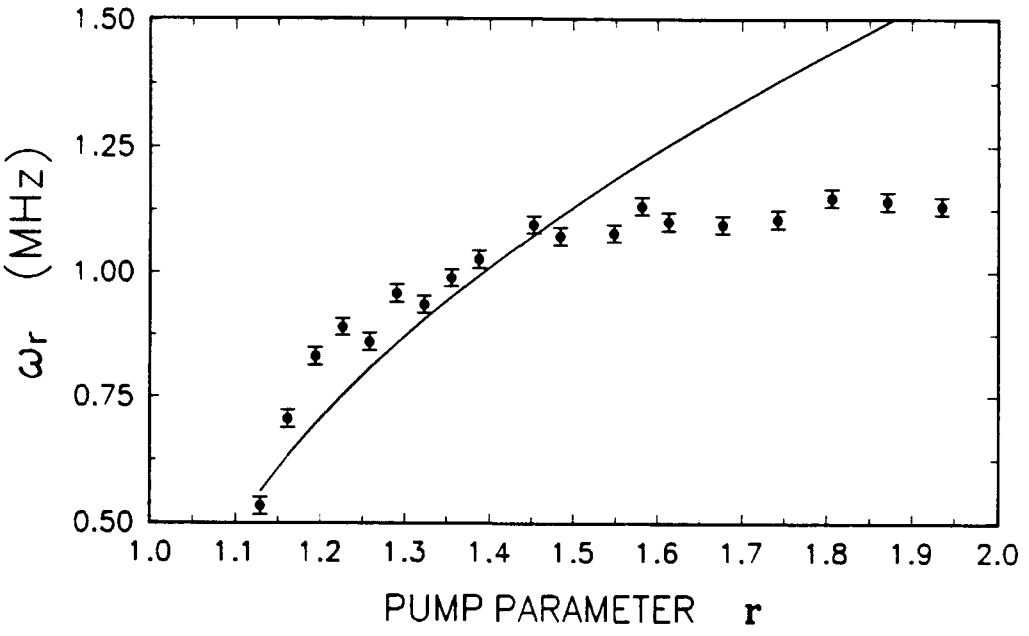


Figure 5.4: Variation of oscillation frequency $\omega_r$ with pump parameter $r$. Experimental points are from single sweep waveforms recorded with deep cavity loss modulation. The continuous line represents the theoretical curve from Eq. (4.29). Parameters $\gamma_3$ and $\gamma_2$ were extracted from a single waveform averaged over ten sweeps at the pump parameter $r = 1.39$.

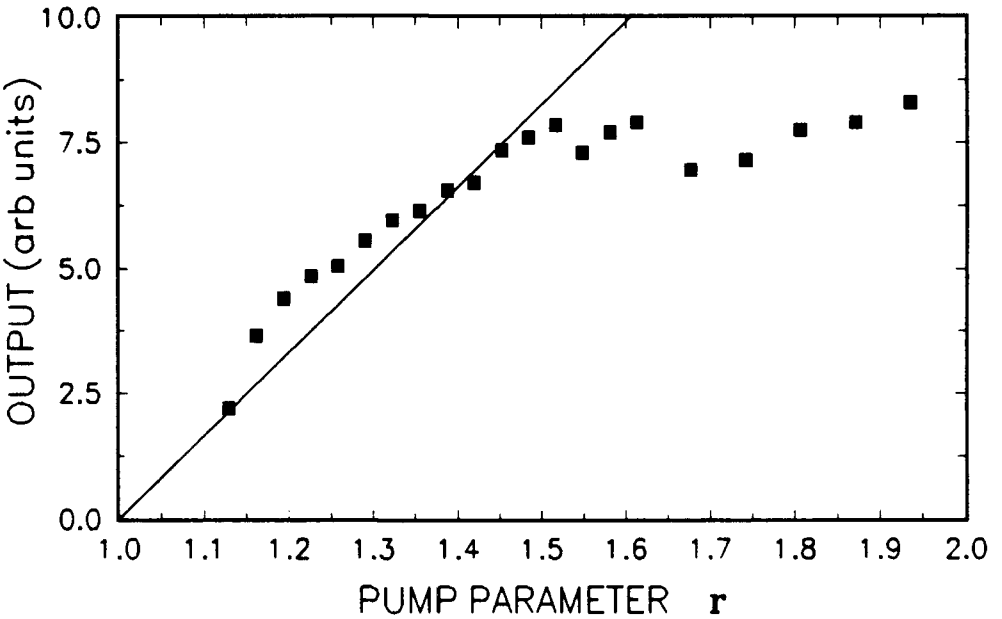


Figure 5.5: Variation of laser output power versus pump parameter $r$ for deep modulation. The line represents theoretical output characteristics.

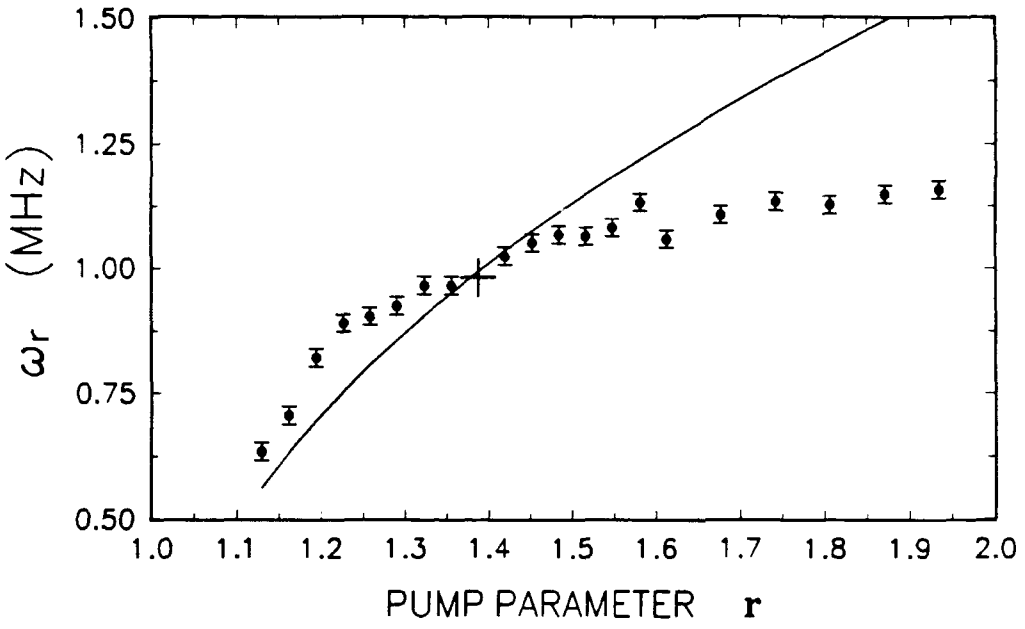


Figure 5.6: Variation of oscillation frequency $\omega_r$ with pump parameter $r$. Experimental points are from waveforms averaged over ten sweeps. The data point with the cross indicates the waveform used to extract parameters for the theoretical curves in Figs. 5.4, 5.6, 5.7 and 5.9.

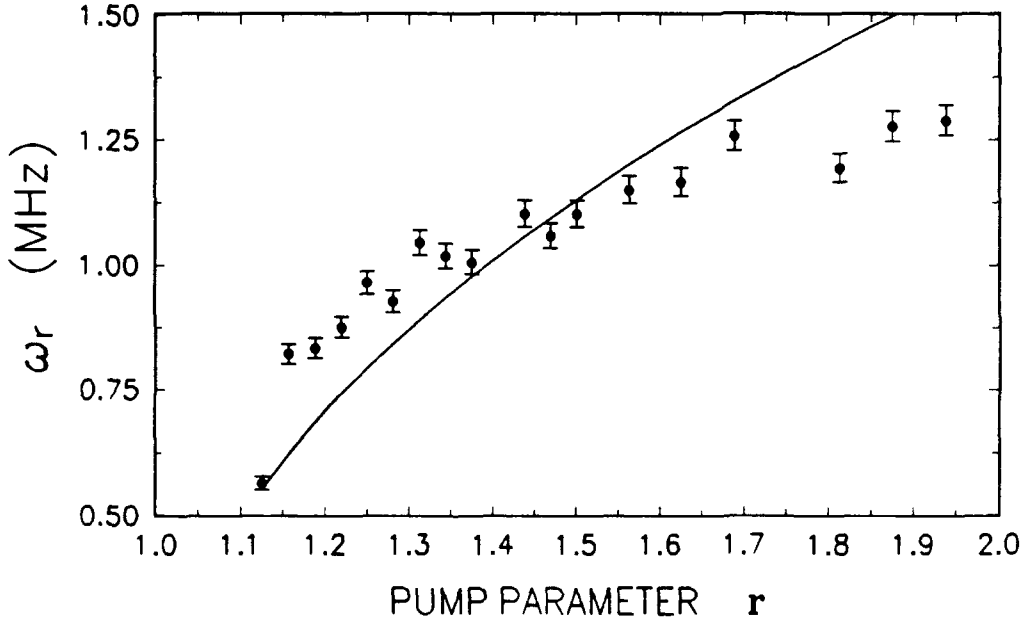


Figure 5.7: Variation of oscillation frequency $\omega_r$ with pump parameter $r$ for shallow cavity loss modulation. Experimental points are from single sweep waveforms. The continuous curve represents theoretical predictions based on Eq. (4.29). Parameters $\gamma_1$ and $\gamma_2$ were extracted from a single deep modulation waveform averaged over ten sweeps for pump parameter $r = 1.39$.

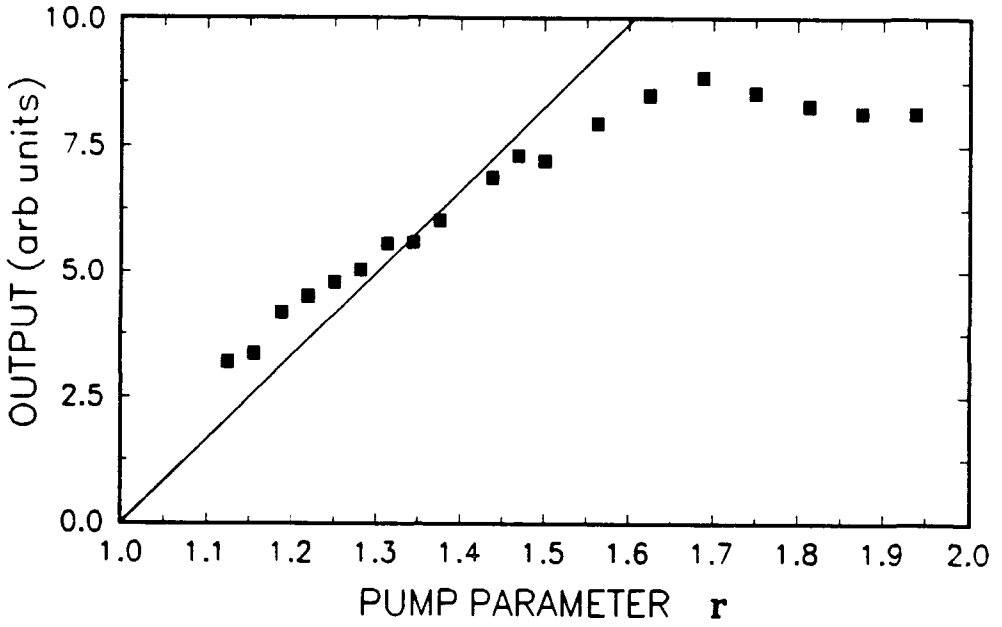


Figure 5.8: Variation of laser output power as a function of pump parameter $r$ for shallow modulation. The line represents theoretical output characteristics.

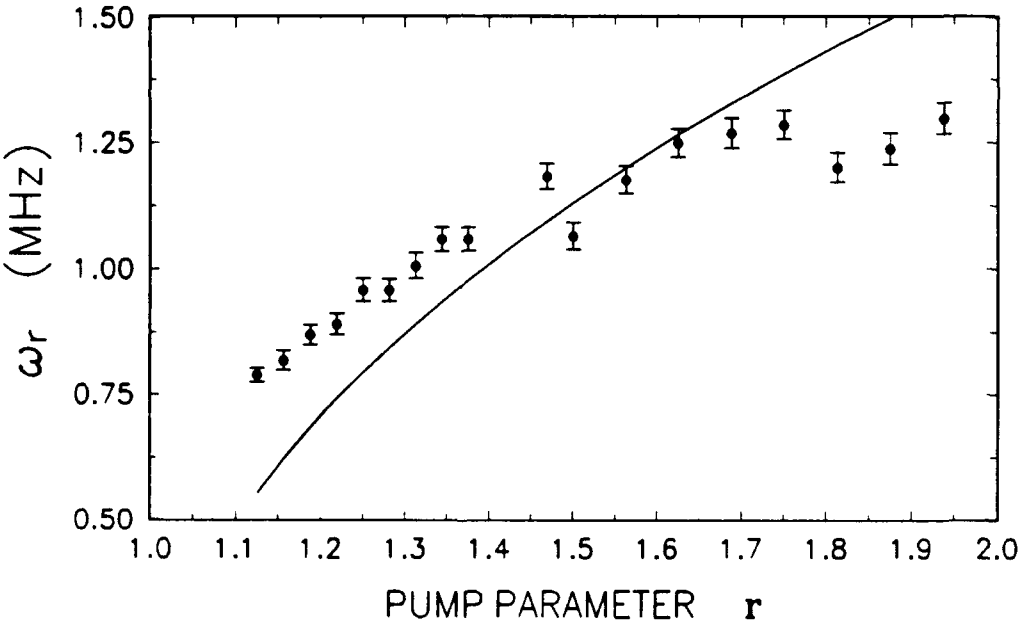


Figure 5.9: Variation of oscillation frequency $\omega_r$ with pump parameter $r$ for shallow cavity modulation. Experimental points are from waveforms averaged over ten sweeps. The continuous curve represents the theoretical predictions based on Eq. (4.29). Parameters $\gamma_c$ and $\gamma_2$ were extracted from a single deep modulation waveform averaged over ten sweeps for pump parameter $r = 1.39$.

This experiment was repeated to explore the role of noise, intrinsic or extrinsic, in the experiment. The same experimental procedure was used, with the exception that only single sweep waveforms were recorded. All parameters were then extracted from a single waveform as opposed to a waveform averaged over ten sweeps. The result for the upper state lifetime was

$$\boxed{\tau_2 = 3.48 \pm .18 \mu\text{sec}}. \tag{5.17}$$

and the cavity loss was determined to be

$$\boxed{\ell_c = (3.6 \pm .4)\ \%\ \text{per pass}}. \tag{5.18}$$

The plots in Figs. 5.10 through 5.13 show the observed and predicted spiking and relaxation oscillation frequency and the corresponding output power as a function of pump parameter. No error bars are shown in Fig. 5.12 since in many cases there were only two peaks on the waveform. This single data point did not allow an estimate of error in the period or frequency of oscillation.

### 5.2.3 Discussion of Results

The close agreement between the two data collection runs for the values for the upper state lifetime $\tau_2$, and the intrinsic cavity loss $\ell_c$, suggests that noise did not significantly effect the experimental measurement of these quantities, except perhaps at lower operating points. The value for the upper state lifetime can be compared with other measurements whose primary objective was to measure this value precisely. Spectroscopic and lasing characteristics of Ti:sapphire have been of considerable interest ever since its potential as a broadly tunable solid state laser was recognized [1, 37, 38]. Experiments to determine the fluorescence lifetime of the $Ti^{3+}$ ion in $Al_2O_3$ have been carried out by monitoring the fluorescence decay after exciting a crystal with a pulse of radiation from a dye laser at various wavelengths [1, 39, 40]. The results of various experiments are consistent and show a temperature-dependent upper state lifetime. The lifetime has a maximum value of approximately 3.85 $\mu$sec below 200 K. It then decreases rapidly in the temperature range of 200 to 400 K to a value less than 1 $\mu$sec.

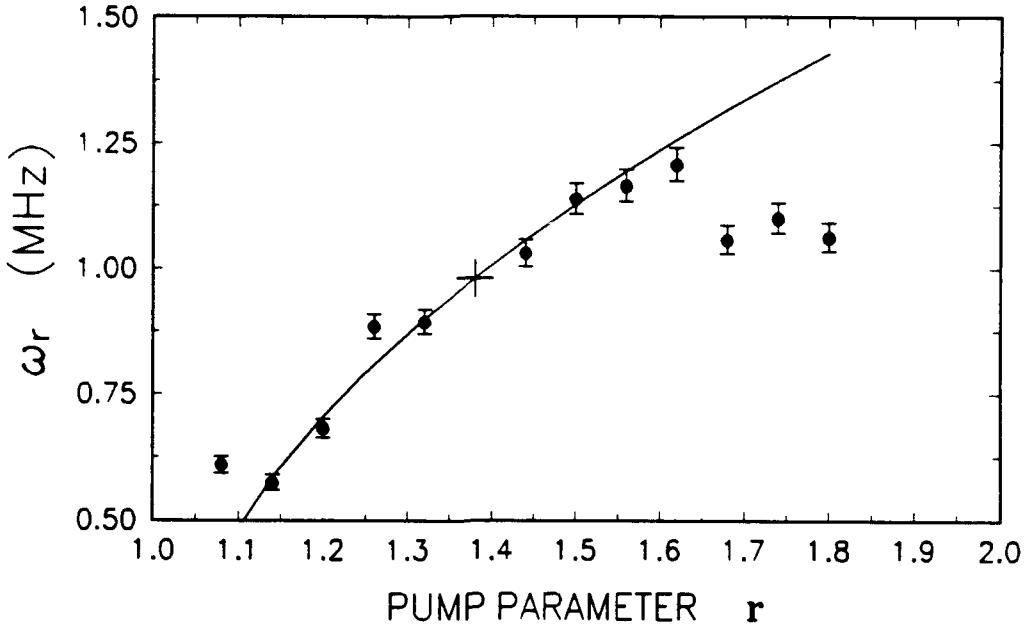


Figure 5.10: Variation of oscillation frequency $\omega_r$ with pump parameter $r$. Experimental points are from single sweep waveforms recorded with deep cavity loss modulation. The continuous line represents the theoretical curve from Eq. (4.29). The data point with the cross indicates the waveform used to extract parameters $\gamma_2$ and $\gamma_2$ for Figs. 5.10 and 5.12.

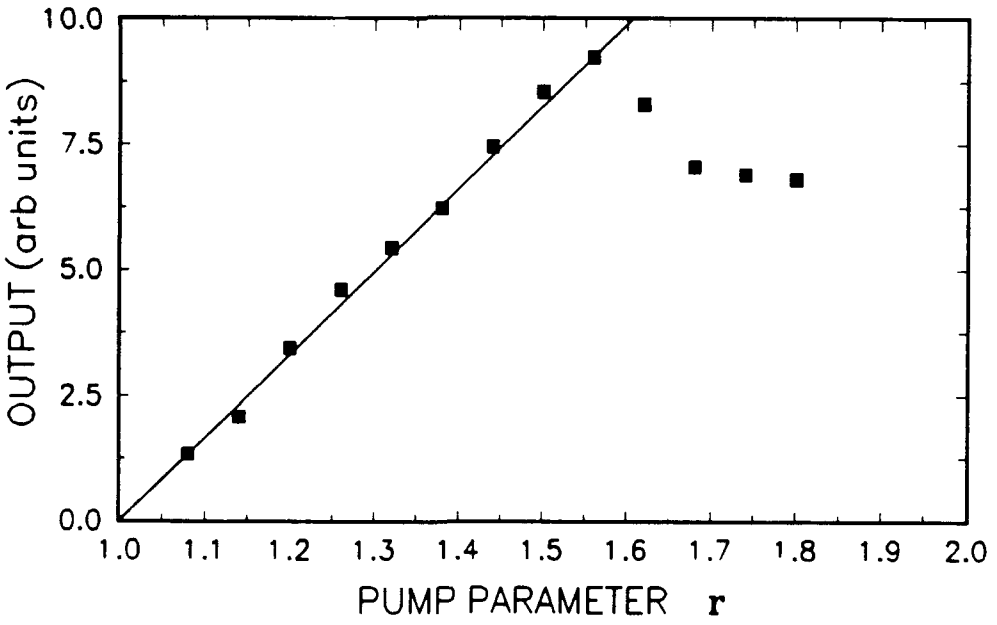


Figure 5.11: Variation of laser output power as a function of pump parameter $r$ for deep modulation in the second experiment. The line represents theoretical output characteristics.

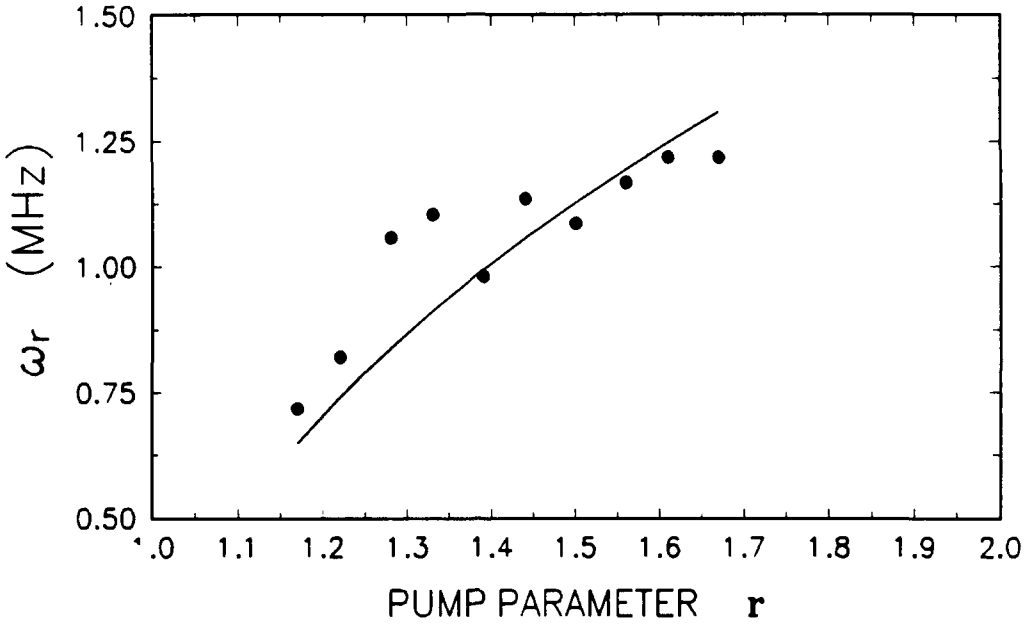


Figure 5.12: Variation of oscillation frequency $\omega_r$ with pump parameter $r$ for shallow cavity loss modulation. Experimental points are from single sweep waveforms. The continuous line represents theoretical predictions based on Eq. (4.29). Parameters $\gamma_c$ and $\gamma_2$ were extracted from a single sweep waveform for pump parameter $r = 1.38$.

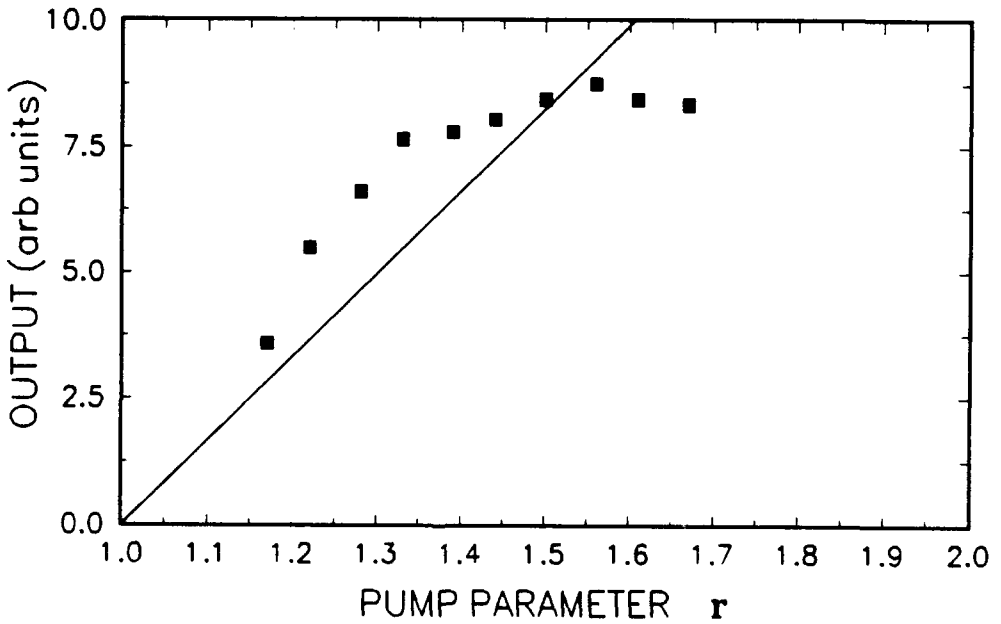


Figure 5.13: Variation of laser output power as a function of pump parameter $r$ for shallow modulation in the second experiment. The line represents theoretical output characteristics.

In our experiments, the crystal was cooled by circulating water in a jacket surrounding the crystal. Good thermal contact between the jacket and the crystal was achieved by wrapping the crystal with thin, flexible, copper foil. This cooling kept the crystal at a temperature of approximately 280 K. Extracting a value for the upper state lifetime from the published results [1, 39, 40] for this temperature gives a lifetime of 3.20 to 3.35 $\mu$sec. Our results are consistent with this value, within experimental error. This agreement gives support to our experimental method for determining the upper state lifetime $\tau_2$ by analyzing the relaxation oscillations. Further, this agreement suggests that the assumptions made in deriving the equations governing the relaxation oscillations in Section 4.2 were indeed valid.

The value of the intrinsic cavity loss $\ell_c$ is unique to our laser system. Therefore it can only be compared with a measurement of the cavity loss by a method independent of the relaxation oscillations. This measurement was the primary objective of the second set of experiments, the results of which are described in Section 5.3.

To see how well the rate equation model is able to predict the observed behavior of the laser, we compare the experimental results with the theoretical predictions based on Eq. (4.29) in Figs. 5.4, 5.6, 5.7, 5.9, 5.10, and 5.12. Such a comparison shows that the general behavior of the relaxation oscillation frequency follows the theoretical prediction at low pump parameters ($r < 1.5$). At higher pump parameters however, noticeable deviations from the predicted behavior appear. This same behavior is observed in the output power of the laser, as shown in Figs. 5.5, 5.8, 5.11, and 5.13. The output power should increase linearly with increased pump power, as depicted by the continuous line in these figures. This deviation of laser output from a linear dependence on the pump parameter has been observed in other experiments [22, 41]. This departure from the expected output power is probably due to temperature changes inside the mode volume of the crystal at higher pump powers. As previously noted, the upper state lifetime $\tau_2$ is temperature dependent, with a steep slope in the room temperature operating regime. This means that a small change in the temperature inside the crystal can result in a significant change in the upper state lifetime. Recalling the small gain coefficient given in Eq. (4.56), we see that the gain of the laser has a linear dependence on the upper state lifetime. A shorter upper

state lifetime reduces the gain per pass inside the laser and hence would decrease the output. This would have the same effect as lowering the pump parameter $r$, since the threshold for lower gain requires greater pumping.

The effect that a change in the upper state lifetime would have on the relaxation oscillation frequency can be determined by analyzing Eq. (4.29). The dominant frequency is $\omega_0$, found in the first term of the square root and defined in Eq. (4.16). Since $r$ decreases with a decreasing upper state lifetime, we would anticipate that the relaxation oscillation frequency would decrease as the temperature inside the crystal goes up. This is what is seen in Figs. 5.4, 5.6, 5.7, 5.9, 5.10, and 5.12. At lower pump parameters, in the range of $r = 1.0$ to 1.5, the observed relaxation oscillation frequency agrees with the predictions of Eq. (4.29) derived in Section 4.2. This suggests that the simple laser rate equations (4.1) and (4.3) describe the dynamics of the laser system well for lower pump parameters, where thermal effects can be ignored.

### 5.2.4 Results of Numerical Modeling

We also analyzed the data obtained from our experiments in terms of a model that describes the dynamics of the system. This comparison between theory and experiment is more detailed than that based solely on Eq. (4.29) and provides a much more stringent check of the validity of the simple rate equation model. In Section 4.3, a method for modeling the laser rate equations (4.1) and (4.3) of Section 4.1 was presented. For a loss modulated system, the appropriate equations of motion were given by Eqs. (4.43) and (4.44). These equations were solved numerically with experimentally measured parameters using the Runge–Kutta method of algorithms. Computer-generated waveforms were then produced based on these solutions for comparison with the recorded waveforms. Using this technique, we modeled several waveforms selected at random. The method in which the computerized model "laser" was used to generated the various waveforms is as follows.

For deep modulation, the model equations were solved starting at $t = 0$ with the number of atoms in the upper lasing state at the scaled stationary state value of $p$ as defined in Eq. (4.48). Using the results from our first experiment for $\gamma_2$ (5.8) and

$\gamma_2$ (5.15) into Eq. (4.45), the equation for the modulating parameter, we find

$$p = \frac{\gamma_c}{\gamma_2} \approx 31.9 \,. \tag{5.19}$$

The normalized pumping rate $R$ was set as defined by Eq. (4.46) using the pump parameter of the waveform being modeled and the value of $p$ given in Eq. (5.19). We started with the laser "off" initially. For this, the value for the number of photons in the cavity was first estimated to be $10^{-10}$, based on the value of the saturation photon number $q_s$ defined in Eq. (4.33). The actual number of photons in the cavity mode is indeterminant because of spontaneous emission noise. The initial number of photons was adjusted to get the model laser to initiate buildup at approximately the same time as the recorded waveform. With the parameters initialized as described, the waveform generated by the model represents the turn on of a laser recovering from deep modulation.

Comparisons of the measured and model-generated waveforms for deep cavity loss modulation are shown in Figs. 5.14–5.17. The model-generated waveforms are represented by the continuous curve and the measured waveform by the dotted curve. Figure 5.14 compares a single sweep waveform at pump parameter $r = 1.29$ with the model predictions and Fig. 5.15 compares a waveform averaged over ten sweeps with the model predictions at the same pump parameter. Figure 5.16 compares a single sweep waveform at pump parameter $r = 1.39$ with the model predictions and Fig. 5.17 compares a waveform averaged over ten sweeps at the same pump parameter.

For shallow modulation, the initial values for the model laser were chosen in the same manner as for deep modulation, except that the cavity photon number was set to its stationary state value $(r - 1)$, as defined by Eq. (4.47). The loss parameter $p$ was then modulated at a frequency corresponding to the modulating frequency of the AOM in the actual experiment. The model was allowed to "run" long enough to eliminate transient effects of the initial conditions. Since the exact depth of cavity loss modulation was not known for the relaxation oscillation experiments, the depth of modulation for $p$ was determined by varying the fractional change in $p$ until the steady state values of the recorded and modeled waveforms overlapped. The actual depth of modulation for the cavity loss was then estimated from this fractional

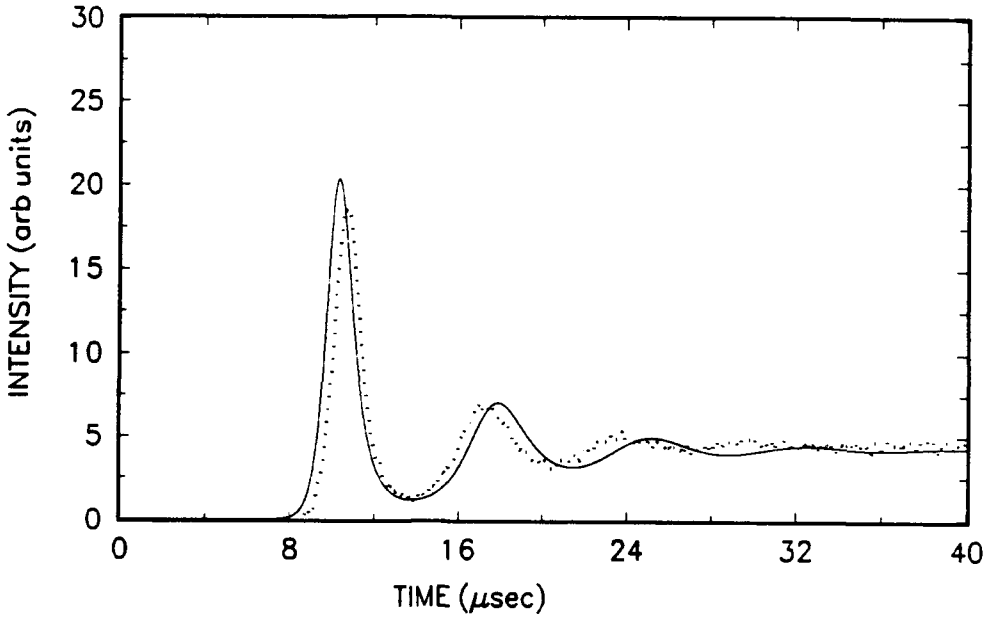


Figure 5.14: A comparison of recorded and modeled waveforms representing the spiking oscillations of the Ti:sapphire laser with deep loss modulation. The solid curve depicts the modeled waveform generated by the model described in Section 4.3. The dotted curve represents the single sweep waveform recorded at $r = 1.29$.

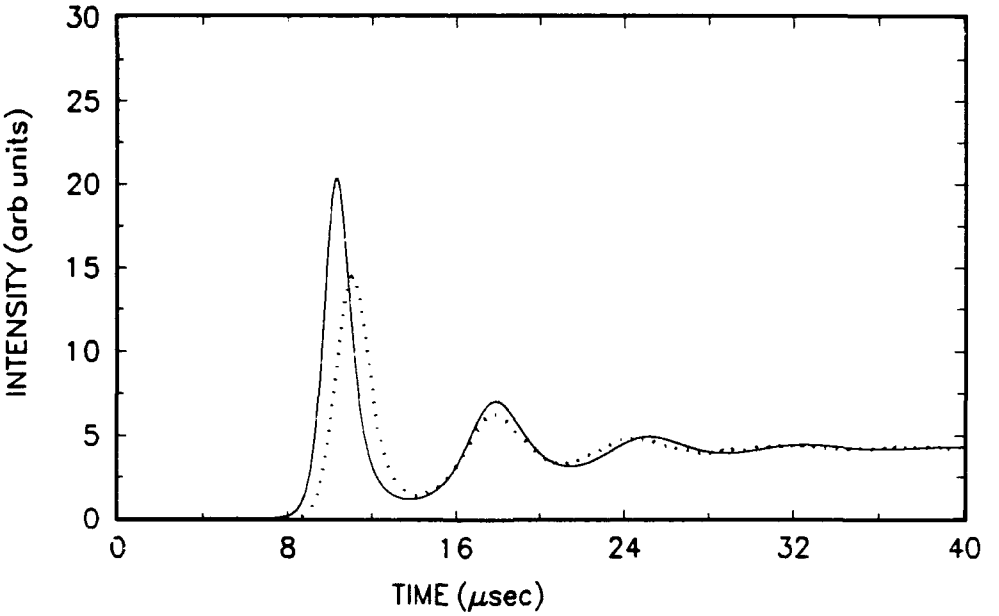


Figure 5.15: A comparison of recorded and modeled waveforms representing the spiking oscillations from deep loss modulation. The solid curve depicts the model-generated waveform and the dotted curve represents the recorded waveform averaged over ten sweeps at $r = 1.29$.

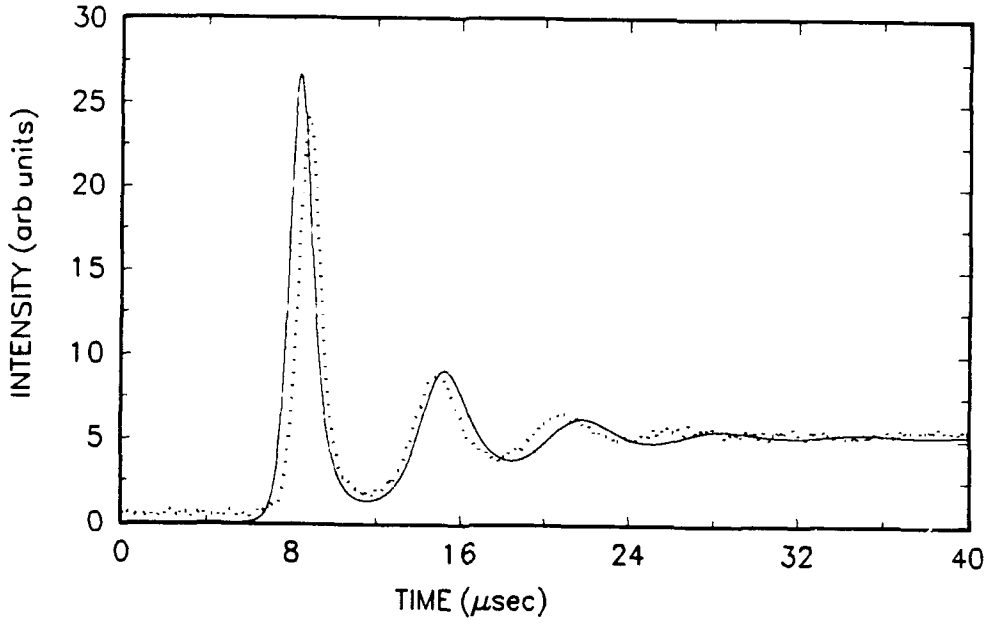


Figure 5.16: A comparison of recorded and modeled waveforms representing the spiking oscillations from deep loss modulation at pump parameter $r = 1.39$. The solid curve depicts the waveform generated by the model and the dotted curve represents the recorded single sweep waveform.

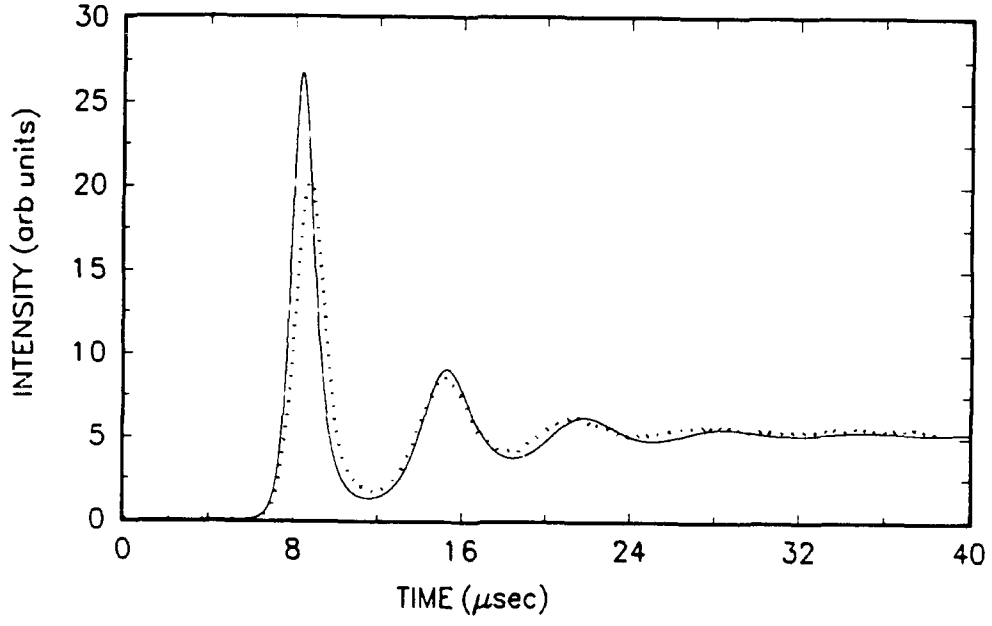


Figure 5.17: A comparison of recorded and modeled waveforms representing the spiking oscillations from deep loss modulation. The solid curve depicts the model-generated waveform and the dotted curve represents the recorded waveform averaged over ten sweeps at $r = 1.39$.

change in $p$. With the parameters for the model determined as described here, the generated waveforms represent a laser system being disturbed with shallow cavity loss modulation.

Figures 5.18–5.21 show the comparison between the model predictions and the measured waveforms for shallow cavity loss modulation. The model generated waveforms were adjusted on time scale to compensate for the trigger delay in the recorded waveforms. The depth of loss modulation for all modeled waveforms was about 0.3 %. Figure 5.18 shows a comparison of a single sweep waveform recorded at pump parameter $r = 1.28$ with the model prediction. A waveform averaged over ten sweeps at the same pump parameter compared with the model prediction is shown in Fig. 5.19. Figures 5.20 and 5.21 compare the waveforms recorded at another pump parameter of value $r = 1.50$ for a single sweep and averaged over ten sweeps with the respective model predictions.

By comparing the recorded waveforms with the model-generated waveforms we conclude that the model describes the qualitative behavior of the laser from loss modulation well. Quantitative comparisons between the model and the actual laser behavior are limited by a number of factors. First is the fact that the recording of the actual laser behavior by the transient digitizer is limited by the speed of the digitizer. A comparison between the signal rise time on the oscilloscope and the rise time displayed on the recorded waveform indicated that the bandwidth of the transient recorder was less than that of the detector. Second, since the model uses experimentally measured parameters, uncertainty in the measured values will result in uncertainty in the modeled waveforms.

We can also derive conclusions based on the differences between the single sweep waveforms and those averaged over ten sweeps. For the deep modulation waveforms, the averaged waveforms consistently have shallower initial peaks or "spikes" than the waveforms recorded from single sweeps. For shallow modulation this difference is not as pronounced. Slight fluctuations in the time to reach this first peak would result in an overall decrease in the amplitude of the spike as it is averaged. This suggests that the rise time to the first peak fluctuates more from a cavity with deep loss modulation than for a cavity with shallow loss modulation. The source of this

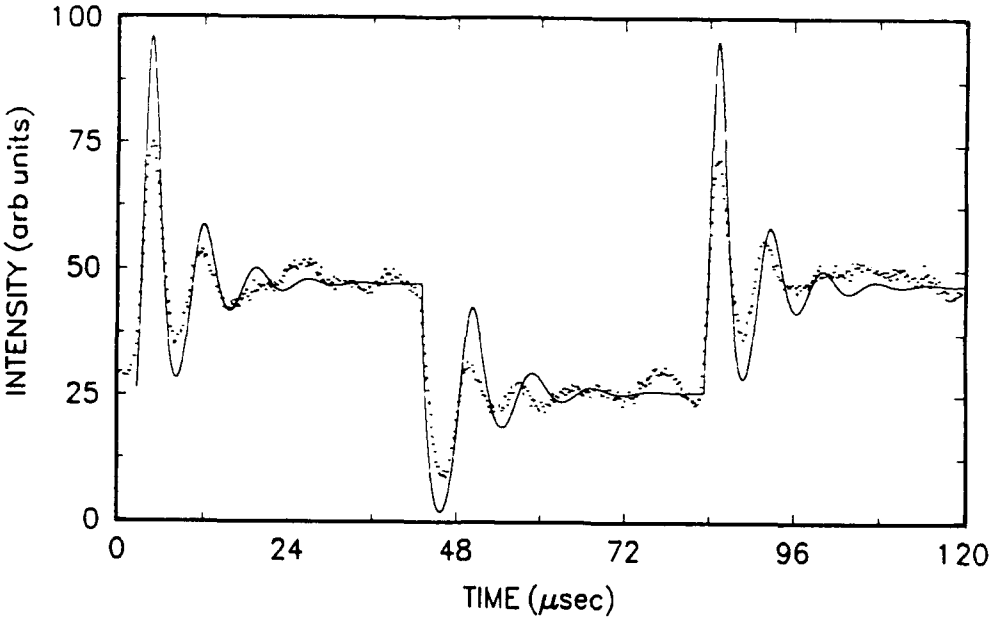


Figure 5.18: A comparison of recorded and modeled waveforms representing the relaxation oscillations of the Ti:sapphire laser with shallow loss modulation. The solid curve depicts the modeled waveform generated by the model described in Section 4.3. The dotted curve represents the single sweep waveform recorded at $r = 1.28$. Depth of loss modulation for the model was 0.3 %.

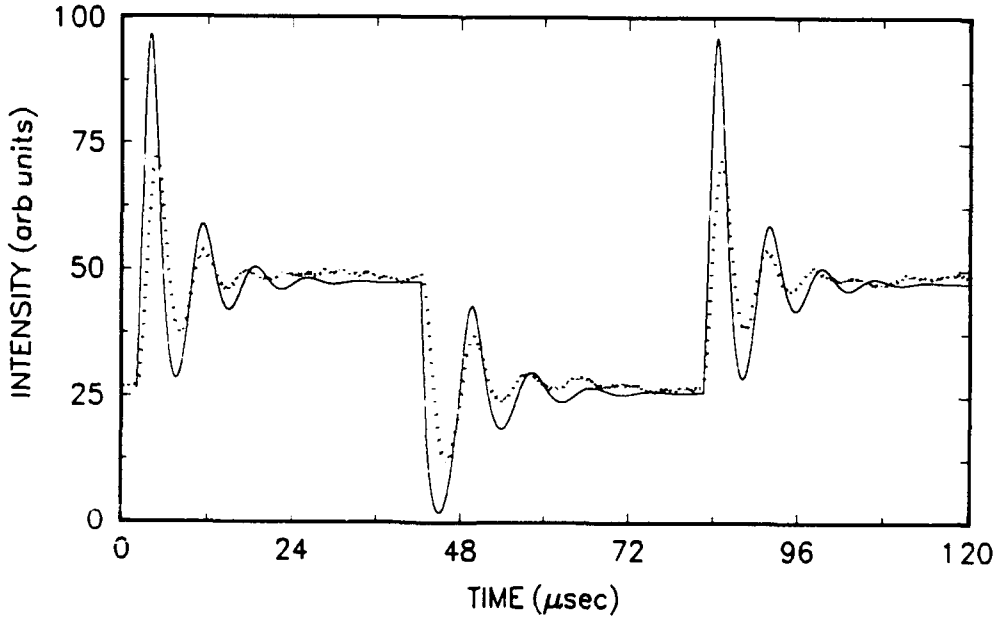


Figure 5.19: A comparison of recorded and modeled waveforms representing the relaxation oscillations from shallow loss modulation. The solid curve depicts the model-generated waveform and the dotted curve represents the recorded waveform averaged over ten sweeps at $r = 1.28$.

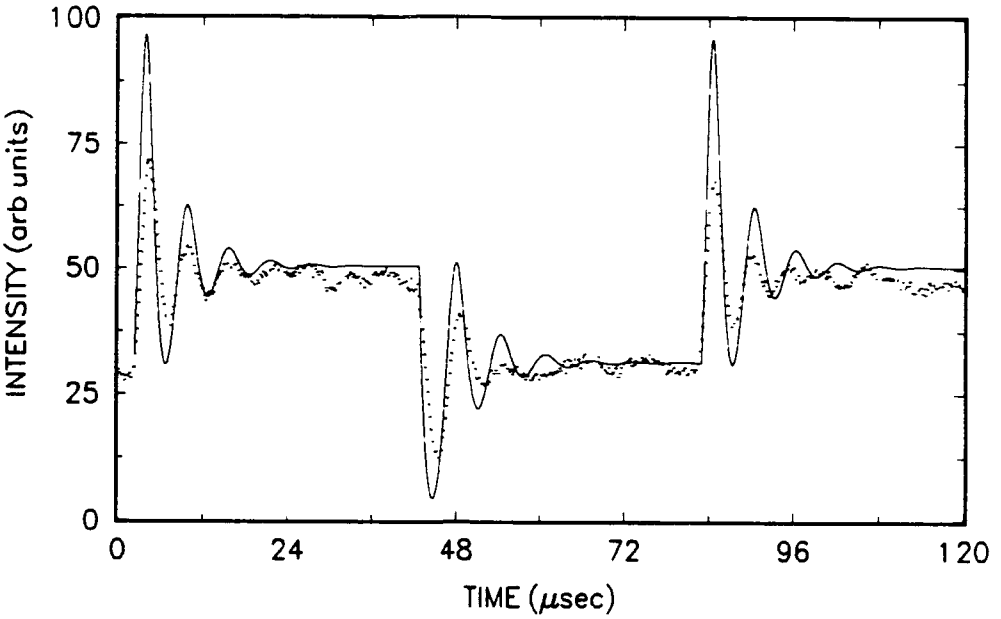


Figure 5.20: A comparison of recorded and modeled waveforms representing the relaxation oscillations from shallow loss modulation at pump parameter $r = 1.50$. The solid curve depicts the waveform generated by the model and the dotted curve represents the recorded single sweep waveform. Depth of loss modulation was 0.3 %.

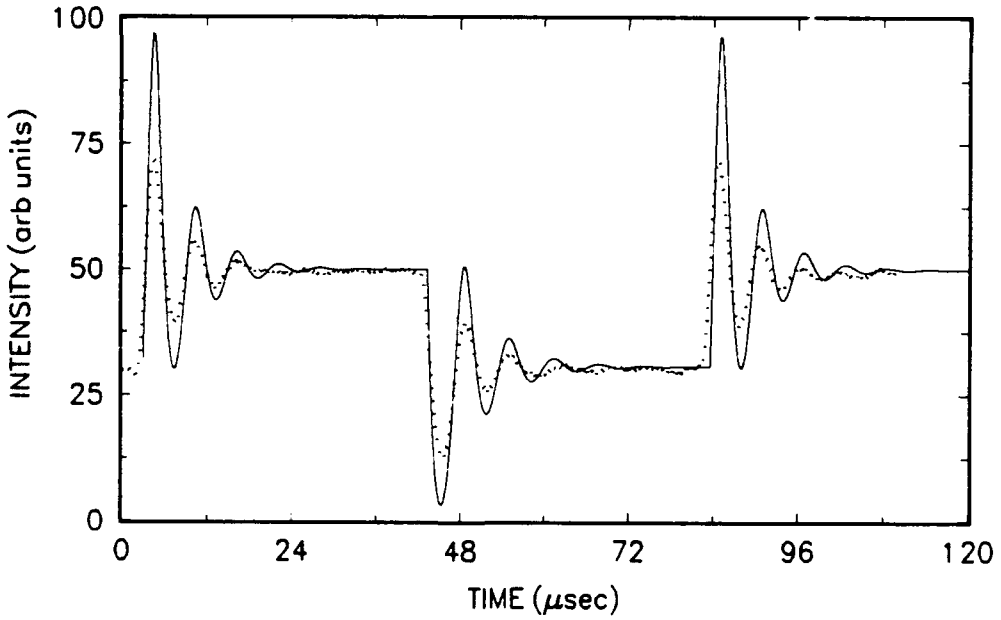


Figure 5.21: A comparison of recorded and modeled waveforms representing the relaxation oscillations from shallow loss modulation. The solid curve depicts the model-generated waveform. The dotted curve represents the recorded waveform averaged over ten sweeps at $r = 1.50$.

slight temporal fluctuation for the deep modulated cavity is quantum noise since the laser is off during the time the cavity suffers large loss. The buildup time to the first peak is dependent upon the number of photons inside the fundamental mode of the cavity. The buildup of the laser radiation starts once a population inversion has developed and a spontaneously emitted photon passes through the gain medium. The average time for laser buildup decreases as the number of photons present initially in the cavity increases. The study of this quantum noise and its deterministic effect on the rise time of a laser signal offers an excellent opportunity for further research.

## 5.3 Experiment 2: Cavity Losses

In Section 5.2, we described an experiment to measure the intrinsic loss of a laser system by studying its relaxation oscillations. In this section, we describe another experiment that was carried out to determine the intrinsic cavity losses. This method also allows us to determine the normalized pumping rate $R$ of our laser as defined by Eq. (4.46) and estimate the stimulated emission cross section $\sigma_{21}$ of the Ti:sapphire crystal. The theoretical background for this experiment is given in Section 4.4. To carry out this experiment, the loss offered by the acousto-optic modulator used in the experiment was calibrated. The experimental procedure consisted of measuring the threshold pump power as a function of the AOM loss.

### 5.3.1 Experimental Setup: AOM Calibration

Our objective in calibrating the AOM loss was to determine the percent loss out of the primary beam as a function of input voltage to the driver of the AOM. The AOM was placed at normal incidence immediately outside the Ti:sapphire laser cavity. The laser was then operated at a certain pump power above threshold. The light output from one of the cavity mirrors was allowed to pass through the AOM. The zero order beam in the transmitted light illuminated a photodetector. The detector was placed far enough away from the AOM to ensure sufficient separation between the zero and higher order diffracted beams so that they would not be detected. The signal from the photodetector was displayed on an oscilloscope and digitized and recorded by the

transient digitizer. The source of DC voltage to the AOM driver was a Power Designs, Inc. Model 6050A DC power supply. The carrier level (bias) on the driver was set to zero. The DC voltage to the driver was incremented in steps of 100 mV in the range from 0 to 1 V. Waveforms were recorded at each level of DC input to the driver. To minimize the effect of fluctuations in the pump and the Ti:sapphire laser, the waveforms were averaged over 100 sweeps. The recorded waveforms were then further time averaged over the 2 ms duration of the sweep to determine an average value for the light intensity. Any contribution from the detector offset was subtracted from the measured mean signal producing a number $N_x$, where $x$ represents the applied voltage to the driver and $N$ represents the average intensity of the transmitted beam. Percent loss for the applied voltage was determined according to the relation

$$\% \text{ loss induced by AOM} = \frac{N_0 - N_x}{N_0} \times 100 \,. \tag{5.20}$$

The data points showing % loss as a function of DC volts applied to the driver are shown in Fig. 5.22. The straight line is the best fit to the data points. The slope of this line gives the relationship between loss induced out of the primary beam and voltage applied to the AOM driver. This relationship was determined to be

$$\text{loss} = 0.0121\%/\text{mV} \,. \tag{5.21}$$

The uncertainty in this value is less than 0.15% of the measured value.

### 5.3.2 Experimental Setup: Cavity Losses

Once the AOM was calibrated, it was placed at normal incidence in the long arm of the cavity. All intracavity elements were adjusted to minimize the threshold, which was determined to be at 4.75 watts of pump power. Output from the laser was monitored by a high gain detector from reflections off one of the Brewster windows of the crystal as shown in Fig. 5.23. This light was filtered with a colored glass filter and focused onto the detector. The signal from the detector was monitored with an oscilloscope. The threshold condition was defined as the point at which the fluctuations in the signal were equal to the average of the signal. The intensity of the

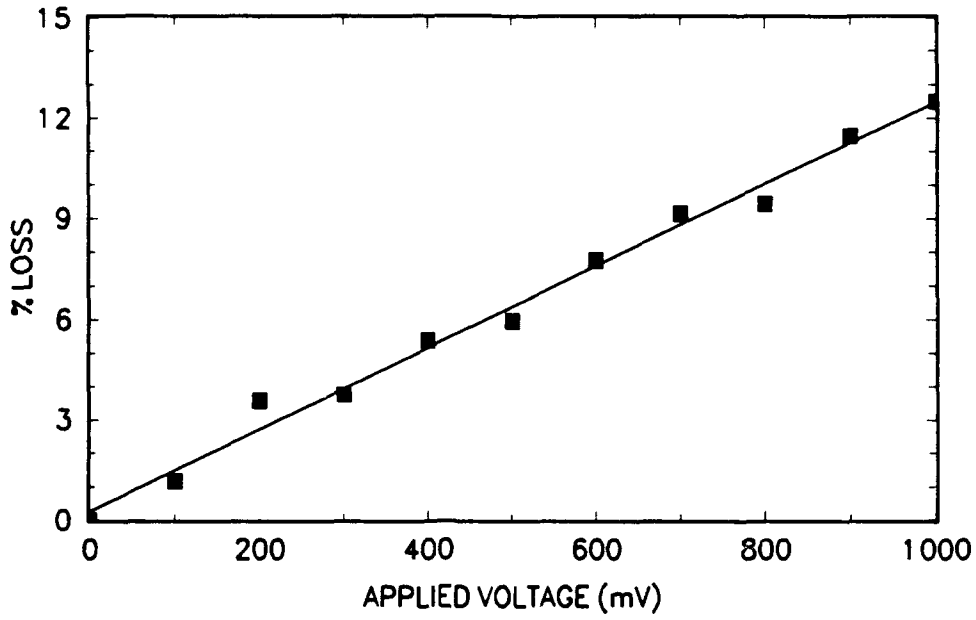


Figure 5.22: Loss calibration curve for the IntraAction Corp. acousto-optic modulator used in the relaxation oscillation and the cavity loss experiments. Data were taken at normal incidence using output from the Ti:sapphire laser.

pump power was measured using a photodetector monitoring the reflections of pump light from the cavity curved mirror, as shown in Fig. 5.23. The reflected light was attenuated through a series of neutral density filters.

Voltage applied to the AOM driver was incremented in steps of approximately 30 mV. The range of applied voltage was from zero to a maximum of approximately 200 mV. At the level of loss corresponding to 200 mV to the driver, the pump power was insufficient to overcome the AOM induced loss. At each increment of voltage to the AOM driver, the pump power was increased until the laser threshold condition was met. For each value of voltage applied (mV) to the AOM, threshold pump power was recorded from the output of the detector in volts. This process was repeated three times in succession. Each measurement was converted into data points as follows. The voltage applied to the AOM driver was converted into percent loss based on the formula given in Eq. (5.21). The signal from the photodetector was converted into watts of pump power by using the formula

$$\text{Watts} = [0.9 \times \text{signal voltage}] \times 2.0 \tag{5.22}$$

This formula was determined by calibrating the output voltage from the photodetector against the output power readings from the meter on the power supply of the pump

laser. The voltage from the detector was recorded at two values of pump power ($\approx 5$ and 10 watts) as indicated on the meter on the power supply. This voltage was then reduced by the voltage reading obtained from the detector when the incident beam was blocked with a beam dump and only background light was detected. This reduction represented approximately 10% of the "unblocked" value. The resulting voltage readings corresponding to the two pump power settings were compared with the power meter readings to establish a scale factor of $\approx 2$.

### 5.3.3 Results

All the data points of % loss with threshold pump power were then plotted and fitted with a line of minimum regression. The results are shown in Fig. 5.24. The data points are shown for only two of the three runs to minimize overcrowding of the data points. The straight line depicts the best fit to all data points. The intercept of the straight line on the $\ell_{AOM}$ axis gives the value of $\ell_c$, the intrinsic cavity loss, in accordance with Eq. (4.54). The measured value for the intrinsic cavity loss $\ell$ from these measurements is

$$\boxed{\ell_c = (2.95 \pm .35)\%}. \tag{5.23}$$

In order to determine the normalized pumping rate $R$ defined by Eq. (4.46), we measured the slope of the line of regression. As described in Section 4.4, the slope represents $g$, the percent gain per pass through the cavity per watt of pump power. The measured value of $g$ was

$$\boxed{g = (0.707 \pm 0.011)\ \%\ \text{per watt per pass}}. \tag{5.24}$$

Using this value in Eq. (4.55) with the upper state decay rate determined from the first experiment we find

$$\boxed{R = [7.36 \pm .38] \times W_p}. \tag{5.25}$$

This experiment also allows us to estimate the gain cross section of the medium with the help of Eq. (4.56). The efficiencies in Eq. (4.56) were estimated as follows. The quantum efficiency could not be measured directly, but we estimated it to be

$$\eta_0 \approx 0.8 \tag{5.26}$$

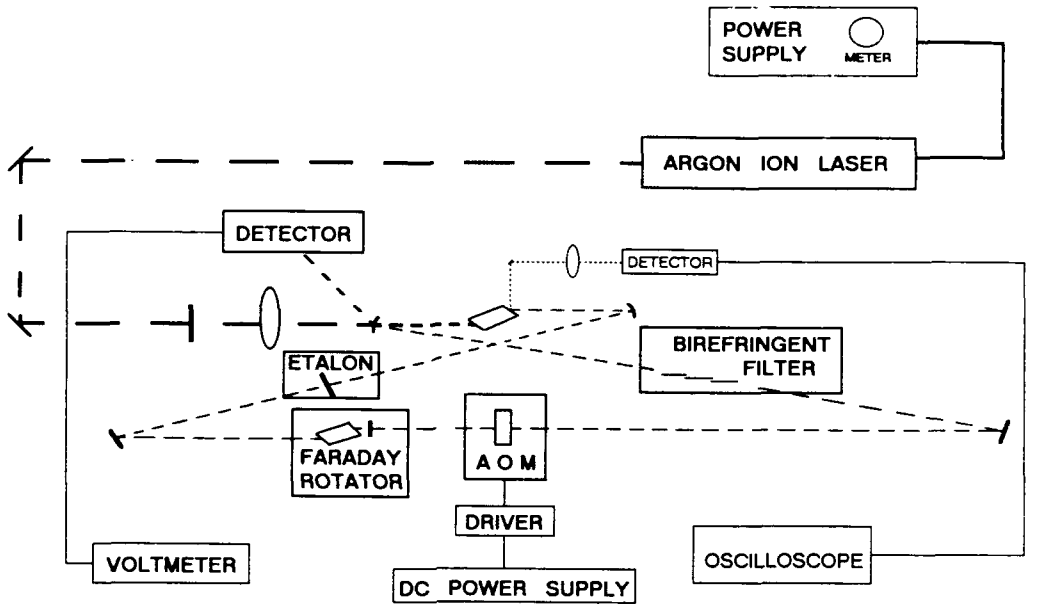


Figure 5.23: The experimental setup for conducting the cavity loss experiment using the AOM to vary cavity loss. The dashed lines represent optical paths and the solid lines represent electrical paths.

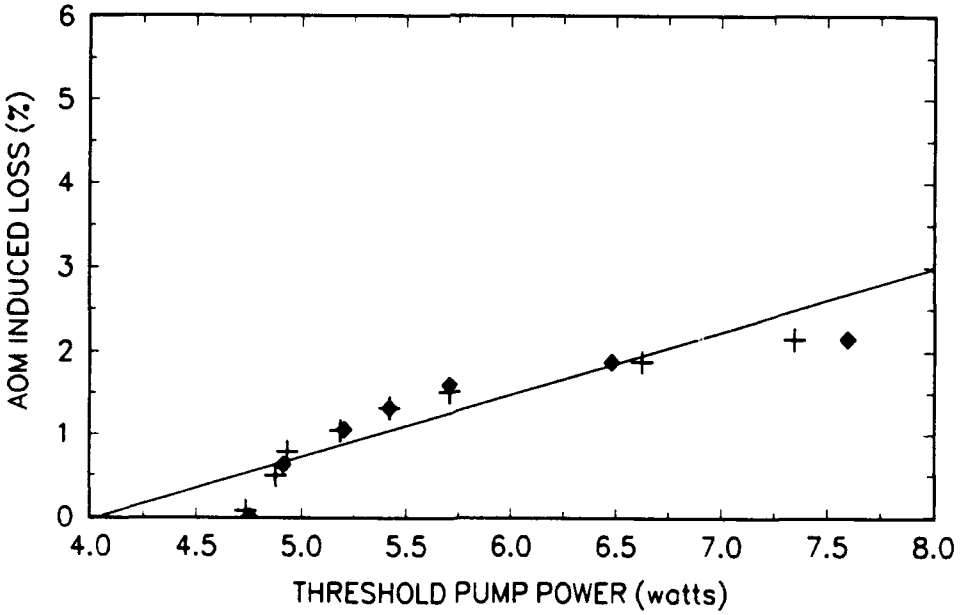


Figure 5.24: Variations of threshold pump power with intracavity AOM induced loss. The data points are shown for two of the three runs. The straight line represents the best fit to all data points.

based on previous experiments [1, 10, 12]. The energy efficiency $\eta_1$ was determined from Eq. (4.57) using 500 nm as the average wavelength of the pump photons and 780 nm as the average wavelength of a laser photon

$$\eta_1 \approx 0.64 \,. \tag{5.27}$$

The primary loss in the transmission of the pump beam to the crystal was from reflections off the curved cavity mirror prior to the crystal. Measurements of this reflected beam compared with the output from pump laser showed a consistent loss of 28%. This gives an efficiency $\eta_2$ of

$$\eta_2 = 0.72 \,. \tag{5.28}$$

Single pass absorption measurements of the crystal showed that approximately 83% of the pump beam was absorbed by the crystal over a pumping range of 0.5 to 7.0 watts. This gives

$$\eta_3 = 0.83 \,. \tag{5.29}$$

To determine $A$, the average cross sectional area of the pump beam inside the crystal, we refer to the mode matching problem described in Section 3.4 and the characteristics of the spot size at the beam waist given in Section 2.3. For our cavity, the spot size at the beam waist was estimated to be 25 microns (see Figs. 3.4 and 3.5). Since the crystal is 2 cm long, we take the average spot size to be at a position 50 mm inside the crystal ($z = 50$ mm). To determine the spot size at this location, we use Eqs. (2.44) and (2.49) to obtain

$$w_{avg} \approx 40 \text{ microns} \,. \tag{5.30}$$

giving an average cross sectional area of the pump beam

$$A \approx 5 \times 10^{-5} \text{ cm}^2 \,. \tag{5.31}$$

Using these values in Eq. (4.58), we estimate the the stimulated emission cross section to be

$$\boxed{\sigma_{21} \approx 1.4 \times 10^{-19} \text{ cm}^2} \,. \tag{5.32}$$

### 5.3.4 Discussion of Results

The close agreement in the measured values for the intrinsic cavity loss $\ell_i$ between this experiment and the relaxation oscillation experiments suggests that both experimental techniques are reliable. Indeed, a procedure based on variable loss similar to that used in the second set of experiments has been used by Sanchez *et al.* to measure the intrinsic loss of a Ti:sapphire laser [41]. However, the technique of determining cavity losses by analyzing the relaxation oscillations of a laser is a new technique that can be easily applied to other solid state lasers.

For our results, the slightly higher value for the intrinsic cavity loss from the first experiment is probably due to an increase in thermal losses with increased pumping power. The values of loss from the first set of experiments were measured from data obtained while the crystal was being pumped with approximately 6.5 watts from the pump laser ($r = 1.39$ and $W_{th} = 4.75$ watts). Comparing this pump power with the pump power used in the second set of experiments (see Fig. 5.24), we see that the data from the second experiment was for the most part obtained using lower pump powers.

Schulz gives an excellent account of the thermal effects in the Ti:sapphire crystal in [22]. He estimates that between 30 and 45 percent of the power absorbed by the crystal is deposited as heat, resulting in thermal lensing and a change in the index of refraction inside the crystal. Both of these effects have the result of "detuning" the cavity or increasing loss.

The gain cross section has been measured using several different experimental techniques [1, 38, 40, 41, 42, 43]. The measured values range from $6.5 \times 10^{-20}$ cm$^2$ to $1.5 \times 10^{-19}$ cm$^2$ depending on technique and wavelength used in the measurement. Our result agrees well with these measurements.

In this chapter we have described in detail the laser system used to conduct two different experiments. The simple laser rate equation approximations developed in Chapter 4 seem to describe well the dynamical behavior of the Ti:sapphire relaxation oscillations. The cavity loss experiments confirmed that the intrinsic cavity losses can be determined from relaxation oscillations. Both sets of experiments open up many opportunities for studying the dynamics of Ti:sapphire lasers. Some of these will be

discussed in Chapter 7.

# Chapter 6

## Polarization Properties of Gaussian Beams

Our treatment of laser beams in Chapter 2 was within the framework of the scalar wave equation (2.7) and the paraxial approximations (2.23) and (2.24). For most applications which do not involve the polarization properties of laser beams, this framework is quite adequate. Indeed, the cavity design and experiments described in this thesis were developed within this framework. When describing the polarization properties of laser beams however, a scalar representation is inadequate. Even for a linearly polarized laser beam, a scalar description of a finite cross section laser beam is inconsistent with Maxwell's equations (2.1)–(2.4). The transverse nature of the electromagnetic field expressed by Eqs. (2.1) and (2.3) implies that the spatial variation of the field in directions transverse to the direction of propagation is coupled to the polarization properties of the field. Thus it is well known that spatial variation of the field in the direction of polarization gives rise to a longitudinal field component [44]. This coupling of the transverse spatial variation of nonplanar wavefronts to polarization was investigated in an interesting paper by Fainman and Shamir [45]. They analyzed the cross polarization in a spherical wavefront from a point source. They also recorded experimentally the cross polarization of a linearly polarized fundamental Gaussian beam passing through a pin hole. Simon, Sudarshan and Mukunda [44] used an analysis of Maxwell's equations in the relativistic front form to establish the polarization properties of the fundamental Gaussian laser beams. Several other approaches to this problem have been discussed, including potential formulation of Maxwell's equations [46, 47] and a power series expansion of electromagnetic fields [48]. In this chapter, we present another approach to this problem. Our approach is simpler and more direct and allows us to establish the general polarization structure of paraxial Hermite–Gaussian modes of a laser. We also present

experimental evidence for this structure using the linearly polarized beam from an argon ion laser.

## 6.1 Paraxial Solutions to Maxwell's Equations

In Chapter 2, we derived the paraxial wave equation (2.26) and developed a solution representing the basic characteristics of Gaussian beams. In this section, we determine the form of paraxial solutions to Maxwell's equations which allow us to better represent the polarization properties of laser beams. For quasi- monochromatic fields propagating in the $z$-direction, we write the electric and magnetic fields of the wave as

$$\tilde{\mathbf{E}}(\mathbf{r},t) = \mathbf{E}(\mathbf{r})e^{i(kz-\omega t)} \equiv (E_1(\mathbf{r})\hat{\epsilon}_1 + E_2(\mathbf{r})\hat{\epsilon}_2 + E_3(\mathbf{r})\hat{\epsilon}_3)\, e^{i(kz-\omega t)}\,. \tag{6.1}$$

$$\tilde{\mathbf{B}}(\mathbf{r},t) = \mathbf{B}(\mathbf{r})e^{i(kz-\omega t)} \equiv (B_1(\mathbf{r})\hat{\epsilon}_1 + B_2(\mathbf{r})\hat{\epsilon}_2 + B_3(\mathbf{r})\hat{\epsilon}_3)\, e^{i(kz-\omega t)}\,. \tag{6.2}$$

Here $\mathbf{E}(\mathbf{r})$ and $\mathbf{B}(\mathbf{r})$ describe the transverse spatial profile of the beam and $\hat{\epsilon}_1$, $\hat{\epsilon}_2$, and $\hat{\epsilon}_3$ are unit vectors along the $x$, $y$, and $z$-axes respectively. For the fields in Eqs. (6.1) and (6.2) Maxwell's equations in free space become

$$ikE_3(\mathbf{r}) + \nabla\cdot\mathbf{E}(\mathbf{r}) = 0\,, \tag{6.3}$$

$$ik\hat{\epsilon}_3\times\mathbf{E}(\mathbf{r}) + \nabla\times\mathbf{E}(\mathbf{r}) = ikc\mathbf{B}(\mathbf{r})\,, \tag{6.4}$$

$$ikB_3(\mathbf{r}) + \nabla\cdot\mathbf{B}(\mathbf{r}) = 0\,, \tag{6.5}$$

$$ik\hat{\epsilon}_3\times\mathbf{B}(\mathbf{r}) + \nabla\times\mathbf{B}(\mathbf{r}) = -i\frac{k}{c}\mathbf{E}(\mathbf{r})\,. \tag{6.6}$$

From these equations we see that each cartesian component of the electric and magnetic field satisfies the scalar wave equation (2.7). For paraxial beam like solutions, the inequalities defining the paraxial approximation Eqs. (2.23) and (2.24) hold for each field component and each component satisfies the paraxial wave equation (2.26). These components are not arbitrary. They are coupled via Eqs. (6.3)-(6.6). In the paraxial approximation of Eqs. (2.23) and (2.24), Eqs. (6.3) and (6.5) allow us to express the longitudinal field components in terms of the transverse field components

$$E_3(\mathbf{r}) = \frac{i}{k}\left(\frac{\partial E_1}{\partial x} + \frac{\partial E_2}{\partial y}\right)\,. \tag{6.7}$$

AD-A254 264 SYSTEM DESIGN AND RELAXATION OSCILLATIONS OF A TITANIUM-SAPPHIRE LASER(U) AIR FORCE INST OF TECH WRIGHT-PATTERSON AFB OH W L ERIKSON AUG 92 2/2

UNCLASSIFIED AFIT/CI/CIA-92-072 XF-AFIT NL

END
FILMED
DTIC

# IMAGE EVALUATION TEST TARGET (MT-3)

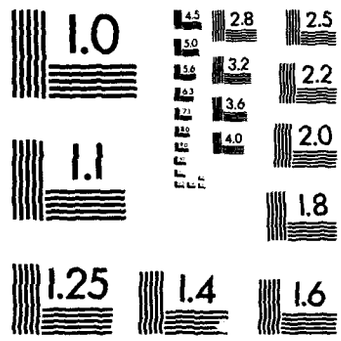


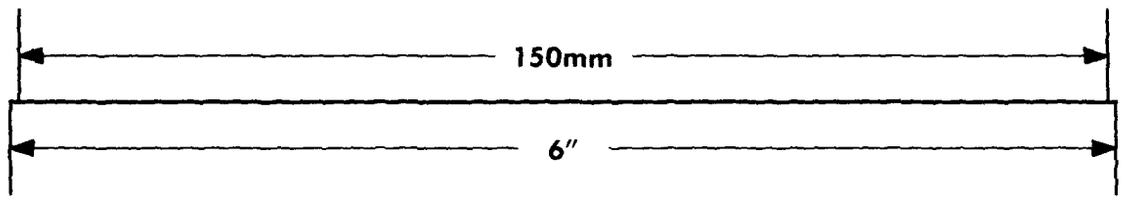


**PHOTOGRAPHIC SCIENCES CORPORATION**
770 BASKET ROAD
P.O. BOX 338
WEBSTER, NEW YORK 14580
(716) 265-1600

$$B_3(\mathbf{r}) = \frac{i}{k}\left(\frac{\partial B_1}{\partial x} + \frac{\partial B_2}{\partial y}\right) . \tag{6.8}$$

where we have used the inequality from Eq. (2.23) in arriving at these equations.

Using Eq.(6.4) we can express the magnetic field components in terms of the electric field components as

$$cB_1(\mathbf{r}) = -E_2 + \frac{1}{2k^2}\left(\frac{\partial^2 E_2}{\partial y^2} - \frac{\partial^2 E_2}{\partial x^2}\right) + \frac{1}{k^2}\frac{\partial^2 E_1}{\partial x \partial y} . \tag{6.9}$$

$$cB_2(\mathbf{r}) = E_1 + \frac{1}{2k^2}\left(\frac{\partial^2 E_1}{\partial y^2} - \frac{\partial^2 E_1}{\partial x^2}\right) - \frac{1}{k^2}\frac{\partial^2 E_2}{\partial x \partial y} . \tag{6.10}$$

$$cB_3(\mathbf{r}) = -\frac{i}{k}\left(\frac{\partial E_2}{\partial x} - \frac{\partial E_1}{\partial y}\right) . \tag{6.11}$$

Similarly, using Eq. (6.7) and the paraxial wave equation (2.26) in Eq. (6.6), we can express the electric field components in terms of the magnetic field components

$$E_1(\mathbf{r}) = c\left[B_2 + \frac{1}{2k^2}\left(\frac{\partial^2 B_2}{\partial x^2} - \frac{\partial^2 B_2}{\partial y^2}\right) - \frac{1}{k^2}\frac{\partial^2 B_1}{\partial x \partial y}\right] . \tag{6.12}$$

$$E_2(\mathbf{r}) = c\left[-B_1 + \frac{1}{2k^2}\left(\frac{\partial^2 B_1}{\partial x^2} - \frac{\partial^2 B_1}{\partial y^2}\right) - \frac{1}{k^2}\frac{\partial^2 B_2}{\partial x \partial y}\right] . \tag{6.13}$$

$$E_3(\mathbf{r}) = \frac{ic}{k}\left(\frac{\partial B_2}{\partial x} - \frac{\partial B_1}{\partial y}\right) . \tag{6.14}$$

In writing Eqs. (6.7) and (6.8), we have kept terms up to $1/(kw)^2$, where $w$ is some characteristic length scale associated with the transverse beam profile. An inspection of these equations shows that the electric and magnetic field components can be expressed in terms of two solutions of the paraxial wave equation (2.26). Let us denote these solutions of the paraxial scalar wave equation by $f(\mathbf{r})$ and $g(\mathbf{r})$, then

$$E_1(\mathbf{r}) = f(\mathbf{r}) + \frac{1}{4k^2}\left(\frac{\partial^2 f(\mathbf{r})}{\partial x^2} - \frac{\partial^2 f(\mathbf{r})}{\partial y^2}\right) + \frac{1}{2k^2}\frac{\partial^2 g(\mathbf{r})}{\partial x \partial y} . \tag{6.15}$$

$$E_2(\mathbf{r}) = g(\mathbf{r}) - \frac{1}{4k^2}\left(\frac{\partial^2 g(\mathbf{r})}{\partial x^2} - \frac{\partial^2 g(\mathbf{r})}{\partial y^2}\right) + \frac{1}{2k^2}\frac{\partial^2 f(\mathbf{r})}{\partial x \partial y} . \tag{6.16}$$

$$E_3(\mathbf{r}) = \frac{i}{k}\left(\frac{\partial f(\mathbf{r})}{\partial x} + \frac{\partial g(\mathbf{r})}{\partial y}\right) . \tag{6.17}$$

$$cB_1(\mathbf{r}) = -g(\mathbf{r}) + \frac{1}{4k^2}\left(\frac{\partial^2 g(\mathbf{r})}{\partial y^2} - \frac{\partial^2 g(\mathbf{r})}{\partial x^2}\right) + \frac{1}{2k^2}\frac{\partial^2 f(\mathbf{r})}{\partial x \partial y} . \tag{6.18}$$

$$cB_2(\mathbf{r}) = f(\mathbf{r}) + \frac{1}{4k^2}\left(\frac{\partial^2 f(\mathbf{r})}{\partial y^2} - \frac{\partial^2 f(\mathbf{r})}{\partial x^2}\right) - \frac{1}{2k^2}\frac{\partial^2 g(\mathbf{r})}{\partial x \partial y} . \tag{6.19}$$

$$cB_3(\mathbf{r}) = -\frac{i}{k}\left(\frac{\partial g(\mathbf{r})}{\partial x} - \frac{\partial f(\mathbf{r})}{\partial y}\right) . \tag{6.20}$$

One can easily check that Eqs. (6.15)-(6.20) satisfy the paraxial Maxwell's equations (6.3)-(6.6) up to terms of order $1/(kw)^2$. We now consider some explicit examples of these solutions.

## 6.2 Linearly Polarized Electromagnetic Waves

From Eqs. (6.15)-(6.20) we see that finite cross section electromagnetic waves, in general, have a longitudinal field component. In this sense it is not possible to have pure transverse electromagnetic beams. However, since the longitudinal component is smaller by a factor of $1/kw$ compared to the transverse fields, it is possible to have beams that have dominant transverse polarization. We now examine the form of a linearly polarized electromagnetic beam.

Without loss of generality, we take the direction of dominant polarization to be the $x$-direction. Then, choosing

$$f(\mathbf{r}) = \psi_{mn}(\mathbf{r}) \qquad \text{and} \qquad g(\mathbf{r}) = 0 . \tag{6.21}$$

we find Eqs. (6.15)-(6.17) take the form

$$E_1^{(mn)}(\mathbf{r}) = A_{mn}\psi_{mn}(\mathbf{r}) . \tag{6.22}$$

$$E_2^{(mn)}(\mathbf{r}) = \frac{1}{2k^2}\frac{\partial^2 \psi_{mn}(\mathbf{r})}{\partial x \partial y} . \tag{6.23}$$

$$E_3^{(mn)}(\mathbf{r}) = \frac{i}{k}\frac{\partial \psi_{mn}(\mathbf{r})}{\partial x} . \tag{6.24}$$

where $\psi_{mn}(\mathbf{r})$ is given by Eq. (2.58).

In writing Eq. (6.22) we have dropped terms involving second order derivatives of $\psi_{mn}(\mathbf{r})$ since compared to the first order terms they are smaller by the factor $1/(kw)^2$. The leading term in the cross-polarization term $E_2^{(mn)}(\mathbf{r})$ is smaller by the factor $1/(kw)^2$ compared to the $E_1$-component. It is kept here because if the beam

given by Eqs. (6.22) (6.24) is passed through a crossed polarizer, then $E_2^{(mn)}(\mathbf{r})$ is the only term that is transmitted. The longitudinal term is smaller by the factor $1/kw$ compared to the dominant transverse component.

The magnetic field components corresponding to Eqs. (6.22)-(6.24) are obtained by the relations

$$cB_1^{mn}(\mathbf{r}) = E_2^{mn}(\mathbf{r}) , \tag{6.25}$$

$$cB_2^{mn}(\mathbf{r}) = E_1^{mn}(\mathbf{r}) , \tag{6.26}$$

$$cB_3^{mn}(\mathbf{r}) = \frac{i}{k}\frac{\partial E_1^{mn}(\mathbf{r})}{\partial y} . \tag{6.27}$$

Using the properties of Hermite polynomials we can write down explicit expressions for $E_2^{(mn)}(\mathbf{r})$ and $E_3^{(mn)}(\mathbf{r})$ as

$$E_1^{(mn)}(\mathbf{r}) = A_{mn}\psi_{mn}(\mathbf{r}) . \tag{6.28}$$

$$E_2^{(mn)}(\mathbf{r}) = \frac{A_{mn}}{4(kw)^2}(4mn\psi_{m-1,n-1} - 2m\psi_{m-1,n+1} - 2n\psi_{m+1,n-1} + \psi_{m+1,n+1}) . \tag{6.29}$$

$$E_3^{(mn)}(\mathbf{r}) = A_{mn}\frac{i}{\sqrt{2}kw}(2m\psi_{m-1,n} - \psi_{m+1,n}) . \tag{6.30}$$

These equations explicitly indicate the relative magnitudes of various field components. A more quantitative measure of the relative strengths of various field components is obtained by comparing the powers associated with different field components. Let the total power associated with the beam be $P_o$. Then the power associated with different electric field components is found to be

$$P_1 = \frac{1}{4}\epsilon_o c\, \Re e \int\int_{-\infty}^{\infty} E_1 E_1^* dx dy = \frac{P_o}{2} . \tag{6.31}$$

$$P_2 = \frac{P_o}{2}\frac{(2m+1)(2n+1)}{4(kw_o)^4} . \tag{6.32}$$

$$P_3 = \frac{P_o}{2}\frac{(2m+1)}{(kw_o)^2} . \tag{6.33}$$

It follows from these equations that the power associated with different field components is a constant of propagation, that is, it is independent of $z$. Equations (6.31) (6.33) together with Eqs. (6.28)-(6.30) show that an electromagnetic beam predominantly polarized in the $x$-direction has a small cross-polarization component in the

$y$-direction in addition to a small longitudinal component. The longitudinal field component is smaller by a factor of $1/kw$ and the cross-polarization field component is smaller by a factor of $1/(kw)^2$ compared to the dominant polarization component. From these considerations it is clear that a pure transverse linearly polarized electromagnetic beam is the geometrical optics limit ($kw \to \infty$) of Eqs. (6.28) and (6.29). In general, for finite cross-section beams, both the cross-polarization and longitudinal field components must be kept for consistency with Maxwell's equations.

The presence of longitudinal field components is also required for a correct description of energy flow in the beam. Energy flow in a beam is described in terms of rays, which are curves along which energy is transported. The tangent to these curves at a given point indicates the direction of energy flow of the Poynting vector. For an electromagnetic beam, rays should converge as they approach a focal region (beam waist) and diverge as they leave the focal region. The Poynting vector averaged over an optical cycle is

$$\mathbf{S} = \frac{1}{2}\epsilon_o c^2 \Re e\,(\mathbf{E} \times \mathbf{B}) \ . \tag{6.34}$$

Using the fields given by Eqs. (6.28)-(6.30) and certain recursion relations for Hermite polynomials, we find that the Poynting vector for the beam can be written as

$$\mathbf{S} = \frac{1}{2}\epsilon_o c^2 |A_{mn}|^2 |\psi_{mn}(\mathbf{r})|^2 \left[\frac{x}{R}\hat{\epsilon}_1 + \frac{y}{R}\hat{\epsilon}_2 + \hat{\epsilon}_3\right] \ . \tag{6.35}$$

The quantity before the square brackets is simply the beam intensity (watts/m$^2$). The vector inside the square brackets denotes the direction of energy flow. If we recall that the radius of curvature is negative for a converging wave and positive for a diverging wave, it follows from Eq. (6.35) that for a beam approaching the beam waist (focal region), energy flow occurs toward the $z$ axis and away from the $z$ axis as it leaves the focal region. If the longitudinal component of the fields is ignored, then the energy flow occurs only along the $z$-axis and such a beam is not only inconsistent with Maxwell's equations, but also does not provide a correct description of focusing properties of laser beams. From Eq. (6.35) we find the equation for the family of rays is

$$\rho = \rho_o \sqrt{(z/z_o)^2 + 1} \tag{6.36}$$

where $\rho = \sqrt{x^2 + y^2}$ and $\rho_o$ is the distance of the ray from the beam axis at the beam waist $z = 0$.

The cross-polarization component is even smaller than the longitudinal component. If polarization properties of the wave are not of interest, it may be ignored. For a correct description of polarization properties however, the cross-polarization component must be kept. For example, if the beam passes through a linear polarizer whose axis is crossed with respect to the dominant direction of polarization, the cross-polarization component is the dominant component in the transmitted beam.

It is also interesting to compare the distribution of fields in a plane transverse to the direction of propagation. In general, the transverse distribution of fields evolves during propagation. It is interesting to note that this evolution does not involve a change in the energy associated with the field. This follows from Eqs. (6.31)-(6.33) where we showed that the power associated with each field component remains constant during propagation. Expressions for the transverse distribution of fields are complicated in general. In the far zone however, the fields take the form

$$E_1^{(mn)}(\mathbf{r}) = A_{mn}(-1)^{m+n+1}\sqrt{\frac{2}{\pi w^2}}H_m\left(\frac{\sqrt{2}x}{w}\right)H_n\left(\frac{\sqrt{2}y}{w}\right)e^{ik\rho^2/2\eta}\,. \quad (6.37)$$

$$E_2^{(mn)}(\mathbf{r}) = \frac{1}{(kw_o)^2}\frac{2xy}{w^2}E_1^{(mn)}(\mathbf{r})\,. \quad (6.38)$$

$$E_3^{(mn)}(\mathbf{r}) = \frac{2i}{(kw_o)}\frac{x}{w}E_1^{(mn)}(\mathbf{r})\,. \quad (6.39)$$

These field components lead to the following distributions for the intensities

$$I_1(\mathbf{r}) = \frac{2P_o}{2^{m+n}}\frac{1}{\pi w^2 n!m!}H_m^2\left(\frac{\sqrt{2}x}{w}\right)H_n^2\left(\frac{\sqrt{2}y}{w}\right)e^{-2(\rho^2)/w^2}\,. \quad (6.40)$$

$$I_2(\mathbf{r}) = \frac{4}{(kw_o)^4}\frac{x^2y^2}{w^4}I_1(\mathbf{r})\,. \quad (6.41)$$

$$I_3(\mathbf{r}) = \frac{4}{(kw_o)^2}\frac{x^2}{w^2}I_1(\mathbf{r})\,. \quad (6.42)$$

Figures 6.1, 6.2, and 6.3 show these intensity distributions for $TEM_{00}$ mode Gaussian beams. For each of these figures, the $z$-axis scale is arbitrary and not related between figures. In the next section we look at the form of a circularly polarized wave.

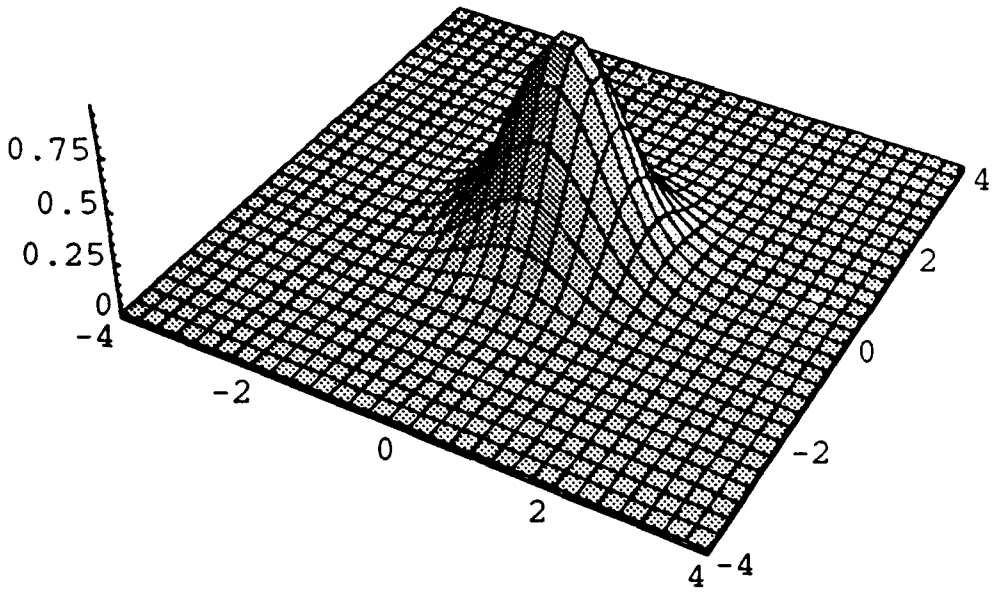


Figure 6.1: A 3-dimensional profile of the intensity distribution of a linearly polarized $TEM_{00}$ mode Gaussian beam as defined by Eq. (6.40). The $z$-axis scale is arbitrary and not related between Figs. 6.1–6.3.

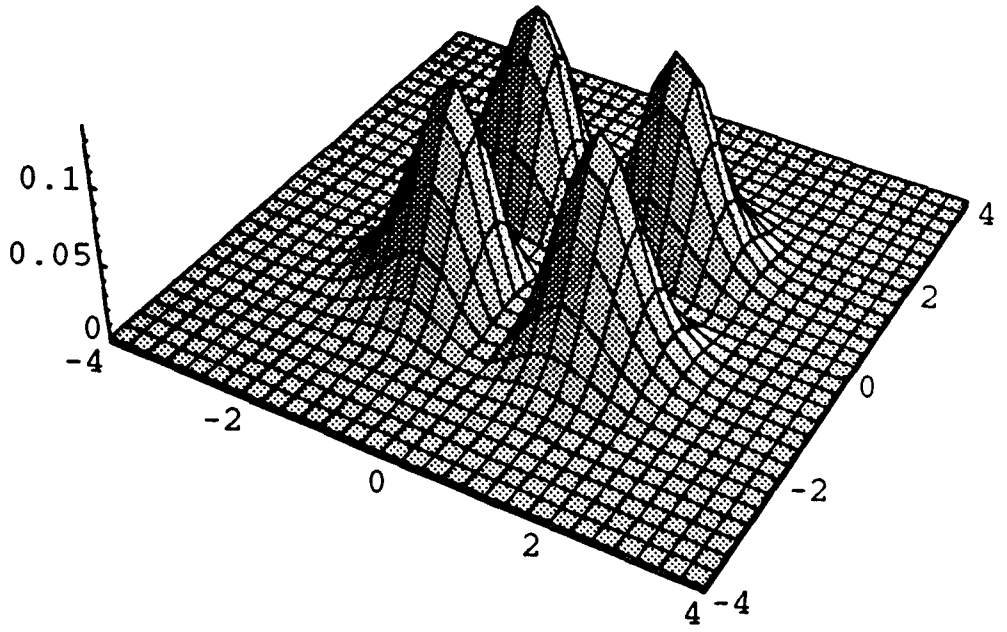


Figure 6.2: A 3-dimensional profile of the intensity distribution of a cross polarized $TEM_{00}$ mode Gaussian beam as defined by Eq. (6.41). The $z$-axis scale is arbitrary.

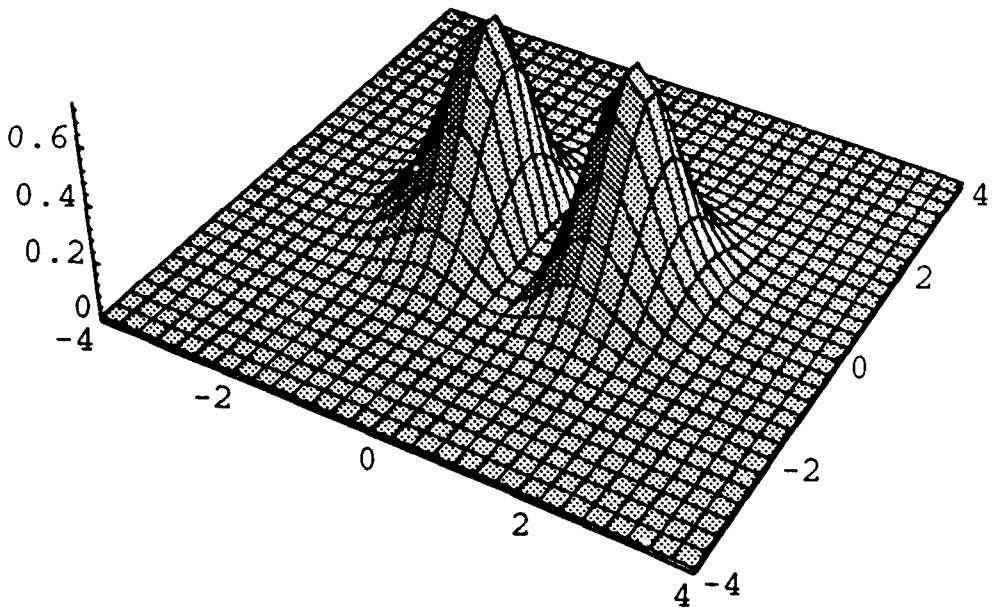


Figure 6.3: A 3-dimensional profile of the intensity distribution of the longitudinal component of a $TEM_{00}$ mode Gaussian beam as defined by Eq. (6.42). The z-axis scale is arbitrary.

## 6.3 Circularly Polarized Electromagnetic Waves

For a circularly polarized wave, we take

$$f(\mathbf{r}) = \psi_{mn}(\mathbf{r}) \qquad \text{and} \qquad g(\mathbf{r}) = i\psi_{mn}(\mathbf{r}) \,. \tag{6.43}$$

Then various field components are

$$E_1^{(mn)}(\mathbf{r}) = \frac{A_{mn}}{\sqrt{2}}\psi_{mn}(\mathbf{r}) \,, \tag{6.44}$$

$$E_2^{(mn)}(\mathbf{r}) = i\frac{A_{mn}}{\sqrt{2}}\psi_{mn}(\mathbf{r}) \,, \tag{6.45}$$

$$E_3^{(mn)}(\mathbf{r}) = \frac{iA_{mn}}{2kw_o}(2m\psi_{m-1,n} - \psi_{m+1,n} + 2in\psi_{m,n-1} - 1\psi_{m,n+1}) \,. \tag{6.46}$$

In the far zone, these equations lead to the following transverse intensity distributions

$$I_\perp(\mathbf{r}) \equiv 2I_1(\mathbf{r}) = 2I_2(\mathbf{r}) = \frac{2P_o}{2^{n+m}m!n!}H_m^2\left(\frac{\sqrt{2}x}{w}\right)H_n^2\left(\frac{\sqrt{2}y}{w}\right) \,. \tag{6.47}$$

$$I_3 = \frac{2(x^2+y^2)}{(kw_o)^2w^2}I_\perp(\mathbf{r}) \,. \tag{6.48}$$

## 6.4 Experimental Observations

Experimental observations of the intensity distributions for a linearly polarized laser beam were made using an argon ion laser operating at 488 nm with a $TEM_{00}$ mode.

Our objective was to compare the linearly polarized intensity profile of the laser beam given by Eq. (6.10) with its cross polarized intensity profile given in Eq. (6.11).

The intensity profile of the laser beam was photographed using a Cohu Inc. 4810 series monochrome solid-state CCD camera. The picture was recorded using an IBM PC and Beamcode 6.1 software. A picture of the linearly polarized beam was taken with the laser operating at less than 10 milliwatts (minimum scale on the digital power meter) and the beam attenuated through a neutral density filter with optical density (OD) 2. Pictures of the beam intensity profile are reproduced in Figs. 6.4 and 6.5. Figure 6.4 shows a 3-dimensional contour of the beam intensity and Fig. 6.5 shows a 2-dimensional planview of the beam intensity. To observe the cross polarized intensity profile, the laser was operated at approximately 110 milliwatts and the beam was transmitted through two dichroic sheet polarizers. The polarizers were oriented so that their polarization axes were orthogonal to each other. Pictures of the cross polarized beam intensity profile are reproduced in Figs. 6.6 and 6.7. Figure 6.6 shows the 3-dimensional pattern and Fig. 6.7 shows the 2-dimensional planview. The linear and cross polarized intensity distributions of Eqs. (6.10) and (6.11) can be clearly seen from these pictures. Due to the fact that the dichroic materials polarize using absorption, the relative intensity magnitudes of the beams photographed in Figs. 6.4-6.7 are undetermined.

In this chapter we have discussed the polarization properties of Gaussian beams by developing paraxial solutions to Maxwell's equations. We saw that the field components of these solutions were not independent, but coupled by Eqs. (6.3)-(6.6). This results in the presence of cross polarized and longitudinal fields in the transverse direction. The presence of the cross polarized field was observed experimentally.

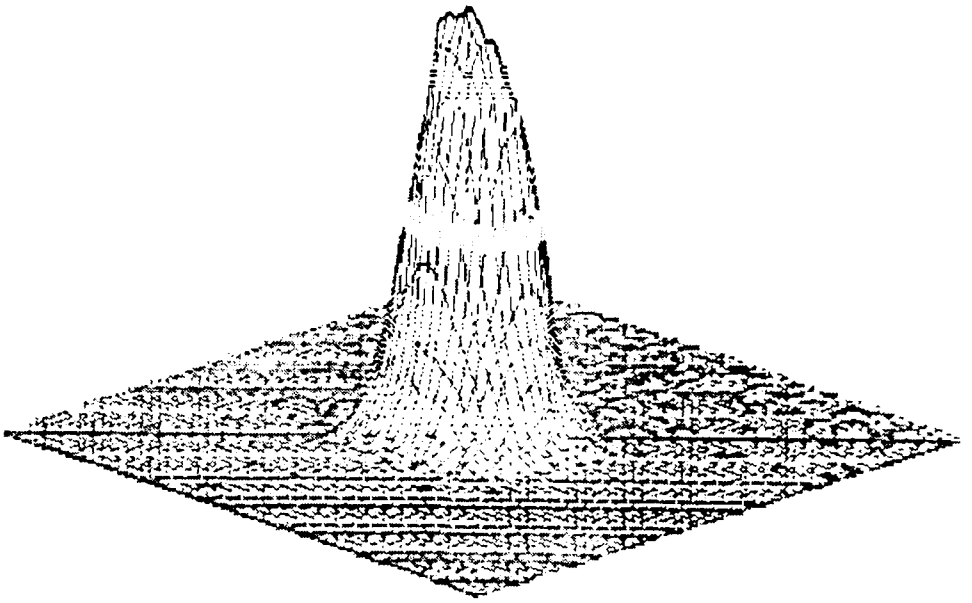

Figure 6.4: A 3-dimensional intensity profile of a linearly polarized $TEM_{00}$ laser beam. The picture was taken from an argon ion laser operating at 488 nm.

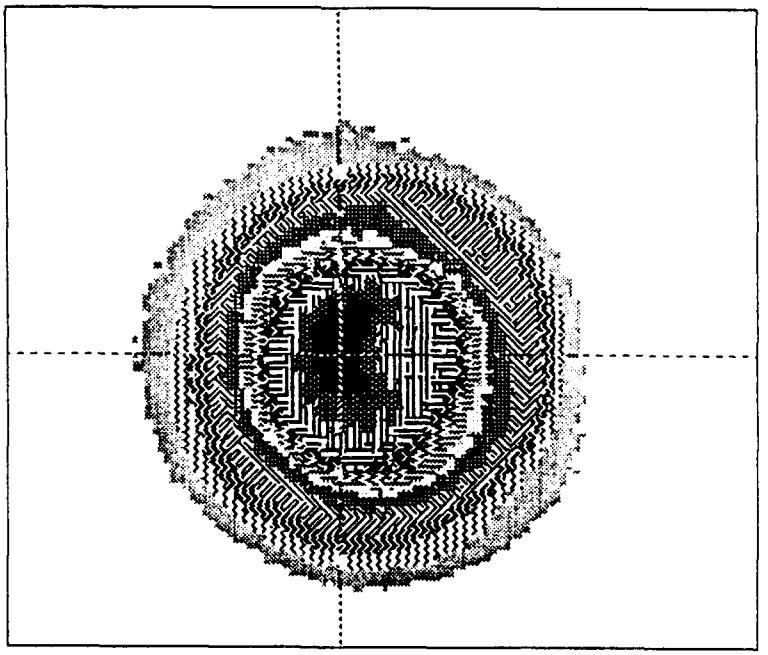

Figure 6.5: A 2-dimensional planview of the intensity profile of a linearly polarized $TEM_{00}$ laser beam. The picture was taken from an argon ion laser operating at 488 nm.

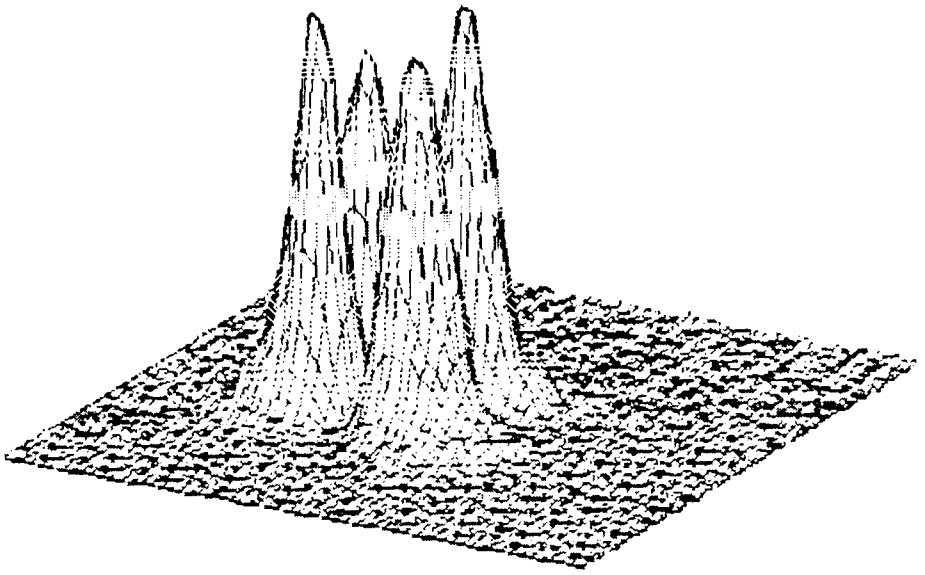

Figure 6.6: A 3-dimensional intensity profile of a cross polarized $TEM_{00}$ laser beam. The picture was taken from an argon ion laser operating at 488 nm.

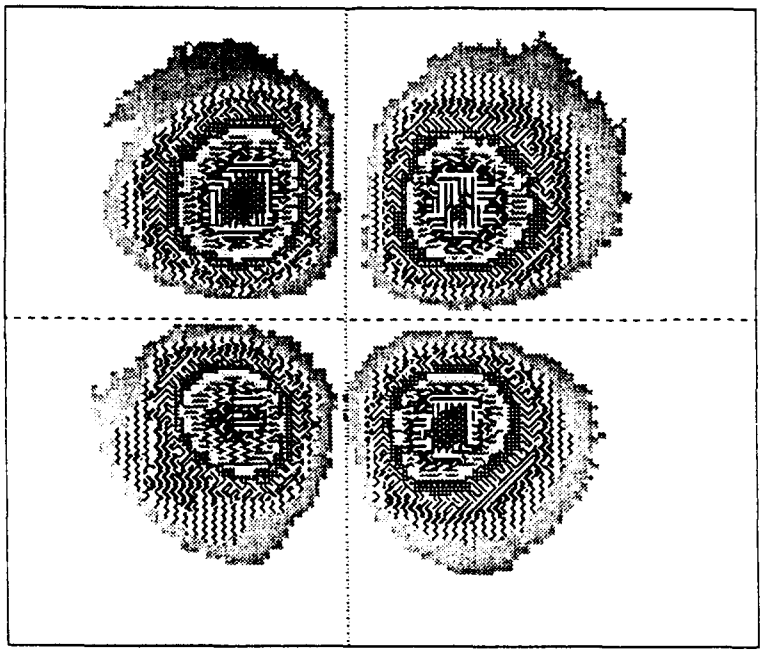

Figure 6.7: A 2-dimensional planview of the intensity profile of a cross polarized $TEM_{00}$ laser beam. The picture was taken from an argon ion laser operating at 488 nm.

# Chapter 7

# Conclusions

In this thesis we have reviewed the characteristics of laser propagation and used those characteristics to develop a method for designing a laser system. The unique characteristics of the Ti:sapphire laser make it an excellent choice for a variety of research applications. The techniques described in this thesis can be used to design a Ti:sapphire or other type of laser system for specific research applications. These techniques address the requirements of stability, astigmatism compensation, and mode matching of the pump and cavity modes.

We also studied some features of the dynamical behavior of Ti:sapphire lasers. To our knowledge, this is the first study of the relaxation oscillations of a Ti:sapphire laser. Using rate equation theory, we developed a method for measuring the upper state lifetime $\tau_2$ and intrinsic cavity loss analyzing these oscillations in the Ti:sapphire laser. Our measured values for these parameters are consistent and in agreement with the values of the upper state lifetime and the intrinsic cavity loss of our laser obtained by independent methods. Our method for determining these parameters from the study of relaxation oscillations presents a new and simple technique which can be applied to other laser systems as well.

By also using rate equation theory, we developed a method for modeling the dynamical behavior of lasers. This method scales the laser rate equations in such a way as to allow numerical solutions from experimentally measured parameters.

We described an experiment for measuring the intrinsic cavity loss by inducing variable cavity loss and measuring the pump power required to reach laser threshold. This experimental procedure allows us to also estimate the normalized pumping rate $R$, the small signal gain coefficient $g$, and the stimulated emission cross section $\sigma_{21}$ of any laser system.

Finally we discussed the interesting field of beam-like vector solutions to Maxwell's equations. These solutions characterize the polarization properties of Gaussian beams. We also saw experimental evidence of the cross polarization intensity profile predicted by our solutions.

The field of laser dynamics is very rich and the Ti:sapphire laser provides an excellent system for studying many aspects of dynamical behavior. By varying the depth and frequency of cavity gain or loss modulation, an investigation into chaotic dynamics, deep spiking oscillations, and generation of specific waveforms can be conducted. Studies of directional mode competition and bistability can also be carried out on a laser system similar to the one described in this thesis. Other interesting opportunities for research include first passage time studies in the scaling regime [49, 50], antiphase studies, and other multi-mode phenomena.

## Bibliography


[1] P. F. Moulton. Spectroscopic and laser characteristics of Ti:$Al_2O_3$. *J. Opt. Soc. Am. B*, 3(1):125–132, 1986.

[2] T. L. Boyd and H. J. Kimble. Frequency stabilization of a continuous-wave Ti:sapphire laser. *Opt. Lett.*, 16(11):808–810, 1991.

[3] C. S. Adams and A. I. Ferguson. Saturated spectroscopy of and two-photon absorption spectroscopy in rubidium using an actively stabilized Ti:$Al_2O_3$ ring laser. *Opt. Commun.*, 75(5,6):419–424, 1990.

[4] W. Vassen, C. Zimmermann, R. Kallenbach, and T. W. Hänsch. A frequency-stabilized titanium sapphire laser for high resolution spectroscopy. *Opt. Commun.*, 75(5,6):435–439, 1990.

[5] K. Nananuma and K. Mogi. 50-fs pulse generation directly from a colliding-pulse mode-locked Ti:sapphire laser using an antiresonant ring mirror. *Opt. Lett.*, 16(10):738–740, 1991.

[6] U. Keller, G. W. 't Hooft, W. H. Knox, and J. E. Cunningham. Femtosecond pulses from a continuously self-starting passively mode-locked Ti:sapphire laser. *Opt. Lett.*, 16(13):1022–1024, 1991.

[7] J. Goodberlet, J. Wang, J. G. Fujimoto, and P. A. Schulz. Starting dynamics of additive-pulse mode locking in the Ti:$Al_2O_3$ laser. *Opt. Lett.*, 15(22):1300–1302, 1990.

[8] J. C. Barnes, N. P. Barnes, and G. E. Miller. Master oscillator power amplifier performance of Ti:$Al_2O_3$. *IEEE J. Quantum Electron.*, 24(6):1029–1037, 1988.

[9] J. D. Kmetec, J.J. Macklin, and J. F. Young. 0.5-TW, 125-fs Ti:sapphiire laser. *Opt. Lett.*, 16(13):1001–1003, 1991.

[10] P. A. Schulz and S. R. Henion. Liquid-nitrogen-cooled Ti:$Al_2O_3$ laser. *IEEE J. Quantum Electron.*, 27(4):1039–1047, 1991.

[11] R. J. Collins, D. F. Nelson, A. L. Schawlow, et al. Coherence, narrowing, directionality, and relaxation oscillations in the light emission from ruby. *Phys. Rev. Lett.*, 5(7):303–305, 1960.

[12] Y. Miyazoe and M. Maeda. On the spiking phenomenon in organic dye lasers. *IEEE J. Quantum Electron.*, 7(36):36–37, 1971.

[13] H. Taniguchi and H. Saito. On the relaxation oscillations in copper-vapor lasers. *J. Appl. Phys.*, 65(10):4068–4070, 1989.

[14] J. Lin, J. K. Gamelin, K. Y. Lau, and S. Wang. Ultrafast (up to 39 GHz) relaxation oscillations of vertical cavity surface emitting laser. *Appl. Phys. Lett.*, 60(1):15–17, 1992.

[15] H. Kogelnik and T. Li. Laser beams and resonators. *Appl. Opt.*, 5(10):1550–1567, 1966.

[16] Anthony E. Siegman. *An Introduction to Lasers and Masers*. McGraw-Hill Book Company, New York, 1971.

[17] Anthony E. Siegman. *Lasers*. University Science Books, Mill Valley, Ca, 1986.

[18] Amnon Yariv. *Quantum Electronics*. John Wiley and Sons, New York, 1989.

[19] H. W. Kogelnik, E. P. Ippen, A. Dienes, and C. V. Shank. Astigmatically compensated cavities for CW dye lasers. *IEEE J. Quantum Electron.*, 8(3):373–379, 1972.

[20] C. Pfistner, P. Albers, and H. P. Weber. Influence of spatial mode matching in end-pumped solid state lasers. *Appl. Phys., B*, 54(1):83–88, 1992.

[21] Arthur C. Hardy and Fred H. Perrin. *The Principles of Optics*. McGraw Hill Book Company, Inc., New York, 1932.

[22] P. A. Schulz. Single-frequency Ti:$Al_2O_3$ ring laser. *IEEE J. Quantum Electron.*, 24(6):1039–1040, 1988.

[23] B. E. A. Saleh and M. C. Teich. *Fundamentals of Photonics*. John Wiley and Sons, Inc., New York, 1991.

[24] I. J. Hodgkinson and J. I. Vukusic. Birefringent tuning filters without secondary peaks. *Opt. Commun.*, 24(1):133–134, 1978.

[25] I. J. Hodgkinson and J. I. Vukusic. Birefringent filters for tuning flash-pumped dye lasers: Simplified theory and design. *Appl. Opt.*, 17(12):1944–1948, 1978.

[26] D. R. Preuss and J. L. Gole. Three-stage birefringent filter tuning smoothly over the visible region: theoretical treatment and experimental design. *Appl. Opt.*, 19(5):702–710, 1980.

[27] S. Zhu. Birefringent filter with tilted optic axis for tuning dye lasers: theory and design. *Appl. Opt.*, 29(3):410–415, 1990.

[28] Yung S. Liu. Line narrowing and tuning of a high-power Nd:glass laser using an intracavity Brewster-angle birefringent filter. *J. Appl. Phys.*, 48(2):647–649, 1977.

[29] F. Ortwein, J. Mentel, and E Schmidt. A birefringent filter as a tuning element for multiline He – $Se^+$ laser. *J. Phys. D: Appl. Phys.*, 22:488–491, 1989.

[30] A. L. Bloom. Modes of a laser resonator containing tilted birefringent plates. *J. Opt. Soc. Am.*, 64(4):447–452, 1974.

[31] P. D. Hale and G. W. Day. Stability of birefringent retarders (waveplates). *Appl. Opt.*, 27(24):5146–5153, 1988.

[32] Peter W. Milonni and Joseph H. Eberly. *Lasers*. John Wiley and Sons, New York, 1988.

[33] Walter Koechner. *Solid State Laser Engineering.* Springer-Verlag, Berlin, 1988.

[34] Herbert Goldstein. *Classical Mechanics.* Addison-Wesley Publishing Company, Reading, MA, second edition, 1981. Chap. 6.

[35] A. C. Reardon. Exact solutions of laser rate equations. *J. Mod. Opt.*, 38(5):857-864, 1991.

[36] Philip R. Bevington. *Data Reduction and Error Analysis for the Physical Sciences.* McGraw-Hill Book Company, New York, 1969.

[37] P. Lacovara, L. Esterowitz, and M. Kokta. Growth, spectroscopy, and lasing of titanium-doped sapphire. *IEEE J. Quantum Electron.*, 21(10):1614-1623, 1985.

[38] R. L. Aggarawal, A. Sanchez, R. E. Fahey, and A. J. Strauss. Magnetic and optical measurements on Ti:$Al_2O_3$ crystals for laser applications: Concentration and absorption cross section of $Ti^{3+}$ ions. *Appl. Phys. Lett.*, 48(20):1345-1347, 1986.

[39] C. E. Byvik and A. M. Buoncristiani. Analysis of vibronic transitions in titanium doped sapphire using the temperature of the fluorescence spectra. *IEEE J. Quantum Electron.*, 21(10):1619-1623, 1985.

[40] P. Albers, E. Stark, and G. Huber. Continuous-wave laser operation and quantum efficiency of titanium-doped sapphire. *J. Opt. Soc. Am. B.* 3(1):134-139, 1986.

[41] A. Sanchez, R. E. Fahey, A. J. Strauss, and R. L. Aggrawal. Room-temperature continuous-wave operation of a Ti:$Al_2O_3$ laser. *Opt. Lett.*, 11(6):363-364, 1986.

[42] G. F. Albrecht, J. M. Eggleston, and J. J. Ewing. Measurements of $Ti^{3+}$:$Al_2O_3$ as a lasing material. *Opt. Commun.*, 52(6):401-404, 1985.

[43] K. F. Wall, R. L. Aggarwal, R. E. Fahey, and A. J. Strauss. Small-signal gain measurements in a Ti:$Al_2O_3$ amplifier. *IEEE J. Quantum Electron.*, 24(6):1016-1019, 1988.

[44] R. Simon, E. C. G. Sudarshan, and N. Mukunda. Gaussian-Maxwell beams. *J. Opt. Soc. Am. A*, 3(4):536–539, 1986.

[45] Y. Fainman and J. Shamir. Polarization of nonplanar wave fronts. *Appl. Opt.*, 23(18):3188–3195, 1984.

[46] L. W. Davis. Theory of electromagnetic beams. *Phys. Rev. A*, 19(3):1177–1179, 1979.

[47] D. N. Pattanayak and G. P. Agrawal. Representation of vector electromagnetic beams. *Phys. Rev. A*, 22(3):1159–1164, 1980.

[48] M. Lax. From Maxwell to paraxial wave optics. *Phys. Rev. A*, 11(4):1365–1370, 1975.

[49] M. R. Young and S. P. Singh. Observation of the "Brownian motion" of the electric field in a laser. *Phys. Rev. A*, 35(3):1453–1456, 1987.

[50] M. R. Young and S. P. Singh. Measurements of first-passage-time distributions in laser transients near threshold. *J. Opt. Soc. Am. B*, 5(5):1011–1019, 1988.